Modelling of the diffuse arc in a vacuum circuit-breaker

MODELLING OF THE DIFFUSE ARC IN A VACUUM CIRCUIT-BREAKER

HANS SCHELLEKENS

This work forms a part of a research program on vacuum circuit breakers conducted at Holec Switchgear Group, Hengelo, the Netherlands.

MODELLING OF THE DIFFUSE ARC IN A VACUUM CIRCUIT-BREAKER

PROEFSCHRIFT

ter verkrijging van de graad van doctor in de technische wetenschappen aan de Technische Hogeschool Eindhoven, op gezag van de rector magnificus, prof.dr. S.T.M. Ackermans, voor een commissie aangewezen door het college van dekanen in het openbaar te verdedigen op dinsdag 8 maart 1983 te 16.00 uur

door

Hans Schellekens

geboren te Alkmaar

DIT PROEFSCHRIFT IS GOEDGEKEURD
DOOR DE PROMOTOREN

Prof.dr.ir.D.C.Schram
en
Prof.dr.ir.P.C.T.van der Laan

Contents

1. INTRODUCTION

1.1. General

Circuit-breakers protect transmission and distribution systems from the electrical energy released during overloads and short circuits. When this occurs, the circuit-breaker isolates the defective part of the electrical system from the remaining distribution system. Usually, these circuit-breakers are electro-mechanical switching devices containing a pair of electrical contacts, one of which is movable.

If, for some reason, the current has to be interrupted, the contacts are separated. After contact separation the current does not drop instantly to zero, but will remain flowing through the medium between the two contacts of the circuit-breaker. Depending on the type of circuit-breaker the medium consists of vacuum, gas, oil or semiconductor.

Some circuit-breakers build up an arc voltage equal to the current driving voltage and thus force the current to zero. Other breakers, particularly in a.c. circuits, wait until the occurrence of a natural current zero. Current interruption then takes place through the rapid recovery of the insulating properties of the inter-electrode medium.

Vacuum insulation has a number of advantages over conventional gas or oil insulation for interrupter applications. The high hold-off voltage of the contact gap under high vacuum is determined only by the properties of the contact surface. Theoretically vacuum has a larger dielectric strength than any other gaseous dielectric for a fixed electrode arrangement.

Vacuum interrupters also give an extremely rapid rate of rise of recovery voltage of the order of 20 kV/µs This is many times larger than that of a gas blast interrupter of similar rating. The low arcing voltage during the interruption process produces only low energy dissipation in the vacuum interrupter, much less than in conventional methods of switching. Therefore arc erosion is very slight even at high switching frequencies and thus the vacuum interrupter has a long life. The large hold-off voltage of a vacuum circuit-breaker allows also for a short contact stroke compared to other types of circuit-breakers. This simplifies the actuating mechanism, thereby increasing the reliability of the whole system. With these advantages over other switchgear the application of vacuum interrupters in distribution systems is already widespread. The use of vacuum interrupters in transmission systems is restricted as a result of their limited capability to interrupt high currents.

The excellent properties of the vacuum switch are limited to currents below approximately 10 kA, where the arc constricts, and an anode spot is formed. The increased erosion due to the anode spot degrades the contact surface causing a lower dielectric strength. It will be clear that the deteriorating effects associated with the anode spot should be avoided. One way of achieving this is to use contact geometries that produce a magnetic field

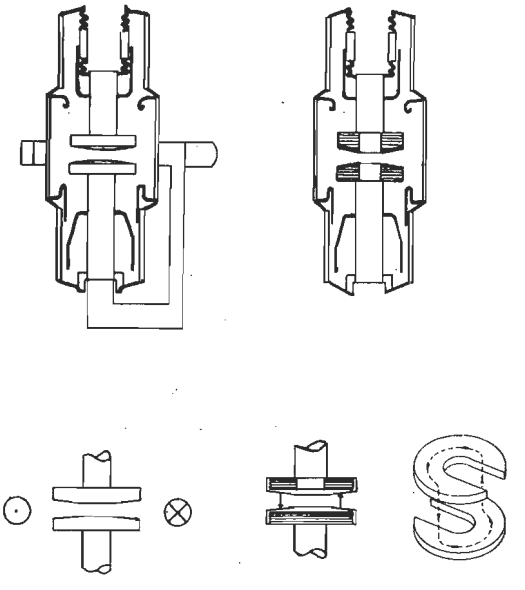

Figure 1.1 Two vacuum circuitbreakers using an axial magnetic field.

a. axial magnetic field generated by an external coil
b. axial magnetic field generated by two iron horseshoes around the main current conductor.

which moves the anode spot across the electrode so that excessive electrode wear is avoided . A different approach to this problem is to increase the current at which an anode spot forms by using an axial magnetic field.
Two commercially available vacuum circuit-breakers equipped with axial magnetic fields are shown in figure 1.1. As at present knowledge about the basics of the interaction between axial magnetic field and arc is lacking, it is this interaction which will be studied in more detail in this thesis.

1.2. Purpose of the investigation

Three arcing regimes can be distinguished dependent on the external parameters. For the electrode geometry studied below these three arcing regimes are shown in a diagram of axial magnetic field strength versus current (see figure 1.2.)

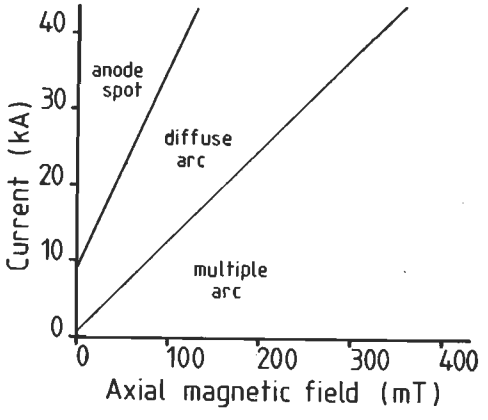

Figure 1.2 Diagram representing the three arcing regimes of the vacuum arc between 60 mm diameter copper electrodes with 10 mm clearance as a function of the external parameters: current and axial magnetic field.

1. the multiple arc. Here the arc current is concentrated in narrow channels. The background plasma, in which these arcs are embedded, is of relatively low density. The current channels contrast visible with their surroundings, which results in an optical image of multiple arcs.

2. the diffuse arc: Cathode spots feed the arc with metal vapour plasma, so that the region in between the electrodes becomes filled with a diffuse homogeneous plasma. The anode acts as a passive collector of current.

3. the arc with an anode spot: On the anode a vigorously evaporating anode spot emits additional metal vapour into the arc and current conduction is limited to the bright vapour colomn extending from the anode towards the cathode.

As can be seen from figure 1.2 the current values at which the transitions from regimes 1 to 2 and 2 to 3 occur increase with magnetic field strength.
The working hypothesis of the present work is, that the formation of the anode spot is a result of the phenomena that set in during the diffuse vacuum arc. So in this thesis the physics of the diffuse arc will be investigated both experimentally and theoretically.
In chapter 2 first an short introduction is given into some characteristics of the vacuum arc. Then the three different types of arcing behaviour will be elucidated.
The transition from the multiple arc to the diffuse arc regimes is indicated with help of an optical probe method.
In chapter 3 the experimental setup of the idealized vacuum circuit-breaker used is shown.
Also the exact parameter range used in this study will be given.
In chapter 4 four different measurement techniques are shown, which are used to measure the plasma parameters e.g.: electron temperature, ion temperature, electron density, effective charge, neutral density and axial magnetic field strength.
In chapter 5 the vacuum arc plasma is modelled in accordance with magnetohydrodynamic theory. An important condition in this model is, that the mean free path of the arc constituents, e.g. electrons, ions and neutrals is shorter than the characteristics dimensions of the arc plasma. The experiments described in chapter 4 indicate that this limiting condition is indeed ful filled in the diffuse arc. In this model statements the current density and the electric field in the arc are related to the plasma parameters.

In chapter 6 the experimental results of chapter 4 are compared with literature. Also the interrelation between the various experimental results and the arcing model is discussed with emphasis on the pressure distribution in the arc, the current flow and the arc voltage.
The results of the discussion yield an explanation of the formation of the anode spot.
Finally in chapter 7 from the presented analysis of the diffuse vacuum arc some conclusions are drawn.

2. THE DIFFUSE VACUUM ARC

In this chapter the range of interest for the various parameters will be defined and in particular attention will be given to what is called the diffuse vacuum arc.
First in section 2.1 some general features of the vacuum arc that are widely accepted, will be mentioned although most of them are not well understood.
Then follows a description of the vacuum arc in absence of an axial magnetic field This description is mainly based on a study performed by Mitchell (Mit70).
Then a description of the vacuum arc in an axial magnetic field is given.
The chapter ends with some remarks on the validity of the diffuse arc.

2.1 General description of the vacuum arc

In a vacuum circuit-breaker in closed position the current at the contact surface of two electrodes passes through a number of small areas. (Hol 67, Far 80b). The number and size of these areas depend on contact pressure, roughness and hardness of the electrode surface. When the contacts begin to separate, the number of these areas decreases and eventually all current has to pass through only one spot. At this spot the dissipated heat, due to Ohmic losses, will be sufficient to bring the metal to its boiling point. The metal evaporates and an arc will start to burn in the metal vapour. Strictly, it is better to speak of a metal vapour arc than of a vacuum arc.

At current levels below anode spot formation, the only source of material is the cathode. On the cathode hot spots exist (the cathode spots) with a typical diameter of several micrometers (Daa 74).
The temperature is estimated to be around the atmospheric boiling point of the electrode material (Eck 80). Here the current flow from metal to arc is carried by thermal field emission (Far 80a, Daa 78).
According to this mechanism, the effective potential barrier for electron emission at the cathode surface is reduced in height and thickness by a strong electric field just outside the surface.
Because the metal surface is also heated, the electrons with the highest energy approaching the surface from the inside of the metal can then pass over the potential barrier (enhanced thermionic emission) into the electrode gap, as first described by Schottky (Sch 24). Less energetic electrons can pass through the potential barrier by tunnelling (field emission) (Fow 28).

Due to the high temperature of the cathode spot, cathode material evaporates and a jet of vapour is driven from the cathode spot (Eck 80).
For a single cathode spot the mean velocity of the jet of copper vapour has been derived from the force on a vane inserted in the jet and the reaction force at the cathode (or from the mass gain of the vane); the velocity turns out to be in the 10^4 m/s range. (Ply 65, Tan 30, Eas 34).
Also the ions move away from the cathode with mean velocities of around $1\text{-}2\times10^4$ m/s in the case of singly ionized copper Dav 69). These high velocities, (the corresponding kinetic energies are higher than could be obtained from the total potential drop across the arc) make a potential maximum just above the cathode plausible.
More refined investigations of the velocity distribution of the ions show that magneto-hydrodynamic effects are important as well (Mil 81).
An alternative explanation is given by Drouet (Dro 81). He claims that the ion acceleration may be a result of a conversion of internal energy of the cathode spot plasma into kinetic energy.

Each cathode spot can only sustain a limited amount of current. On copper electrodes this limit is between 75 and 100 A per cathode spot (Dja 71).
If the total current is increased above this value a new cathode spot will be formed and both spots will move away from each other. These spots move into a

direction opposite to what should be expected from Ampère's law. Therefore this motion is called the "retrograde" motion (Sta 03).
The velocity increases proportionally to the azimuthal magnetic field generated by the current up to about 20 m/s at 40 mT for copper.
At higher magnetic flux densities the increase in velocity is relatively slow (She 75, Gun 72). As a result of the retrograde motion at high current levels the whole cathode surface will be covered with cathode spots.

Other features of the arc, like arc voltage and appearance depend on electrode geometry and external fields.
Therefore, they will be treated in the next sections.

2.2. The vacuum arc in the absence of an axial magnetic field

In the absence of an axial magnetic field the arc voltage is largely independent of contact separation and arc current up to certain limits (Mit 70). For plain copper butt contacts with a diameter of 60 mm and a clearance of 10 mm (the geometry used throughout this study), the maximum current up to which the voltage is constant, 20-21 Volts, is 800 A (Gun 78). At higher currents the voltage increases with the current and is affected by the diameter of the contacts and their distance of separation.
Above approximately 6 kA the arcing voltage becomes unstable and when the current exceeds 8 kA an anode spot will form. (Mit 70, Ric 71, Kim 69). In figure 2.1 the arc voltage of this type of arc is presented.

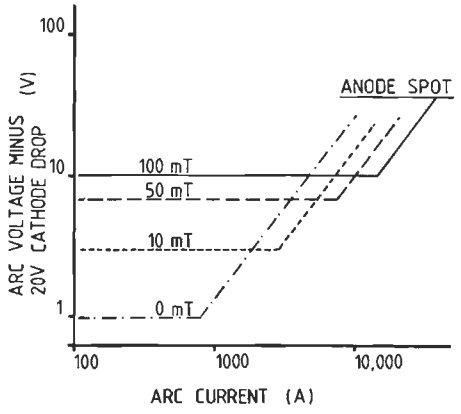

Figure 2.1 Arc voltage against arc current for a vacuum arc between 60 mm diameter copper electrodes with a 10 mm clearance at various axial magnetic field strengths.

The appearance of the vacuum arc before anode spot formation is described by Mitchell (Mit 70) as follows:"The discharge is supported by a number of cathode spots which move constantly over the cathode surface. Colour cine records show that these spots are white and that the diffuse plasma, which emanates from these high current density regions is bright green".
This type of arc with a positive current-voltage relationship is hence called the diffuse vacuum arc.
The formation of the anode spot is not only dependent on the contact geometry but depends also on the arcing time (Ric 71, Box 78). The value of 8 kA mentioned here applies to a 50 Hz sinusoidal current wave. From the anode spot vapour jets hit the cathode, until a large cathode spot is formed, in which the small cathode spots slowly disappear (Mit 70, Heb 80). What remains is a highly constricted vacuum arc in which concentrated bright vapour columns are emitted from molten spots on the anode and cathode. This type of arc resembles the high pressure welding arcs. (Kim 74)

2.3 The vacuum arc in an axial magnetic field.

2.3.1 The single arc channel

A single cathode spot on copper electrodes while moving across the electrode can carry a current between 10 and 100 amperes. Below 10A arcing behaviour is very unstable and can lead to current interruption by current chopping. Above 100 A the cathode spot splits into two new spots. Here the appearance and the voltage across a single 100 A arc will be discussed.

The appearance of this low current vacuum arc on copper electrodes has already been discussed by Morimiya and by Rondeel (Mor 73, Ron 75).
The former measures a 1-2 mm radius of a 80 A arc at a distance of 5 mm from the cathode. The latter gives microdensitometer curves obtained from the image of an arc of

150 A on high speed film.
The interpretation of Rondeel's results is difficult, because the photographic properties of the film used are not given, and because the blackness or density of all films exhibit a non linear behaviour with the intensity.

In the experimental method employed below the light intensity distribution of the 100 A arc was measured by side-on photography. From these measurements the radius of the arc was deduced.
The set-up used for these measurements is shown in figure 2.2.

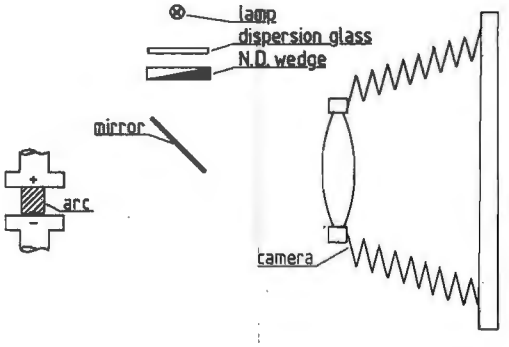

Figure 2.2 Experimental set up, with arc and calibration equipment, used to measure the diameter of a single 100 A arc. (N.D. = neutral density)

The arc was photographed with Polaroid film type 55 with a resolution of 150 lines/mm, through a f 5.6 camera with an image ratio of 1 to 1. Also on the same photographic plate an image of a calibrated, illuminated neutral density wedge was formed. For each photograph this yields a relation between the real intensity and the blackening of the negative. The current source of the arc was a charged capacitor in series with a resistance. This circuit has with a rise time of 0.01 ms and a decay time of 4 ms.
In order to reduce the movement of the arc to a minimum during the exposure the current through the arc was commutated in a thyristor 0.01 ms after the start of the discharge.
The integrated intensity of the illuminated wedge was adapted to that of the arc by a suitable choice of exposure time of the camera.

Figure 2.3. shows an example of a photograph obtained in this manner. The

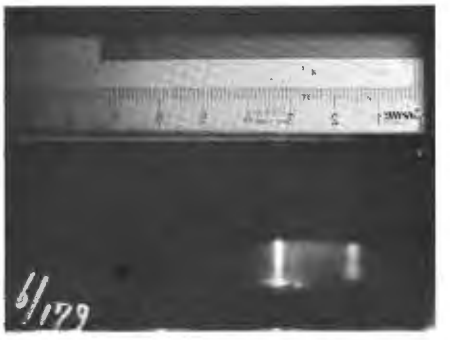

Figure 2.3 A result obtained with the experimental set up of figure 2.2.

trigger discharge in the anode can be clearly seen as well as the protrusion on the cathode (on which the optical system was focussed). A ruler was fixed to the wedge to have an accurate spatial resolution; also an extra neutral density filter was fixed to the wedge to increase its dynamic range.

Figure 2.4. shows the measured lateral intensity of the 100 A arc at 100 mT shown in figure 2.3. This intensity profile is approximated by a Gauss-function.

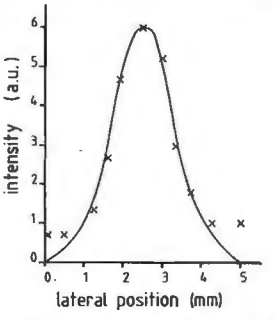

Figure 2.4 The measured lateral intensity (in arbitrary units a.u.) of the 100 A arc at 100 mT halfway the electrodes of figure 2.3.

The emission profile is now easily determined, because the shape of the Gauss function remains unchanged by an Abel inversion. The radius of the arc, defined as the length, where the emission coefficient drops by a factor of 1/e, is shown in figure 2.5. as a function of the axial magnetic field.
This study gave a systematically lower value for the radius of the arc than was found by Mor 73 and Ron 75, but the deviation remained less than twice the error bar. In figure 2.5 also the pictures taken of arc are shown.
These show that for a fixed axial position the emissivity increases with the axial magnetic field strength.
The high luminosity in front of the anode is thought to be caused by the excitation

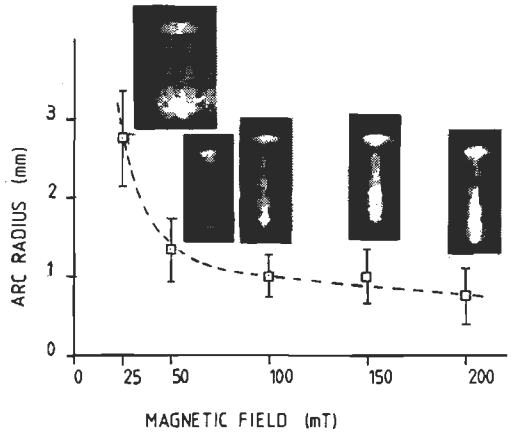

Figure 2.5 The radius of the 100 A arc as a function of the axial magnetic field. Each picture represents a measurement at the specified parameters.

of neutrals as a result of inelastic electron-neutral collisions. These neutrals may return to the arc from the recombination region near the anode surface. The photographs also show an optical illusion. It seems as if the arc channels become narrower towards the anode. This is caused by the decrease of intensity towards the anode.
Figure 2.6 shows the radius at 50 mT as a function of the distance to the cathode. Within the accuracy of the measurements no dependence on the axial position is found, but the peak local emissivity decreases towards the anode. The same behaviour is found at other arc parameters.

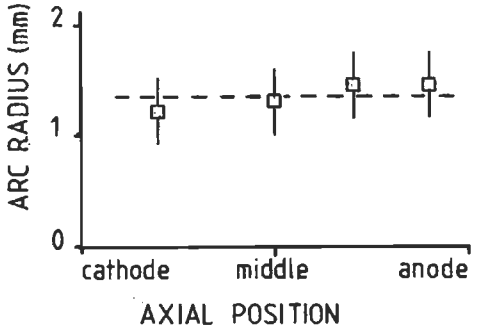

Figure 2.6 The radius of the 100 A arc at 50 mT as function of the axial position. The clearance between the electrodes is 10 mm.

The radius of a single arc channel is smaller than the axial dimensions and the arc is fed from a single spot on the cathode.
Because of these aspects a single arc channel resembles a hollow cathode arc. (Lid 62, Del 74, The 77). Although the forces, determining the pressure balance of this arc channel, are unknown (at the moment there is no relevant study on this subject available), the resemblance to the hollow cathode arc suggests that both pinch force and diffusion largerly govern the pressure balance (Pot 79, Sch 83).
The decrease of the radius with increasing magnetic field corresponds to an increase of the local emissivity, which is most probably caused by an increase of the particle density in the arc channel.
The density may be enhanced by a reduction of the radial diffusion as a result of the axial magnetic field.

The arc voltage of a single 100 A arc increases slowly from 20 Volt without axial magnetic field to about 30 Volt at 100 mT (see figure 2.15). For the greater part this voltage drop is across the cathode spot: 18-20 Volt (Ree 63), the other part is across the arc column.
Gundlach found this column voltage drop to depend logarithmically on the distance from the anode to the cathode spot. (Gun 78)

Now that some characteristics of a 100 A arc in an axial magnetic field have been explored the high current arc will be looked at more closely.

It should however be born in mind that it would be too simple and hence erroneous to expect the high current arc to be a mere superposition of independent 100 A arcs. With the current not only the number of arcs but also the density of the background plasma increases, as will become evident in chapter 6.
When the background density becomes comparable to the density in an arc channel one can no longer distinguish between separate arcs and a different description of the resulting interelectrode plasma is required.

2.3.2 The high current arc

When the current is increased beyond 100 A the cathode spot splits and several cathode spots with corresponding arc channels are formed. This results in the appearance of the arc, as displayed in figure 2.7.
At this stage the arc voltage is still the same as that of a single 100 A arc.
The background density is still low and the vacuum arc behaves like multiple independent arc channels so this type of arc is called the multiple arc (see figure 1.2).

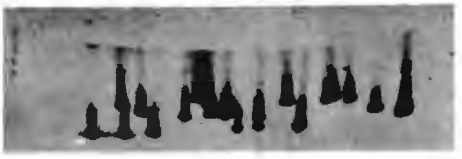

Figure 2.7 A high current vacuum arc, 3 kA, in an axial magnetic field 100 mT, between 60 mm diameter copper contacts. The arc is split up in 100 arcs. The multiple arcing mode.

The arc voltage remains constant at a fixed axial magnetic field strength up to a certain current. This is illustrated in figure 2.8 which shows the oscillogram of current and arc voltage of a multiple arc. The sudden jump in arc voltage from zero to to a finite value is caused by an electronic safety circuit, which prevents arc voltage measurements during the first millisecond.

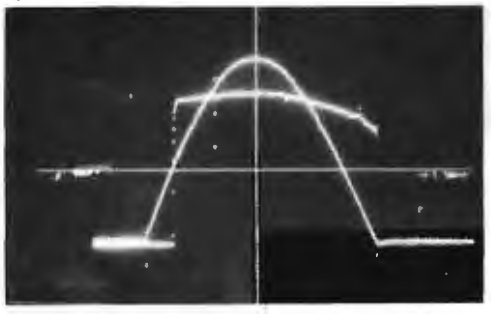

Figure 2.8 Oscillogram of the multiple arc.
B_z = 200 mT
sinusoidal current 10 kA/peak
arc voltage 35 V/peak
horizontal timebase ± 20 ms

At still higher currents the arc voltage starts to rise. This is illustrated in figure 29 an oscillogram for this type of arc.

This arc is characterized by a positive voltage current relationship, which is also represented in figure 2.1. for fixed axial magnetic field strengths.

In the absence of an axial magnetic field, this type of arc was called diffuse by Mitchell (Mit 70).

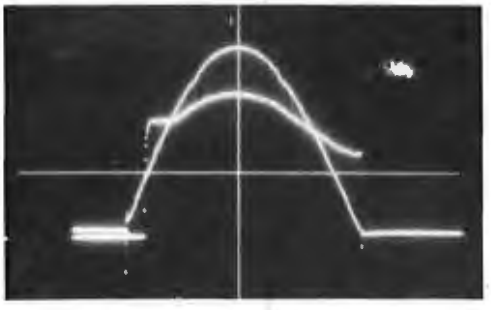

Figure 2.9 Oscillogram of the diffuse arc.
B_z = 25 mT
sinusoidal current 10 kA/peak
arc voltage 36 V/peak

In the presence of an axial magnetic field the concept of the diffuse arc, based solely on photographs, is subjective as can be seen in figure 2.10 where still some individual arc channels can be distinguished in the diffuse background plasma.
(This may be caused by the properties of the film, which exaggerates intensity differences, as already seen in the preceding paragraph.)
Based on the positive voltage-current relationship the arc could be however called diffuse.

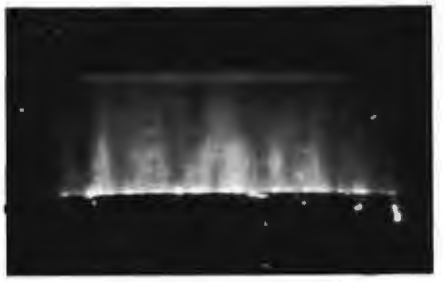

Figure 2.10 A high current diffuse vacuum arc in an axial magnetic field.

In the next paragraph an optical method using photo diodes, by which it is possible to determine the transition from the multiple arc to the diffuse arc more sensitively will be described.

At still higher currents the arc ultimately constricts in an anode spot. The current level at which this happens increases with the axial magnetic field strength.
For instance at an magnetic field strength of 50 mT an anode spot forms at 24 kA (see figure 1.2 and 2.1), or at a current level three times as high as in the absence of any magnetic field.
Once an anode spot is formed, it has devastating effects on the electrodes, regardless of the strength of the axial magnetic field.

2.4 The diffuse arc

Above it was shown (based on high speed photography) that the diffuse vacuum arc in the absence of an axial magnetic field was visually diffuse (Mit 70). So, in this case there is no doubt about the plasma state. With an axial magnetic field things are more complex. Based on the positive current-voltage characteristic the arc is diffuse above a certain current, which depends on the axial magnetic field strength.

however, at a moderate axial magnetic field strength by photographystill some arc channels can be distinguished in the diffuse background plasma light.
In a strong axial magnetic field the diffuse background plasma is too teneous to be visible.
Now the question can be raised: when does the diffuse background plasma have an influence on the arcing behaviour?
The increase of the arc voltage may be an indication of this influence. However, the arcing voltage is the result of many complex arcing processes, which may already occur before they raise the voltage by a measurable quantity.
As mentioned before, photography though illustrative has the tendency to over emphasize brighter regions in the plasma medium. Therefore it was decided to observe the plasma with photodiodes, which have a large dynamic range and do not have this problem.
First the principles of the method will be explained, after which an experiment will be described and interpreted.

Assume that the vacuum arc consist of a main diffuse plasma background with a emission coefficient E_d. In this diffuse plasma there are a large number of arc channels with an emission coefficient E_o.
In side-on observation of the plasma, (see figure 2.11) the intensity, I, will be:

$$I = \int_{-L}^{L} \varepsilon_d \, dx + N \cdot \int_{-R}^{R} \varepsilon_0 \, dx \qquad (2.1)$$

in which N is the number of arc channels in the observation path.
Fluctuations in the intensity will be a result of the motion of arc channels through the observation volume.

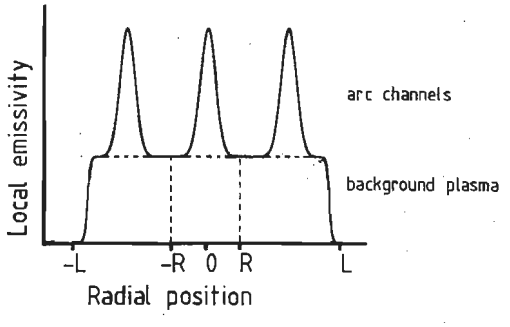

Figure 2.11 Simplified local emmissivity in the diffuse vacuum arc.

The light intensity, I, can now be split into a mean intensity component, $\bar{I}$ proportional to the mean number of arcs, $\bar{N}$ and a fluctuating intensity component, $\tilde{I}$ which is proportional to the fluctuating number of arcs, $\tilde{N}$.
Here, the "relative fluctuation level", RFL, of the arc is defined as the ratio between fluctuating part of the light intensity and the mean intensity:

$$RFL = \frac{\tilde{I}}{\bar{I}} = \frac{\tilde{N}}{\bar{N}} \times (1 + A)^{-1} \qquad (2.2)$$

in which $$A = \frac{\int_{-L}^{L} \varepsilon_d \, dx}{\bar{N} \cdot \int_{-R}^{R} \varepsilon_0 \, dx}$$

The factor A indicates the relative importance of the ambient plasma compared to that of the plasma in the arc channels, and the relative fluctuation level is a measure for this quantity. For instance, in a multiple arc with no significant ambient plasma A approaches zero and the RFL reaches a maximum; in a diffuse arc A tends to infinity and the RFL becomes zero.

Now an experiment is described of a 10 kA vacuum arc between copper electrodes of 60 mm diameter with a clearance of 10 mm. This arc passes through several stages with increasing magnetic field; namely anode spot, diffuse appearance and multiple arc regime.
The light intensity is measured with the setup given in figure 2.12. as a function of the magnetic field for a fixed value of the current, 10 kA.
The fixed current value offers the experimental advantage of a constant total number of cathode spots and so the number of arcs emanating from the cathode is independent of the magnetic field strength.

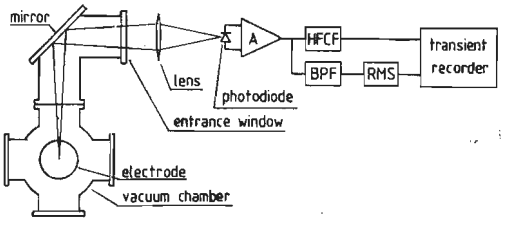

Figure 2.12 Experimental setup used to determine the relative fluctuation level in the high current vacuum arc. a.: Amplifier; HFCF: High Frequency Cutoff Filter; BPF: Band Pass Filter; RMS: Root Mean Square.

The light flux, emitted by the vacuum arc and recorded from the photodiode by a digital transient recorder the "Biomation 8100" is represented in figure 2.13a.
The basic waveform resembles that of the current wave, with high-frequency fluctuations superimposed on it.
The frequency spectrum of this light flux, obtained by Fourier transformation, is represented in figure 2.13b.

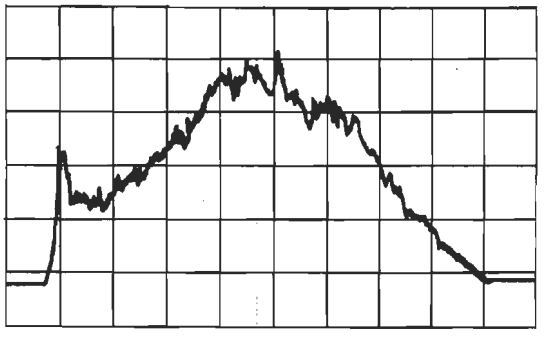

Figure 2.13a Light flux (in arbitrary units a.u.) of a 10 kA arc at 50 mT as a function of time measured with photodiode shown in fig. 2.12 (horizontal axis 1.2 ms/div.).

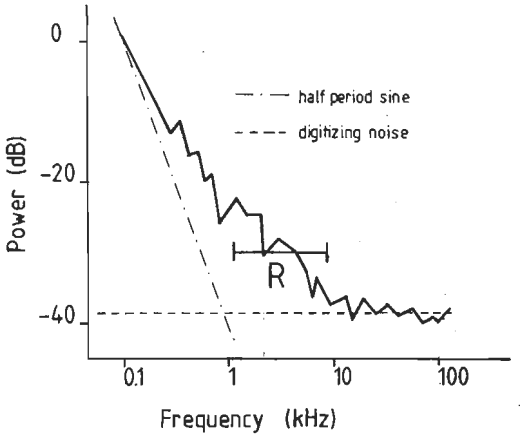

Figure 2.13b The power spectral density on a logarithmic scale normalized to the main frequency component at 100 Hz of the intensity represented in fig. 2.13a.

Here one distinguishes between a low frequency peak associated with the basic waveform of the current (a half period of a sine), a white noise component introduced by the digitizing process and a fluctuation spectrum, 1 - 10 kHz.
The latter can be attributed to the movement of cathode spots together with their arc channels through the observation window. Knowing the velocity of the cathode spots (Gun 72, She 73, Gun 78) the average time interval necessary for a cathode spot to cross the observation window can be estimated. The corresponding frequency range is given in figure 2.13b with capital R.

The relative fluctuation level has been determined with the experimental setup shown in figure 2.12.
The signal of the photodiode passes through:

1. a high-frequency cut-off filter (hfcf) to a digitizing transient recorder: yielding the mean intensity.
2. a band pass filter (bpf) with a cutoff and cuton of 20 dB/octave, passing frequencies within the range of R to an RMS meter with a response time of 2 ms. The output is stored in the same transient recorder: yielding the fluctuating intensity.

The relative fluctuation level has been calculated from these two signals according to equation 2.2.

The relative fluctuation level of a 10 kA arc measured as a function of the axial magnetic field strength is represented in figure 2.14.

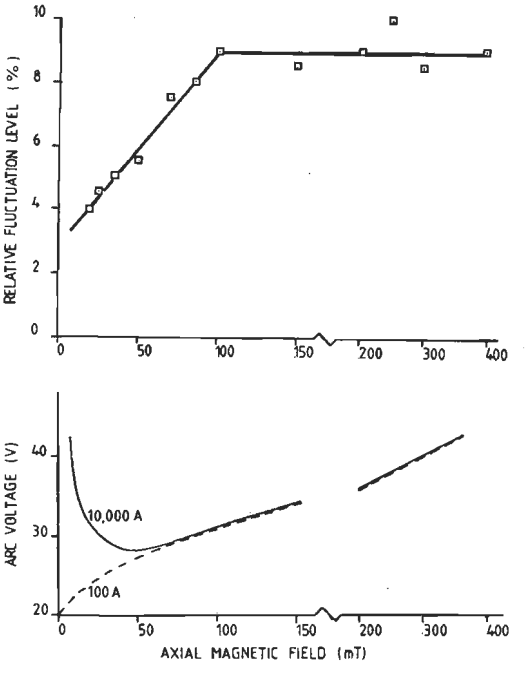

Figure 2.14 The relative fluctuation level for a 10 kA arc between 60 mm diameter copper contacts as a function of the axial magnetic field.

Figure 2.15 The arc voltage of a single 100 A arc and of a 10 kA arc as a function of the axial magnetic field.

It first increases with the magnetic field strength and saturates at a value of 10% for magnetic field strengths in excess of 100 mT. At these large magnetic field strengths the arc voltage is independent of the current, which indicates that the individual arc channels do not interact

with each other or with the background plasma. This type of arc has already been called the multiple arc.
Below 100 mT the relative fluctuation level decreases with decreasing magnetic field. This indicates that the background plasma density has become comparable to the density in the arc channels.
The difference between the arc voltage of a 10 kA arc and the arc voltage of a single 100 A arc (Gun 78) increases also with decreasing magnetic field, see figure 2.15. This means that the arc not only gets a positive current-voltage relationship but also a diffuse appearance and hence correctly can be called diffuse.
Figure 2.16 represents the dependence of the relative fluctuation level at the axial position. Here it is shown that the

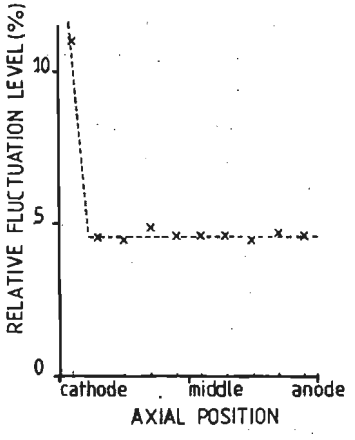

Figure 2.16 The relative fluctuation level as a function of axial position for a 10 kA arc at 25 mT.

relative fluctuation level is independent of the distance to the cathode except for the region just above the cathode.
At some distance away from the cathode the relative fluctuation level depends only on the number of arc channels within a given observation path (see also equation 2.2), and as the number of individual arc channels does not change with axial position, the relative fluctuation level has to be independent of the distance to the cathode. This is confirmed by the experiments.
This also means that below 100 mT the 10kA vacuum arc is diffuse everywhere except close to the cathode.
Very close to the cathode the RFL increases rapidly. Thus here the plasma is not anymore diffuse, but rather consists of more or less separate arc channels in a background plasma of much lower density. This is caused by the fact that, although the background plasma is probably the same near the cathode as in the diffuse part, the density in the arc channels is much higher in the cathode region. This increase of the RFL close to the cathode is found for all magnetic field values investigated.

2.5 Concluding remarks

The description of the vacuum arc has to be given for three different situations.
At low current the density of the background plasma is so low, that no interaction exists between the high velocity vapour jets emitted by the cathode spots and the background plasma.
This kind of arc is called the multiple arc.
With increasing axial magnetic field the density within the jet increases.
So the density level at which interaction occurs between the jets and the background plasma increases also.
Therefore the multiple arcing mode extends to higher currents with increasing magnetic field.

When interaction occurs between the jets and the background plasma, this is first noticed in the relative fluctuation measurements and, if the interaction is sufficiently strong, also in the arc voltage measurements.
From this moment on it seems inappropriate to describe the behaviour of the plasma in terms of jets and background plasma, as the densities in both, jet and background plasma, have become comparable.
Instead the vacuum arc plasma can be treated as a diffuse plasma filling the whole region between the electrodes. This will be the approach to the vacuum arc in this thesis. This treatment of the vaccum arc is thus restricted to the high current vacuum arc at moderate magnetic field strengths, where the arc is diffuse.
At very high currents an anode spot forms. The formation of the anode spot itself will not be studied, as it is avoided because of its devastating effects.
A mechanism which may lead finally to the formation of the anode spot will be discussed.

3. THE EXPERIMENTAL ARRANGEMENT

A diagram of the set up is given in figure 3.1 with a list of the most important external parameters. Figure 3.2 shows the entire experimental arrangement.

3.1 The vacuum chamber

All experiments were performed in a stainless steel vessel of 130 mm diameter and 5mm wall thickness. The vacuum chamber has four observation ports with a ratangular cross section of 27 x 56 mm^2 at the same level as the electrodes.
On the flanges of the observation ports an elbow is connected in which a mirror is placed. The deposition of cathode material on the mirror during arcing allows optical diagnostics for several thousand arcing operations without the need for replacing either the mirror or the entrance window. (c.f. chapter 4.1) Figure 3.3 shows a picture of the electrodes made with a camera looking through the elbow.
Due to the deposition of droplets which scattered the light the mirror is less successful in experiments with laser interferometry (c.f.chapter 4.2).

The electrodes used are made of oxygen free high conductivity copper and have a diameter of 60mm with a clearance of 10 mm. The arc is initiated by a high voltage breakdown between a trigger electrode, and the electrode, in which the trigger is placed; usually the cathode. The trigger discharge causes a breakdown of the main vacuum gap and thus initiates the main arc.
The pressure of residual gas in the vacuum chamber is held lower than 10^{-3} Pascal by a combination of a rotary and a turbo molecular pump. Although the pressure of the copper vapour plasma reaches values of 10^{4} Pascal between the electrodes during arcing, the pressure of the residual gas did not rise above 3.10^{-3} Pascal. The pressure of the residual gas was measured by a Penning-ionization gauge which was shielded from the arc by a metal labyrinth.

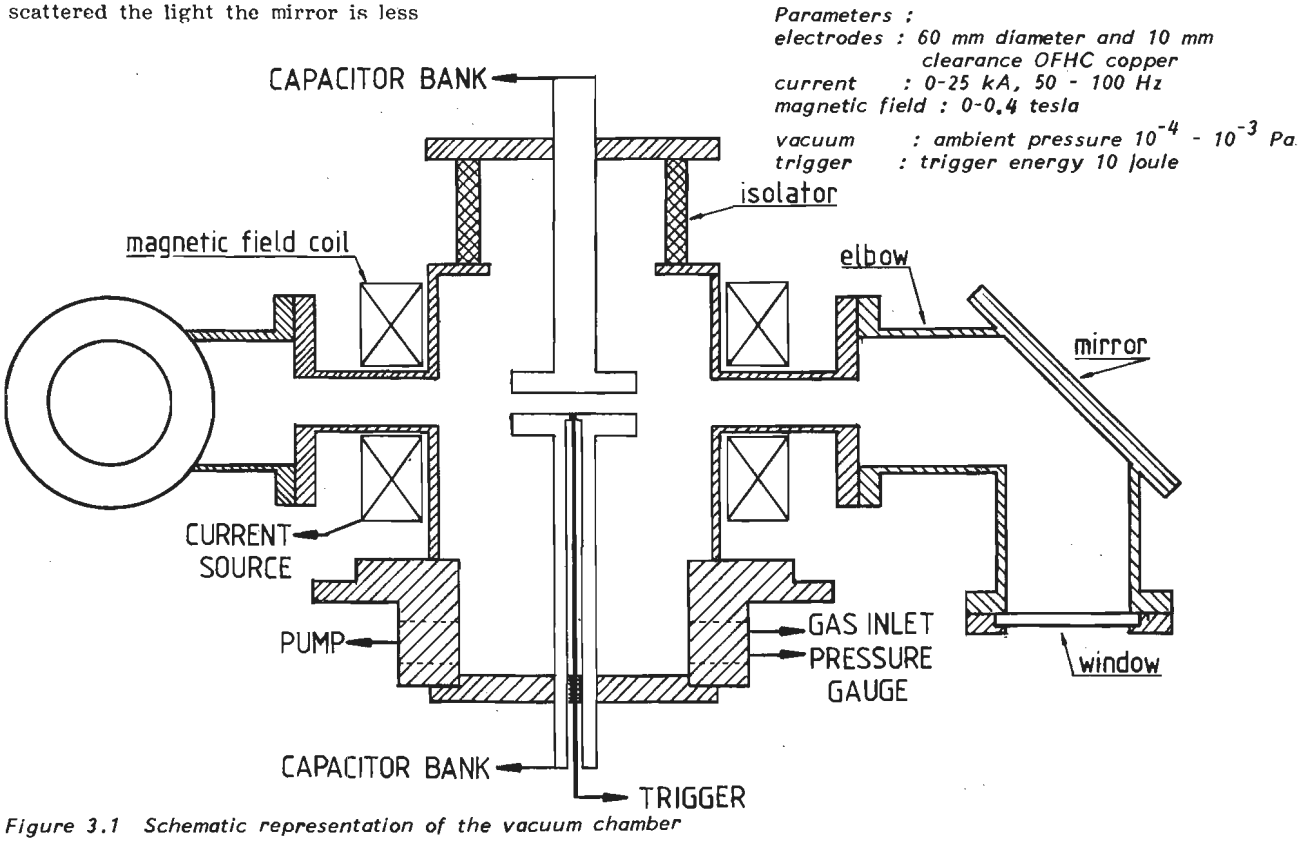

Figure 3.1 Schematic representation of the vacuum chamber

Figure 3.2 Photograph showing the vacuum chamber with the experimental set up used with the time resolved spectroscopy on the foreground.

3.2 The power supplies.

The discharge current supply consists of a capacitor bank of 20 mF at 2.5 kV connected in series with a variable inductor. With this setup sinusoidal current pulses could be made with a maximum current of 13 kA at a frequency of approximately 45 Hz and of 29 kA at a frequency of 100 Hz. The impedance of the arc, is 1 to 2% of the circuit impedance, so that the shape of the current pulse was virtually independent of the discharge behaviour. The current was measured by recording the voltage drop across a calibrated resistance of 10^{-4} Ohm.

The axial magnetic field is generated by a constant current through two coils which produced a nearly homogeneous field.
At the edge of the electrodes the magnetic field strength amounts to 98% of the magnetic field strength in the middle of the electrodes.
The current is supplied by a 80 kW

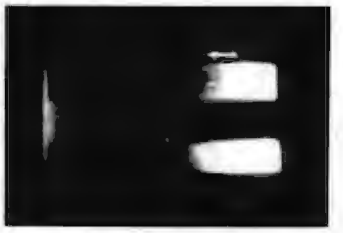

Figure 3.3 Photograph of the electrode arrangement made through an elbow with copper mirror.

rectifier (3 phases) with which a maximum magnetic field of 400 mT can be reached. The ripple amounts to 4% outside the vacuum chamber but due to eddy currents in the large copper contacts the ripple in the middle of the arc was less than 2%.
By placing a capacitor bank parallel to the rectifier the ripple can be reduced to less than 0,1% which was especially important in the case of the diamagnetic loop measurements (cf.chapter 4.3).

3.3 Parameter Range.

The main interest of the present study is the diffuse vacuum arc. Therefore three combinations of arc parameters are chosen out of the parameter range of the diffuse arc;
see figure 1.2.

1. The diffuse vacuum arc in absence of an axial magnetic field in the current range from 3 to 8 kA
   An anode spot forms at 9 kA (50 Hz). see figure 2.1.
2. The diffuse vacuum arc in an axial magnetic field of 50 mT with the current range from 10 to 23 kA
   An anode spot forms at 24 kA (100 Hz) see figure 2.1.
3. The diffuse vacuum arc at 10 kA with axial magnetic fields from 8 to 100 mT
   An anode spot forms at axial magnetic fields smaller than 7 mT see figure 2.11.

The last mentioned combination of parameters is explored most thoroughly.

4. DIAGNOSTIC METHODS

In this chapter the diagnostic methods used to determine the plasma parameters are described. There is literature available about similar experiments in vacuum arcs, but the information about the parameters is not always consistent, partly because the external circuit parameters are not always comparable.
The electron temperature values reported in the literature vary from 7000 K in a high current vacuum arc in an axial magnetic field (Kan 81) to around 250.000 K in a 100 A arc with anode spot (Gri 74). Therefore the spectroscopic measurements described in section 4.1 are designed to establish, which kind of electron temperature measurements is applicable under the present experimental conditions. In this thesis the electron temperature will be given in electron volts, where 1eV corresponds to 11600 K.

The electron density ranges from $10^{19} m^{-3}$ in the low current vacuum arc (Box 74) to 5.10^{22} m^{-3} in the high current vacuum arc (Kan 81). The electron density has also been measured in this study.
The absolute value of the electron density was determined with a laser interferometer, which is described in section 4.2. The measurements of the continuum radiation proved to be an accurate way to obtain the spatial dependence of the electron density (see section 4.1).
High ion velocities 2.10^4 ms^{-1} are observed in low current vacuum arcs (Dav 69). These high velocities are thought to prevail also in the high current vacuum arc (Box 77, Eck 74). Electrostatic probe measurements in the afterglow of the high current vacuum arc yield values of 8000 ms^{-1} (Bau 76). The mean free path of the charged particles scales with the fourth power of the thermal velocity.
So whether the arc has to be regarded as a collisionless expanding plasma cloud or as a collision dominated plasma depends on whether the mean free path for ion-ion collisions is larger or smaller than the characteristic dimensions of the arc. In order to be able to verify whether the mean free path is small enough, as is essential for the applicability of the results of chapter 5, a line broadening measurement was designed to obtain the ion temperature and thus the ion thermal velocity. This experiment is described in section 4.4.

An attempt was made to measure the azimuthal current density distribution in the arc from the diamagnetic loop measurements, which are described in section 4.3. It will be shown in chapter 6 that in the special case of the vacuum arc also the radial current density can be obtained from these measurement and from this the current flow lines in the arc.

Although the aim of the diagnostics was to determine the electron temperature, the electron density, the ion temperature and the current density, the techniques made also possible an estimation of the neutral density, the systematic ion velocities, the effective charge and the electric field in the plasma. The various measurement techniques will be described and discussed in detail and some of the direct results will be presented.
The interrelation between the results obtained by the various diagnostic methods and the consequences of the measured data on the momentum balance will be discussed in chapter 6.

4.1 SPECTROSCOPY

The vacuum arc studied in this thesis burns on copper contacts, so that the only constituent of the plasma is copper in various stages of ionization. Such a metal vapour arc emits a line spectrum as well as free-free and free-bound continuum radiation.
The spectral intensity distribution of the radiation as a function of wavelength can give valuable information about the intrinsic parameters of the arc. In the

following at first the relationship between these parameters and the emission pattern will be explained, then the two experimental methods employed will be discussed:
- time integrated spectroscopy with a spectrograph and
- time resolved spectroscopy with a monochromator.

In the last section the results of both methods will be discussed.

4.1.1 LINE RADIATION

The total intensity of a spectral line emitted in an optically thin homogeneous plasma of length L is proportional to the the upper excited state density:

$$I_{pq} = n_p A_{pq} h\nu_{pq} l/4\pi \qquad (4.1)$$

where n_p is the density of the upper state

A_{pq} is the transition probability

$h\nu_{pq}$ is the photon energy

For a non homogeneous plasma the intensity is proportional to the density of the excited state integrated along the line of sight. When the plasma is rotationally symmetric, an evaluation of the excited state density from the line intensity is possible by the Abel-inversion method. (Loc 68, Kas 78).
In the case of local thermal equilibrium (LTE) the density of the excited state is coupled to the density of the ground state by the Boltzmann equation.

$$\frac{n_p^B}{g_p} = \frac{n_o}{g_o} \exp\{-E_{po}/kT_e\} \qquad (4.2)$$

where E_{po} is the energy difference between the ground state 0 and the excited state p, and g is the statistical weight of the excited state, and kT_e is the thermal energy of the electrons.

If all the levels of the system are in LTE, the electron temperature can be obtained from the slope of a so called Boltzmann plot. In this plot the logarithm of the excited state densities, n_p, divided by their statistical weight, g_p, are plotted against the excitation energy.

With the Saha equation the excited state density of the atomic system with charge Z can also be related to the density of the next ionization stage with charge Z+1:

$$\frac{n_{z,p}^S}{g_{z,p}} = \frac{n_{z+1,o}}{g_{z+1,o}} \frac{n_e}{2} \left(\frac{h^2}{2\pi m_e kT_e}\right)^{3/2} \exp\{-\chi_{z,p;z+1,o}/kT_e\} \qquad (4.3)$$

where:

n_e is the electron density and

$\chi_{z,p;z+1,o}$ is the ionization energy of level p to level 0 in the atomic system with charge Z+1.

In this case the equilibrium is denoted by PLTE, as the lower levels do not necessarily need to be in Saha equilibrium with the Z+1 ground state.
Usually PLTE is reached for far lower electron densities then LTE. This is mainly a consequence of the large energy gap between the ground state and the first excited state.
When in a Boltzmann plot method only excited states are used, only PLTE is needed; LTE is not necessary.

Experiments in a wall stabilized electric arc show that the CuI system reaches LTE at an electron density of $4.10^{22} m^{-3}$ in the case of optically thin resonance lines (Koc 68). Although the resonance lines are strongly absorbed in the vacuum arc studied here, the electron density is too low (in the range of 2.10^{21}–$7.10^{21} m^{-3}$) to have LTE in the CuI system. Due to the greater energy gaps between the various excited levels in the CuII-scheme compared to the CuI-scheme, LTE is certainly excluded in CuII.
The problem of the population of excited states not in LTE has to be treated within the frame work of a collisional radiative (CR) model.
In CR-models the density of the m-th excited state is described by an equation of the form

$$n_m = R_m^0 n_m^S + R_m^1 n_m^B \qquad (4.4)$$

in which n_m^S is the level density according to the Saha equation 4.3 and n_m^B the density according to the Boltzmann equation 4.2. The coefficients

R_m^0 and R_m^1 are the so called collisional radiative coefficients depending on the atomic system. A complete CR-model was made for an aluminum vacuum arc to explain observed level densities (Box 80. Gol 80).
Van der Mullen e.a. (Mul 81) discusses extensive CR-model calculations for hydrogen (Fui 72) and measurements in argon (Mul 80). The existence of a relatively simple systematic trend for the excited state densities, which is called the complete excitation saturation (CES) phase, is evident in many atomic systems at electron densities lower than those required for PLTE. The CES-phase is due to the dominance of collisional (de)excitation over radiative processes far before the considered levels come into Saha-equilibrium with the next ionization stage.
In this concept R_m^1 saturates (i.e.becomes independent of the electron density in contrast to the Corona-phase) and is only weakly dependent on T_e. For ionizing plasmas with overpopulated ground states there is an upward flow of excitation. Because the energy difference between neighbouring levels decreases for higher lying levels (lower ionization energy, E_m^{ion} and consequently the electron excitation cross-section increases, the density of an excited state becomes proportional to the X-th power of the ionization energy:

$$n_m \sim (E_m^{ion})^X \qquad (4.5)$$

The value of X has been calculated for hydrogen (Fui 79) and for non hydrogenic systems (Mul 81, Sij 82) and has been measured for argon (Mul 80) and lies between 2.75 and 3.25.
Instead of using the ionization energy of a specific excited state, the effective quantum number, p, will be used in order to compare the results obtained from the vacuum arc with those presented in literature.
The effective quantum number is defined as (Mul 81)

$$p = \sqrt{R_\infty / E_{ion}} \qquad (4.6)$$

in which R_∞ is the Rydberg constant.

With increasing electron density the high lying levels begin to enter the LTE-phase and are in Saha-equilibrium with the continuum while the lower lying levels are still in the CES-phase. If all the excited levels are in equilibrium with the continuum, and the groundstate is overpopulated, the atomic system is said to be in partial local thermal equilibrium (PLTE). This situation has already been discussed above.

The discussion above shows that evaluation of the electron temperature from the intensity of a spectral lines is possible only when the relevant levels are in PLTE.

4.1.2. Absorption of spectral lines

In the case of self-absorption of spectral lines the relation between the intensity and the excited state density becomes more complicated. Several methods exist to determine the absorption parameter, $k_o l$, of a spectral line.

1. The absorption parameter can be determined by means of an externally modulated light source by measuring the transmission of the plasma with a phase sensitive detector. Drawbacks of this method are the need for a sufficiently strong light source and the lack of integration time due to the pulsed nature of the arc. A way out is to place a mirror at the opposite side of the absorbing medium and to compare the line intensity with and without mirror(Dra 73, Ros 81). This method is used in the line broadening measurements (cf section 4.4.)
A difficulty remains to ascertain the intensity of the reflected component.

2. The ratio of the intensity of two spectral lines corresponding to atomic transitions ending on the same level depends on the absorption parameter (Jol 75).
Let I_{01} and I_{02} be the total intensities emitted by these lines in the absence of absorption. The line for which the oscillator strength is strongest (which will be denoted by subscript 1) will be more strongly absorbed than the other line.
With the assumption of a homogeneous medium in the direction of observation

and the same line profiles for emission and absorption, the ratio of the total selfabsorbed intensities, I_1/I_2, depends on the population of the absorbing level according to the expression:

$$R = \frac{I_1/I_2}{I_{10}/I_{20}} = \frac{k_{02}W(k_{01}l,a_1)}{k_{01}W(k_{02}l,a_2)} \qquad (4.7)$$

The equivalent width of the line, $W(k_0l,a)$, is a function of the absorption parameter and a, the ratio of Lorentz to Gauss broadening of the line.
For two lines ending on the same level the absorption coefficients are related to the oscillator strengths, f_i:

$$\frac{k_{01}}{k_{02}} = \frac{f_1}{f_2} \qquad (4.8)$$

so the ratio R depends only on a single unknown k_{01}, because the parameters, a_1 and a_2, determining the line profile depend on the state of the plasma e.g. temperature and densities. The absorption parameter is found from the ratio between the measured ratio of the line intensities and the calculated ratio of the line intensities.

4.1.3. Continuum

The total continuum emission coefficient is for a singly ionized plasma given by:

$$\varepsilon_{\lambda,c} = \varepsilon_{\lambda,ff} + \varepsilon_{\lambda,fb} = \qquad (4.9)$$

$$= \frac{1.638\ 10^{-43}\ n_e^2}{\lambda^2 \cdot \sqrt{T_e}} \cdot \{\xi_{fb}(1-\exp(-hc/\lambda kT_e)) + \xi_{ff}\exp(-hc/\lambda kT_e)\}$$

The terms proportional to the so-called ksi-factors, ξ_{fb} and ξ_{ff} describe the contributions of the "free-free" radiation or "bremsstrahlung", due to elastic electron-ion collisions, and of "free-bound" radiation, due to radiative recombination.
The factor ξ introduces the influence of the specific electronic structure of the considered atom in the expression for the continuum radiation.
Both factors have been published for some gases, but are unknown for neutral copper. From electron density measurements it is concluded that both ksi-factors are close to 1 for copper in the spectral range between 290 nm and 340 nm.

4.1.4. Selection of spectral lines

The selection of spectral lines was made acoording to the following criteria. Only those lines were measured:

- which emerge from various excitiation levels in order to make a check on the state of the atomic scheme (PLTE or CSE) possible.
- which end on the same sublevel but with different transition probabilities in order to check the degree of selfabsorption.
- of which the transition probability was measured (Bie 75, Koc 68) or could be calculated with the Coulomb approximation (Bat 49)
- which lie in the wavelength interval of 200-400 nm because of the optimum wavelength resolution and sensivity of the measuring equipment.

TABLE 4.1 The selection of spectral lines

wavelength nm	copper system I/II	transition probability calculated 10^8 sec	transition probability measured 10^8 sec	excitation energy eV
333.8	I		0.0038	5.1
330.8	I	0.72	0.43	8.82
330.1	II	0.56		18.09
329.0	II	.59		18.09
327.4	I	1.68	1.36	3.79
324.7	I	1.75	1.37	3.82
296.1	I		0.0376	5.59
283.8	II	1.47		13.42
282.4	I		0.0783	5.78
277.0	II		0.61	13.39
271.3	II	0.852	0.68	13.43
270.3	II	0.837	1.18	13.65
268.9	II	0.99	0.41	13.39
264.4	III	2.29		15.72
261.8	I		0.307	6.12
260.9	III	-		
254.4	II		1.10	13.39
252.2	III	2.55		15.94
250.6	II	1.75		13.43
249.2	I		0.0306	4.92
248.9	II		0.0145	8.23
248.2	III	1.7		14.95
244.2	I		0.0185	5.06
241.2	III	2.77		15.76
240.6	I/III			
240.0	II	0.244		8.42
239.2	I/III			
237.0	II		0.715	8.49
235.7	II	0.0322		8.23

The lines that fulfil these demands are represented in tabel 4.1 and in figure 4.1 and 4.2 where they are drawn in the atomic energy level diagrams of CuI en CuII.
With the lines mentioned above the largest parts of the atomic energy level diagrams of CuI and CuII are covered. Also some lines of CuIII were measured but these all emanated from groups of levels lying closely together and gave therefore no representative picture of the excited state density distribution within the CuIII system.

4.1.5. Measurement methods

4.1.5.a. Time integrated spectroscopy

In figure 4.3. the experimental set up with the spectrograph is given schematically. The arc is focussed on the entrance slit of the spectrographwith a 200 mm focal length quartz lens giving a magnification of ½. Parts of the optical system are also a copper mirror placed inside the vacuum chamber, a quartz vacuum window, and a high reflectivity aluminum mirror which allowed spatially resolved measurements.
The copper mirror consisted of a substrate of glass that was continuously exposed to the arc and hence became covered with arcing products, copper atoms and droplets. After exposure to arcs which carried a total of 5.10^4 Coulombs the reflectivity of the Cu-mirror did not change any more. This mirror arrangement prevented deposition of arcing products on the quartz window.
The quartz spectrograph, type Hilger and Watts, has an opening angle of .0.63 rad and a dispersion ranging from 0.4 nm/mm at 200 nm to 3.5 nm/mm at 400 nm.
In the focal plane of the spectograph a cassette with a photographic plate type Kodak spectrum analysis nr. 1 with a resolution of 100 lines per mm and sensitive for the spectral range from 200 up to 450 nm was placed. The width of the entrance slit (0.1 mm), was chosen to be the largest of apparatus profile (0.03 mm) and spot diameter of a microdensitometer

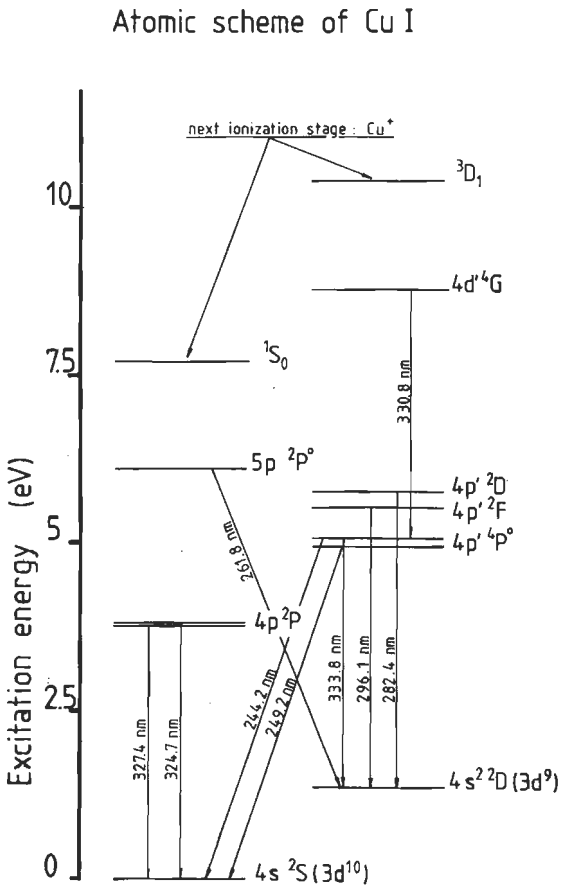

Figure 4.1 Schematic of the atomic energy level diagram of CuI showing the optical transitions studied in this thesis.

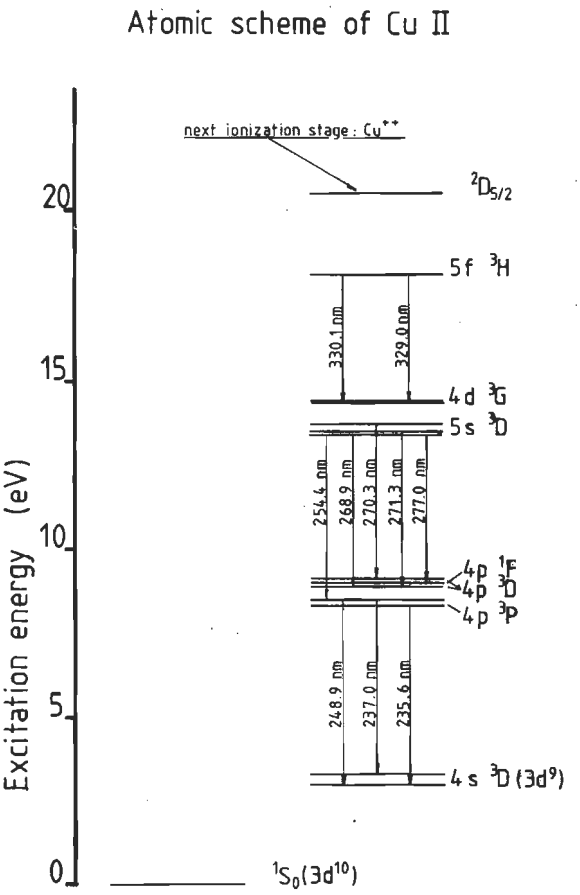

Figure 4.2 Schematic of the atomic energy level diagram of CuII.

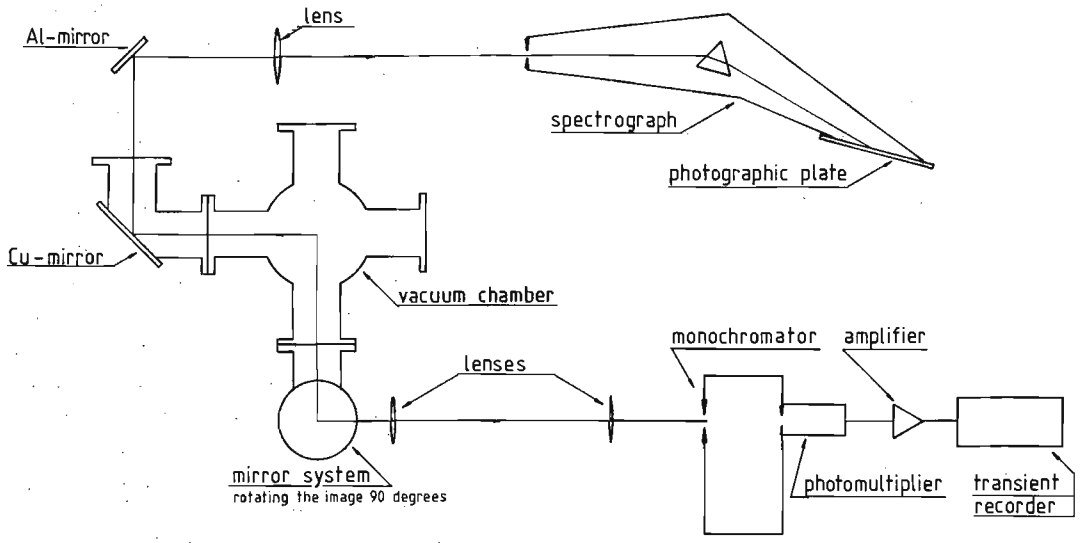

Figure 4.3 Experimental set up used in the spectroscopic study.

(0.025 mm). In this way no correction on the measured total line intensity for the apparatus profile is needed. The height of the entrance slit was larger than the length of the image of the arc in order to photograph the whole arc in axial direction. By moving the Al-mirror between the exposures a lateral survey could be made. Figure 4.4 shows three photographic plates made in this way. Each of the twelve exposures displays the arc at a different lateral position.

The blackness or density of the photographic plate is dependent on the emulsion, the development method, the spectral composition of the light and its

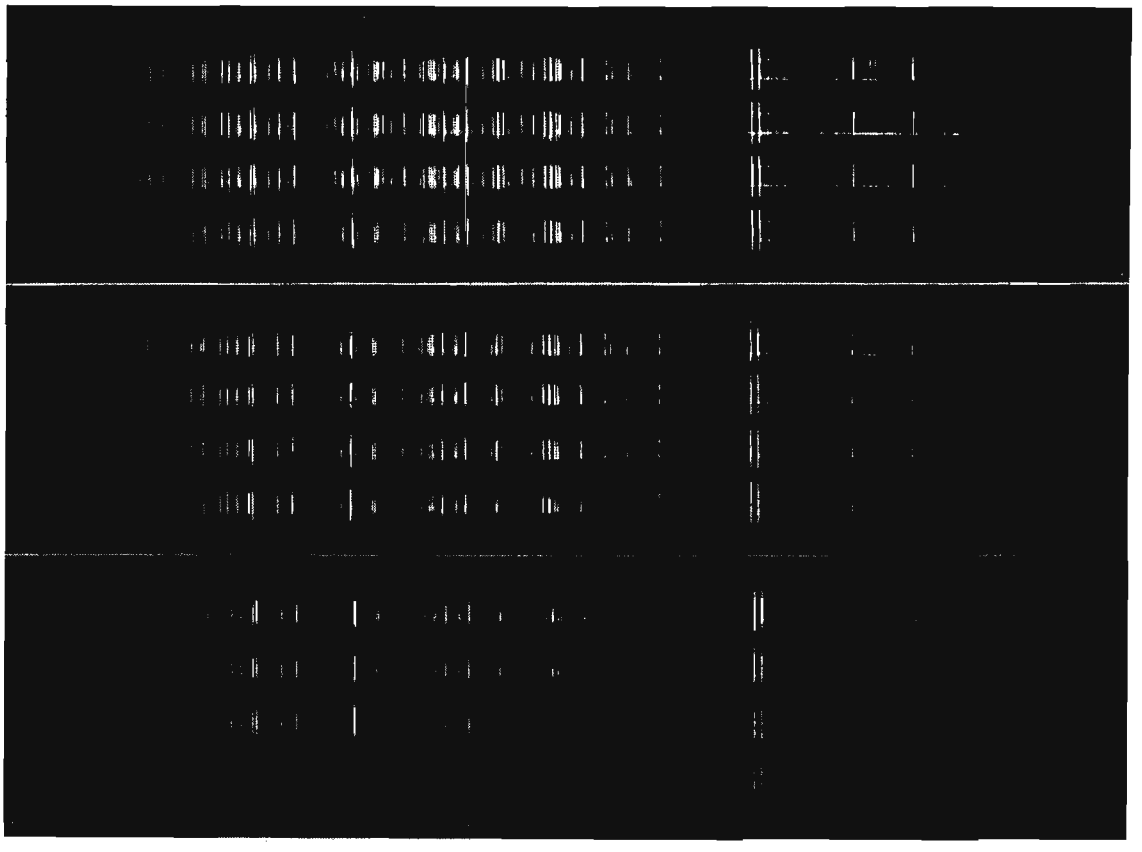

Figure 4.4 Three photographic plates showing twelve exposures of the arc spectrum at various lateral positions . Each exposure reveals horizontally the spectrum (from left to right : UV 210 nm to visible 450 nm) and vertically the axial intensity distribution (above: anode; below: cathode).

radiance. Only one type of photographic plates was used and they were all developed at one time during 9 minutes in microdol developer (1 : 3).
This resulted in a very low fog (the density of the support plus the density of the unexposed but processed emulsion) and also in a low contrast index(the slope of a straight line drawn between two points on the curve : density versus logarithm of the intensity) thus increasing the useful intensity range of the photographic plate .
The relationship between the density and the time integrated intensity was determined with a calibrated tungsten lamp placed in the position of the arc. In the U.V. the radiance of the lamp is much lower than the radiance of the arc, therefore integration times up to 15 minutes were needed to get the same density as with the arc. The density of the lines listed in table 4.1 were measured on various lateral and 5 axial positions with the Very Automatic Micro Photometer of the University of Utrecht, which made the results accessible for a large computer.
An IBM computer converted the density into intensity and after Abel inversion into the local emissivity (Kas 78, Pat 79).

4.1.5.b. Time resolved spectroscopy

In figure 4.3 also the optical system and the electrical measurement circuit used here for the time resolved spectrocopic experiments is shown. The lens system images the arc on the entrance slit (0.1 mm x 3 mm) of a monochromator (spectral resolution 6.8 nm/mm) in such a way that the slit is parallel to the electrode surface. The solid angle of detection is about .003 sterad.
The intensity of the light is measured with a photomultiplier (RCA-IP28).
The photon pulses are counted and stored after amplification in a Biomation 8100 transient recorder.
In this device the A.D. convertor was replaced by a comparator and a counter. The input amplifier offset of the Biomation and the comparator acts a discriminator. The photons are counted during 0.01 ms intervals and their numbers are stored in a 2 kbyte memory. This gives a maximum sensitivity coupled to a good time resolution with the posiibility of time integration afterwards. Correction for the deadtime (140 nsec) is made with a desk computer HP 9820.
Because of the poor spectral resolution of the monochromator only the intensity of isolated lines could be measured.
Therefore the CuI 296.1 nm and the CuII 277.0 nm line were chosen. Also the continuum at 290 nm and at 345 nm was measured. Calibration of the whole system was performed with a tungsten ribbon lamp.
In order to get a detailed picture of the arc the intensity at the above mentioned wavelengths is measured at 3 different distances with respect to the cathode and at 12 lateral positions. The photons counted during each millisecond of the 10 msec arc duration were summed after dead-time correction. An IBM-computer handled these data in the same way as in the case of time integrated measurements.

4.1.6 Results and Discussion

Accuracy: Calibration errors amounted to 10-25% depending on the wavelength and the measurement method and are the largest for the spectograph. Due to the approximately 10% shot to shot variation an additional error ±30% was introduced with curve fitting through the lateral measured points and subsequent Abel inversion. The difference between the time integrated intensity as measured with the spectograph and the time integrated intensity measured with the monochromator is less than 20% which is well within the calibration error.

Excited state densities

Figure 4.5 represents the excited state densities of the atomic energy levels of CuI and CuII at 10 kA 25 mT. The logarithm of the excited state density is plotted against the excitation energy, yielding the Boltzmann-plot, and against the logarithm of the main quantum number p, yielding a check on the CES phase.
This is done for the excited state densities at the arc axis for 5 axial positions: 1, 3, 5, 7 and 9 mm above the cathode. In the Boltzmann-plots the distribution temperatures are given, denoted by T_d in figure 4.5, and in the other plots the exponent x of equation 4.5. Although only one point is given at high excitation energy in CuI, it seems

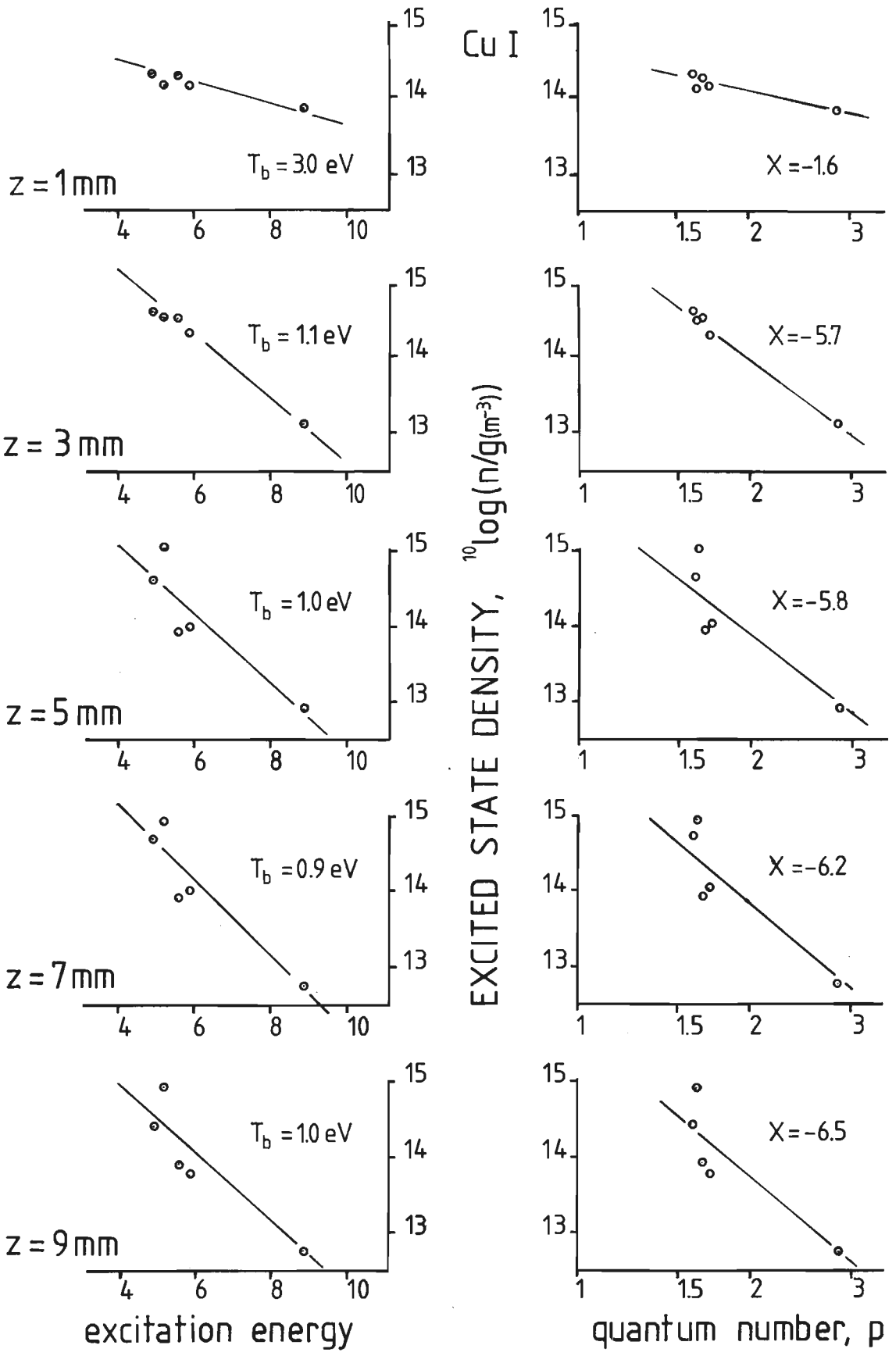

Figure 4.5a Graphic of the excited state densities of CuI versus the excitation energy, which yields the Boltzmann-plot, and versus the main Quantum number p, which yields a check on the existence of the CES phase. Experimental conditions : 10 kA, 25 mT. Densities measured at the arc axis on 5 axial positions: 1, 3, 5, 7 and 9 mm above the cathode.

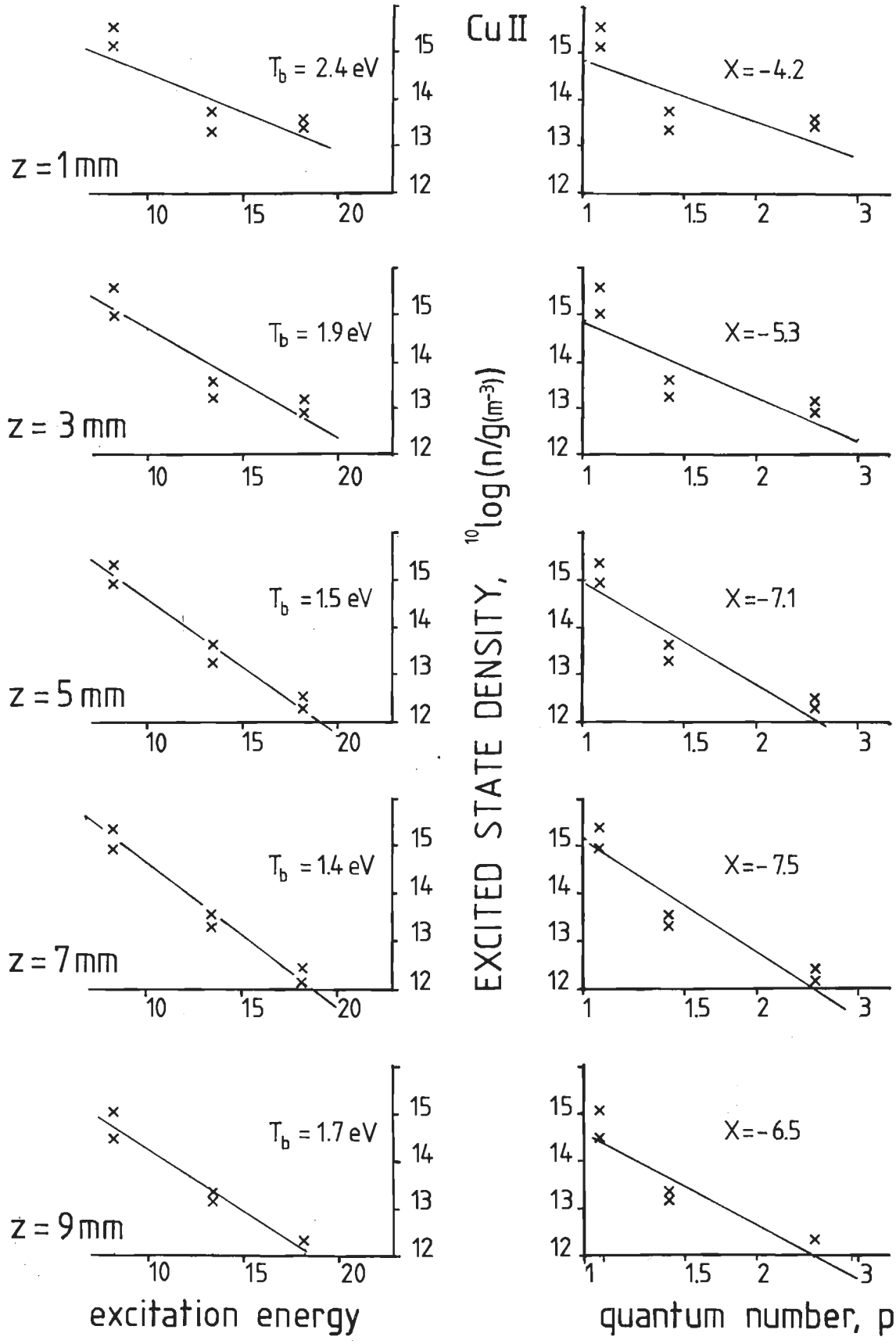

Figure 4.5b Graphic of the excited state densities of CuII versus the excitation energy, which yields the Boltzmann-plot, and versus the main Quantum number p, which yields a check on the existence of the CES phase. Experimental conditions : 10 kA, 25 mT. Densities measured at the arc axis on 5 axial positions: 1, 3, 5, 7 and 9 mm above the cathode.

justified by the accuracy of the measurement to conclude that close to the electrodes the highest excited levels are in Saha equilibrium with the next ionization stage, making the determination of the electron temperature possible once the density of singly ionized copper is known. Further away from the electrodes the CuI system is in CES phase because of the observed relation $n \sim p^{-6}$ At all positions CuII atomic energy levels are in complete saturation excitation phase except the highest excited levels at 18 eV near the cathode.

Electron temperature:

In the CES-phase the density of the excited state is proportional to the density according to Boltzmann $n_m = R^1_m \cdot n^B_m$, which is directly related to the ground state density. If the plasma is singly ionized then the electron-temperature can be deduced from the density of an excited state of an ion:

$$n_m = R^1_m \, n_e \cdot \exp\{-E^{exc}_m / kT_e\} \qquad (4.10)$$

since $n_e = n_i$

The coefficient R^1_m can be calculated at places where the temperature is determined with other means, when it is assumed that R^1_m is dependent of density and temperature.

Near the cathode the upper levels of the CuI diagram are in Saha equilibrium. This leads to a temperature of approximately 2.7 eV for all the arcing parameters studied. Because the levels at 13.4 eV in the CuII diagram are in the CES phase, the coëfficient R^1_m is determined to be $5.2\ 10^{-5}$ for the $5s\ ^3D_3$ level (see fig. 4.6).

With this value the temperature everywhere else in the arc is determined. In fig. 4.7 the axial and radial temperature profile is given for the 10 kA 25 mT arc. The error amounts to 0,3 eV and therefore the temperature can be considered independent of radius and axial position.

In figure 4.8 the time dependence of the temperature is given for a 10 kA 15 mT and 100 mT vacuum arc. The electron temperature is found also to be independent of the time and thus of the current.

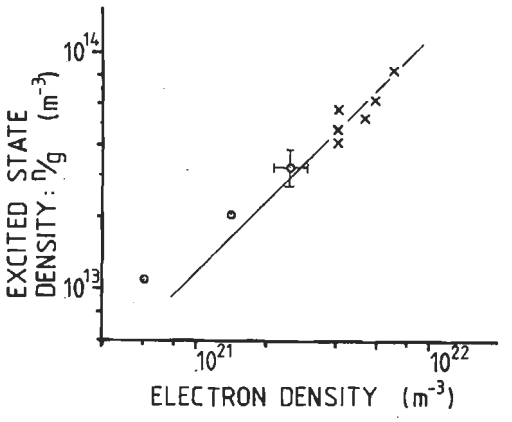

Figure 4.6 Excited state density of the levels at 13.4 eV in the CuII scheme plotted against the electron density at an electron temperature of 2.7 eV.
x: measured at current peak
o: measured in the current wave

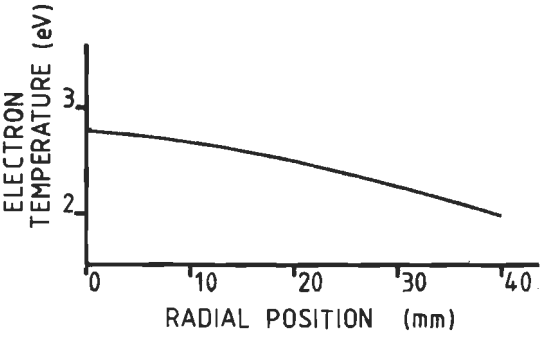

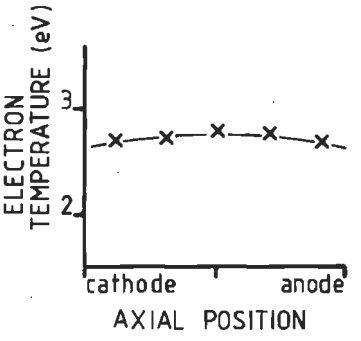

Figure 4.7 Electron temperature profiles of a 10 kA arc at 25 mT.
a: radial : halfway between the electrodes
b: axial : on the arc axis

Continuum:

Only the time resolved measurements are available because the intensity was too small to be detected by the photographic plates.

Due to its quadratic dependence on the electric density, the continuum is very suited to measure the spatial variation of this quantity. Direct measurement of the

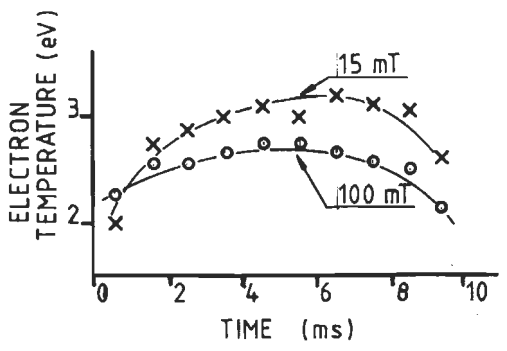

Figure 4.8 Electron temperature profile of an arc at 15 mT and 100 mT with an sinusoidal current of 10 kA peak as a function of time.

electron density with a laser inferometer (see below) made it possible to calibrate the value between the curled brackets in equation 4.8.

Figure 4.9 gives the electron density at various positions in the arc for a 10 kA vacuum arc at 15 mT.

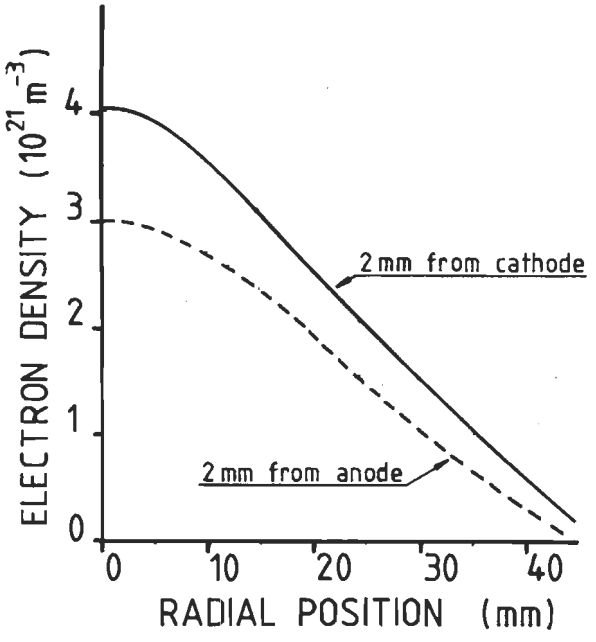

Figure 4.9 Electron density profile of a 10 kA arc at 15 mT.

Neutral density

The neutral lines at 324.7 nm and at 327.4 nm ending on the groundlevel are very strongly absorbed, so that nowhere in the arc the absorption parameter could be determined ($k_0 l > 100$). This puts a lower limit to the neutral density of 10^{20} m^{-3}. Below it is shown that the neutral density increases towards the walls, hence the absorption will be mainly in the outer regions of the arc. The spectral line emission is from the region with the highest excitation frequency, thus in the region with the highest electron density. The plasma conditions are different for the regions of emission and absorption and so it is very unlikely that the line profile of the emitter is the same as the line profile of the absorber. This seriously affects the applicability of the measurement method of the absorption parameter.

The exsistence of the CES phase in both the CuI and CuII atomic scheme makes the determination of the neutral density relative to the electron density. In cases where the electron temperature is constant the following relation exists between neutral and electron density (Pot 80)

$$\frac{n_o}{n_e} = C \cdot \frac{n_{o,4p}/g_{0,4p}}{n_{1,5s}/g_{1,5s}} \qquad (4.11)$$

In figure 4.10 the axial and radial dependence of $\frac{n_o}{n_e \cdot C}$ is given for the 10 kA arc at 15 mT.

This ratio decreases towards the arc centre. This may be caused by ionization of the neutrals leaving the cathode and a return flow of neutrals from the recombination zones near the walls.

To establish the actual neutral density additional information is needed, which is provided by the interferometric measurements described below. A discussion of the observed neutral density profile will be given in chapter 6.

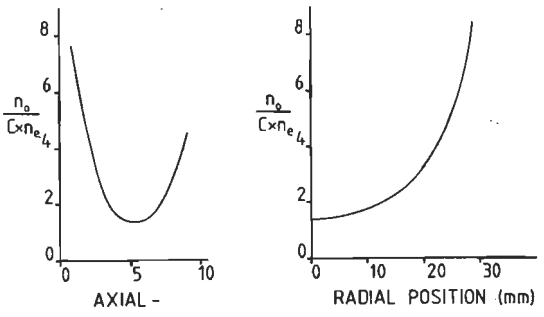

Figure 4.10 Neutral density profile relative to the electron density of a 10 kA arc at 15 mT.
a: axial : on the arc axis
b: radial : halfway between the electrodes

4.2 LASER INTERFEROMETRY

4.2.1 Measurement principle

The index of refraction of a plasma can be expressed as (Alp 59):

$$n - 1 = - \frac{e^2 \lambda_o^2}{8\pi^2 \varepsilon_o m_e c^2} \cdot n_e + \sum_k 2\pi\alpha_k \cdot n_k \qquad (4.12)$$

The first term at the right hand side represents the contribution of the free electrons and thus depends on the electron density. The second term represents the contribution of the electrons bound to the various atomic species, k, and α_k is their polarizability.
In the literature various values of the polarizability of neutral copper are given. Jolly measured the polarizability of neutral copper at radio frequencies and found a value of $23.10^{-30} m^3$. By extrapolating his findings to the visible wavelengths he suggests a value of $28 \pm 13.10^{-30} m^3$ (Jol 72).

Boxman uses a value of 10.10^{-30} m^3 in evaluating his measurements (Box 74). Fragan calculated the polarizability of copper using atomic data and found for neutral copper 91.10^{-30} m^3 and for singly ionized copper $9.6\ 10^{-30} m^3$ (Fra 71).
In this thesis the value proposed by Jolly is used, but the above data show that the absolute neutral density derived from the results may be wrong by a factor of three. The polarizability of the ions is assumed to be small compared to the polarizability of the neutrals. $\alpha_o \simeq 10 \cdot \alpha_i$

In any case the contribution of the ions is small compared to that of the electrons and can be ignored since $n_e = n_i$.

With a laser interferometer it is possible to measure the change of the length of the optical path and hence the index of refraction of the medium, traversed by the laser beam.
From equation 4.11 it can be seen that the neutral contribution is independent of the wavelength, whereas the electron contribution increases as the square of the wavelength. Therefore, measuring the refractive index at two wavelengths simultaneously, should yield both the electron and the neutral density.
The experimental complexity of a simultaneous measurement with two laser interferometers is considerable (Ros 81, Alc 66).
In the present study only one helium-neon laser was available. This laser could be tuned either on the red line at 0.63 μm or on the infra-red line at 3.39 μm
As a result of the reproducibility of the vacuum arc the above mentioned method could be applied to measure the electron density and the neutral atom density.
From a similar measurement on a vacuum arc (Box 74) neutral and electron densities are expected to be of the same magnitude. This results in mixed electron and neutral particle contributions at the red wavelength and mainly an electron contribution at the infra red wavelength.

4.5.2. Experimental set up

As stated above the index of refraction of the plasma is measured with a laser interferometer in a coupled cavity mode. The laser cavity of a HeNe-laser is coupled to an external cavity, in which the plasma across which the phase change is to be measured, is located. This setup has been used first by Ashby and Jephcott (Ash 63) and is represented schematically in figure 4.11. If the external path length

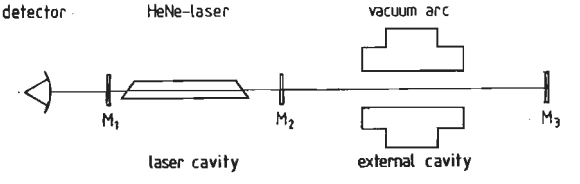

Figure 4.11 Schematic of the laser interferometer of Ashby and Jephcott.

is altered either by moving the mirror M3 or by changes of the index of refraction of the medium in the external beam, the laser output is modulated. The laser output can be measured by a photodetector at the back opposite of the laser. Maxima in the laser output occur when changes in the optical path amount to a multiple of half a wavelength. The number of maxima or fringes corresponds to changes in the densities of neutral copper and electrons along the laser beam:

$$N_{fringes} = \frac{4}{\lambda_o} \int_o^\infty (n(x) - 1)\, dx \qquad (4.13)$$

$$= - \frac{e^2 \lambda_o^2}{4\pi^2 \varepsilon_o m_e c^2} \cdot \int_o^\infty n_e(x) dx + \frac{4\pi\alpha_o}{\lambda_o} \cdot \int_o^\infty n_o(x) dx$$

From the number of the fringes at two wavelengths and with the above relationship two equations are obtained with two unknowns namely the line integral of the neutral density and the line integral of the electron density. Such a system of two equations is solvable.

4.2.2.1 The red laser interferometer

In the setup represented in figure 4.11 it is not always possible to distinguish between the increase or the decrease of the number of fringes. Therefore the zebra-stripe method was employed (Gib 64).
With this method it is not only possible to measure a whole fringe, but also fractions of a fringe and the direction of change.
The principle of the method is to introduce a cyclic change in the interferometer path and to compare this with the change introduced by the plasma. The cyclic change is produced by moving the third mirror of the Ashby-Jephcott interferometer with a piezo-ceramic cylinder, in the direction of the laserbeam. The waveform of the driving voltage for the piezo crystal is fed to the y-axis of an oscilloscope (see figure 4.12) and produces an in phase deflection proportional to the displacement of the mirror. As a consequence of this optical path change the intensity of the laser is modulated.

Each time the intensity of the laser is maximum also the photodetector output voltage is maximum.
A differentiating network gives a positive voltage pulse after the occurrence of a maximum. This signal is fed to the Z entry (beam intensity modulation) of the oscilloscope, which causes a bright pulse on the screen for every fringe. When the cyclic modulating piezo-crystal is the only source of variation in the optical path, the maxima occur at the same voltage during every voltage swing and bright bands appear on the oscilloscope, called zebra-stripes, (see figure 4.13.).
Additional changes in the optical path, for instance caused by the vacuum arc, give rise to a shift of the bands, see figure 4.14. As the distance between two bands, corresponding with one fringe, is equivalent to half a wavelength of the

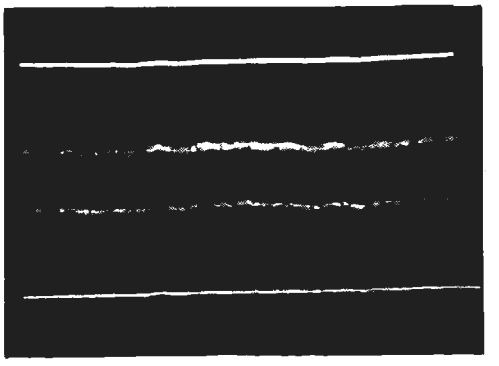

Figure 4.13 Result of a no-load operation obtained with the Zebra-stripe method.

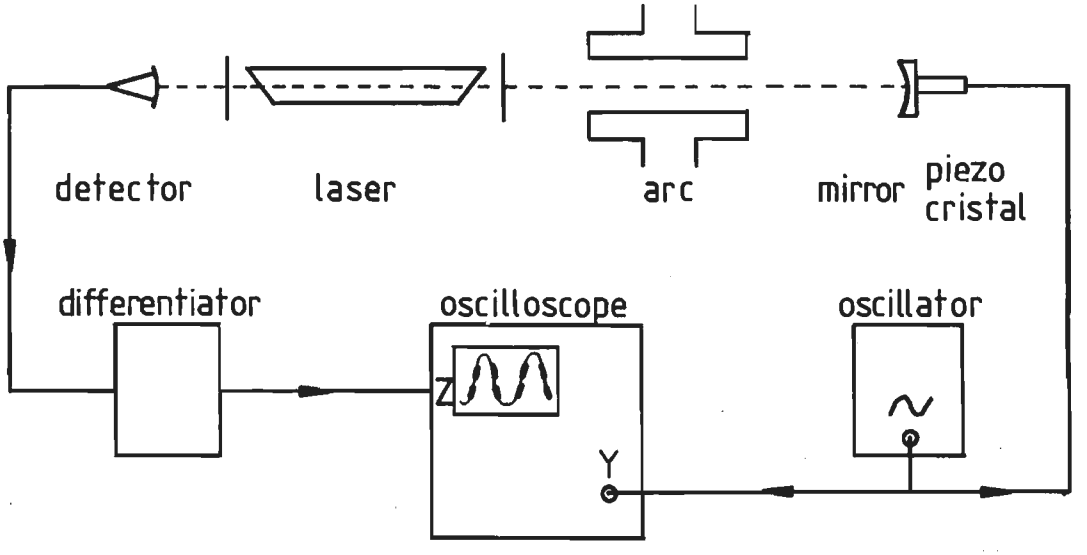

Figure 4.12 Schematic of the Zebra-stripe method.

laser a fraction of a fringe is easily determined from figure 4.14.
The background noise from mechanical vibrations limits the minimum detector sensivity to 0.1 fringe. The frequency of the piezo-electric driving voltage is limited by the first harmonic frequency of the piezo-crystal mirror spring-mass system: which is ± 3 kHz. A change of more than half a fringe during one period of the frequency of the crystal appears like a change of somewhat less than half a fringe in the other direction. This limits the maximum detector sensitivity to 600 fringes/second.

4.2.2.2 The infrared laser interferometer

Here also the Ashby-Jephcott laser interferometer was used. One expects that at longer laser wavelengths if the noise is mainly due to mechanical vibrations the signal to noise ratio would improve. But because of the large transmission losses for the infrared light at the entrance windows of the vacuum chamber and at the inside mirrors, the intensity of the reflected beam became too small to give a measurable interference signal in the laser output. Unlike the spectroscopic measurements where the copper mirror could be used to image the arc, the laser measurements suffered from the loss of light by scattering on the small droplets deposited on the copper mirror. Therefore, mirror M3 (figure 4.11.) had to be placed inside the vacuum chamber. This considerably increased the mechanical noise level, caused by the mechanical stresses of the discharge current exerted on the vacuum chamber, The swing of the piezo-crystal was not sufficient at the longer infrared laser wavelength, so the zebra-stripe detection method was not possible. Therefore, the classical way of detecting fringes was used.
(see figure 4.15.)

4.2.3. Results

The figures 4.14 and 4.15 show typical results obtained by both methods. The

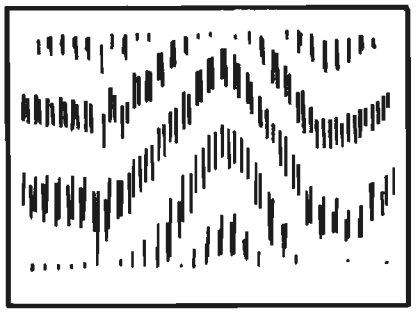

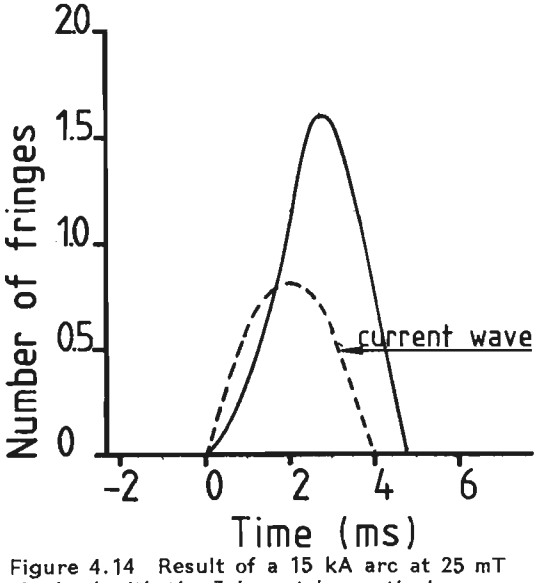

Figure 4.14 Result of a 15 kA arc at 25 mT
obtained with the Zebra-stripe method.
a: measurement result
b: counted fringes

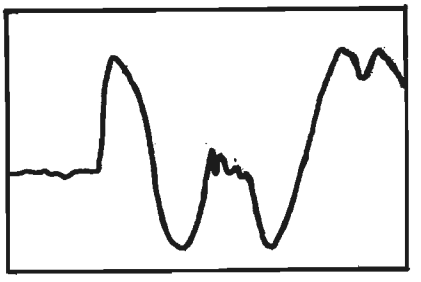

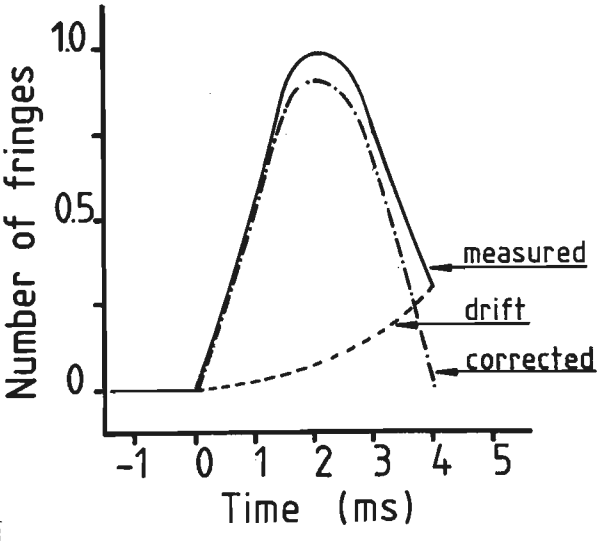

Figure 4.15 Result obtained with the infra-red laser interferometer.

experimentation time, which is half the period of the sinusoidal discharge current, and amounts to 4 msec is comparable to the time necessary for the shock-wave induced by the current to reach the mirrors. This causes an uncertainty of 10 % for the first 2 msec. in the infrared measurements and an even larger uncertainty thereafter. Figure 4.16 depicts the measured electron and neutral densities integrated along the line of sight as a function of the current at 50 mT.

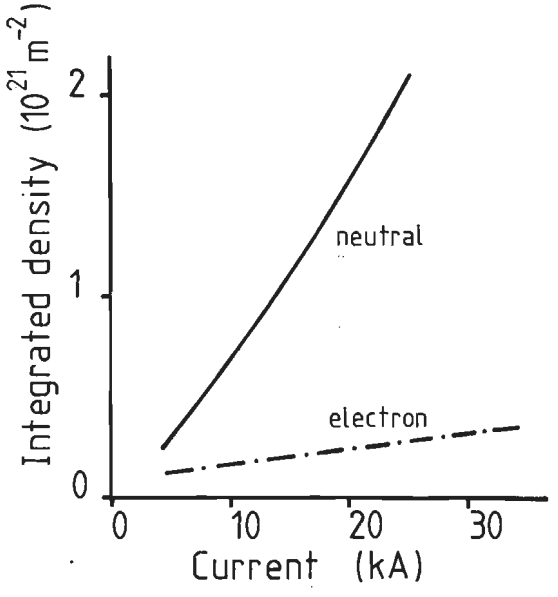

Figure 4.16 Line integrated densities of neutrals and electrons at 50 mT for various arc currents.

The spectroscopic measurements give only information about the region in which light is emitted and which is mainly confined to the electrode region. The extrapolation towards the walls of the spectroscopically determined ratio between neutral and electron density (see figure 4.10) suggest an increase of the neutral density as shown by curve 1 in figure 4.17. However, at the edge of the plasma the ion lines become very weak; this may lead to an overestimate of the neutral density there Still the neutral density may also have a considerable value in the long observation ports. This case is represented in figure

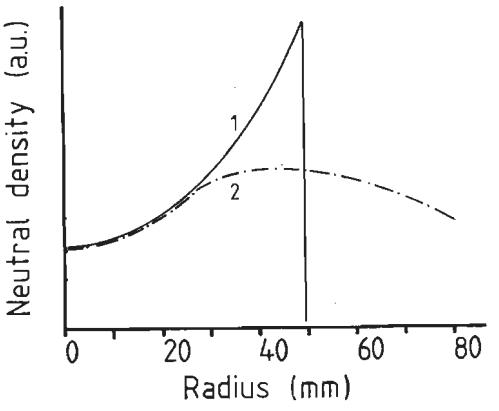

Figure 4.17 Various possible radial neutral density profiles (schematic) resulting in the same line integrated density.

4.17 by curve 2. With the diagnostic method the line integral of the neutral density is measured, which gives the absolute value of the neutral density.

Figure 4.18 shows the radial profile of the neutral density. Now also the ionization degree in the arc centre can be determined. This yields a value of approximately 80 %.

The red laser measurements show also a time lag between the discharge current and the signal. As the main contribution to this signal comes from the neutrals, the maximum neutral density is found to be delayed 1 msec. with respect to the maximum in the current, (see figure 4.14.b). This effect will be discussed in chapter 6.

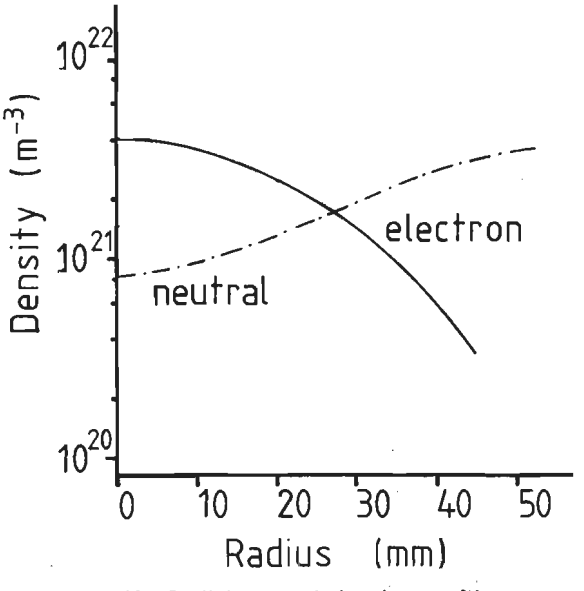

Figure 4.18 Radial neutral density profile at 10 kA, 50 mT (curve 2 of figure 4.17) and radial electron density profile.

4.3 DIAMAGNETIC LOOP MEASUREMENTS

4.3.1 Measurement principle.

A diamagnetic loop is a coil for measuring magnetic fields. The diamagnetic loops used enclose axial magnetic fields in order to measure the axial flux change produced by the plasma. Many plasmas have a negative magnetic susceptibility. If an external magnetic field is applied such a plasma produces a magnetic field that opposes the applied field. These plasmas are called diamagnetic and thus the name of the measurement method refers to such a situation.

However, the vacuum arc studied below is strongly paramagnetic: the arc strengthens the applied axial magnetic field. Nevertheless the diamagnetic loop will retain its name throughout this study.

The voltage induced in one loop is proportional to the change in flux enclosed by the loop, and can be written:

$$\varepsilon = -\frac{\partial \Phi}{\partial t} = -\frac{\partial}{\partial t}\int_{A_{dl}} B_z(r)\cdot 2\pi r\cdot dr \qquad (4.14)$$

in which A_{dl} is the total area of the diamagnetic loop. The flux enclosed by the loop is directly related to the axial magnetic field strength. The axial magnetic field strength B_z is the sum of the externally applied axial magnetic field, B^{ext}, and the magnetic field produced by the plasma. B_z^{plasma}.

$$B_z = B_z^{ext} + B_z^{plasma} \qquad (4.15)$$

The axial magnetic field produced by the plasma results from the azimuthal currents in the arc. These currents produce a flux Φ that can be picked up by the diamagnetic loop (Sch 74).

If the axis of the diamagnetic loop coïncides with the symmetry axis of the azimuthal current, the voltage obtained after integration by an R_iC_i network of the voltage induced in the loop is given by Kluber as (Klu 67):

$$e_d(t) = \frac{n}{R_iC_i}\cdot\Phi(R,Z,t) \qquad (4.16)$$

Where R is the radius of the loop and Z the axial position of this loop.

The presence of metallic parts near the arc cause the signal to be delayed with respect to the actual flux.
So the diamagnetic loop signal depends not only on the geometry of the loop and the dimensions of the arc but also on the geometry of metallic parts in the vacuum chamber and the time history of the flux:

Integration of the induced voltage in the n turns of the diamagnetic loop yields:

$$e_d(t) = \frac{n}{R_iC_i}\cdot\int_{-\infty}^{0} H(\tau)\cdot\Phi(R,Z,t-\tau)\,d\tau \qquad (4.17)$$

H(t) represents the transfer function of the metallic parts.
In the following first the experimental set up and the data handling will be described which were used to determine the radial dependence of the azimuthal current density. Thereafter the results obtained will be shown.

4.3.2 Experimental Setup

In order to minimize the time delay between the flux generated by the azimuthal current density and the diamagnetic signal, the diamagnetic loop was placed inside the anode, which was made of a thin copper disc (2 mm.), mounted on a hollow copper stem (diameter 54 mm, thick 2 mm) with a vertical slit to reduce the skin-current. The cathode was a butt copper contact as in all other experiments. The distance between the diamagnetic loop and the middle of the vacuum arc is 8 mm.
Thus a radial resolution of the flux is possible. So four diamagnetic loops of 5 windings each and with diameters of 15,30,45 and 56 mm were placed inside the anode. The axises of these loops coïncide with the symmetry axis of the electrode arrangement. (see figure 4.19). As this experiment does not provide information about the axial variation of the flux, the azimuthal current density can not be determined without an assumption on its axial dependence. For the sake of simplicity it is supposed that the azimuthal current density inside the arc is independent of axial position. As it is hard to calculate the shielding effect by the

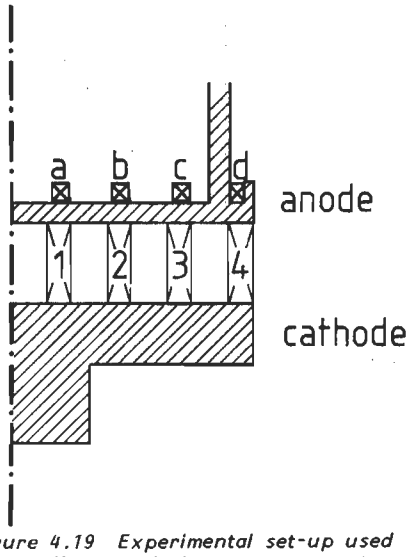

Figure 4.19 Experimental set-up used in the diamagnetic loop measurements. Coils a, b, c and d are the diamagnetic loops. Coils 1, 2, 3 and 4 are the test coils used to calibrate the set up.

electrodes in the evaluation of equation 4.13, the coupling and the phase lag between the azimuthal current and the signal of the loops has been determined experimentally. In a test stand four axial magnetic field generating coils of various diameters simulated the azimuthal currents inside the arc, (see figure 4.19).
The signal obtained from a diamagnetic loop depends on the current flowing in each of the test coils. By supplying a sinusoidal current through each of the test coils the complex Fourier transforms of the diamagnetic loop signals could be measured.

For instance the complex Fourier coëfficient of the diamagnetic loop signal a at frequency is:

$$E_a^c(\omega) = M_{a1}(\omega)\cdot I_1^c(\omega) + M_{a2}(\omega)\cdot I_2^c(\omega) + M_{a3}(\omega)\cdot I_3^c(\omega) + M_{a4}(\omega)\cdot I_4^c(\omega) \qquad 4.18$$

where I^c_n is the complex Fourier coëfficient of the current through test coil n and M_{an} is the complex coupling constant between test coil n and diamagnetic loop a.
The complex Fourier coëfficients of the diamagnetic loop signals can be written in vector notation for each frequency component as:

$$\underline{E}^c(\omega) = \underline{\underline{M}}(\omega)\cdot\underline{I}^c(\omega) \qquad (4.19)$$

In the test stand the matrices $\underline{\underline{M}}(\omega)$ can be determined for various frequencies.

Regarding the applicability of these tests to the actual plasma situation two questions can be raised. First, in the test setup a discrete current flows in a limited region, the coil, whereas in the arc the azimuthal current will be a distributed current. In order to get around this problem it is assumed that the azimuthal current density is constant in axial direction along the length, l, of the vacuum arc and that the azimuthal current flowing in the arc between the radius of test coil i, R_i, and test coil i-1, R_{i-1}, may be represented by a current I_i flowing in a hypothetical test coil with radius R_i:

$$I_i = \int_{R_{i-1}}^{R_i} j_\theta(r)\cdot l\cdot dr \qquad (4.20)$$

In figure 4.20 the simplification used to evaluate the results of the measurements is illustrated.

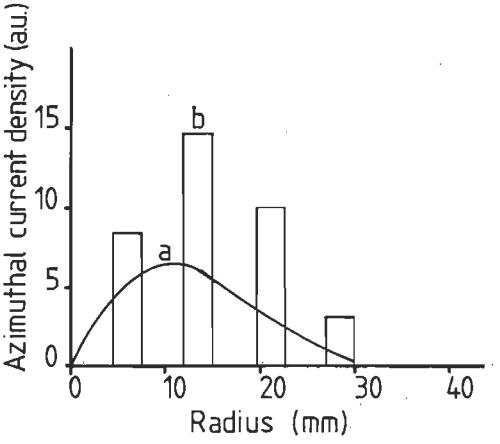

Figure 4.20 Radial distribution of the azimuthal current density in the vacuum arc. a.: probably the actual distribution b.: simplified by the geometry of the test coils

Secondly, in the time dependent vacuum arc the actual diamagnetic loop signal contains an infinite number of frequencies with for each frequency a different complex coupling matrix. In the actual computation the diamagnetic loop signal was converted by Fourier transformation to a finite number of frequency dependent complex Fourier coefficients. For each of these frequencies equation 4.19 was solved yielding the complex Fourier coefficients of the four currents.
Thereafter the time dependend azimuthal current density was obtained by the inverse Fourier transformation.

As the external magnetic field was

constant, the signal caused by the associated flux could be filtered off by a low frequency cut-off filter.

The azimuthal magnetic field, which originates from the main current, generates an extra flux Φ_I in the loop given by:

$$\Phi_I = \mu_o s I \cdot tg(\alpha/2) \qquad (4.21)$$

,if the loop axis is displaced by the distance s (the closest approach of both axes) and inclined by the angle α with respect to the centre of the discharge (Uo 64, Sch 74) This additional flux interferes with the flux originating from the azimuthal plasma current.
The total flux enclosed by the loop is:

$$\Phi_{total} = C_1 \cdot j_\theta + C_2 \cdot I \qquad (4.22)$$

where C_1 and C_2 are geometrical constants. The azimuthal plasma current is dependent on the direction of the applied axial magnetic field. So both components can be separated by measuring the diamagnetic loop signal with positive and negative magnetic field.

4.3.3 Results

The signal obtained from one diamagnetic loop is shown in figure 4.21 for a positive and a negative magnetic field. An error of approximately 5 % is introduced by the drift of the integrator.

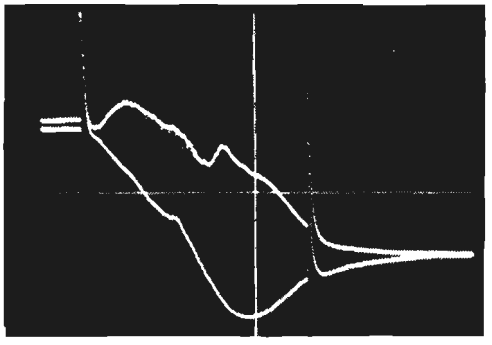

Figure 4.21 Signal obtained from one diamagnetic loop with positive (upper beam and negative magnetic field (lower beam).

Sharp peaks are visible, which occur at the triggering of the discharge and at current interruption. Figure 4.22 shows the measured fluxes of the four diamagnetic loops. Each signal is the difference from two measurements, one with positive and one with negative axial

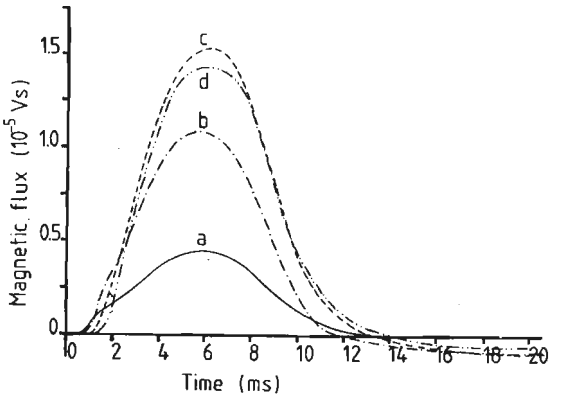

Figure 4.22 Flux enclosed by the four diamagnetic loops.
Arc parameters : sinusoidal current of 10 kA peak and an axial magnetic field of 20 mT.

magnetic field like the example in figure 4.21.
The flux enclosed by diamagnetic loop d is smaller than the flux enclosed by loop c. This indicates that the main azimuthal current flows in a region fairly close to the centre of the arc.
Also the time delay due to the metallic parts is obvious; not only the flux is delayed with respect to the current, but there is still a substantial flux near current zero.

Equation 4.15 has been solved by a least square method assuming that the azimuthal current density divided by the radius has a Gaussian profile.

$$j_\theta / r = C \cdot \exp\{-(r/r_o)^2\} \qquad (4.23)$$

The limited number of equations (four) allows for a reasonably accurate determination of two parameters: C and r_o. The results are shown in figure 4.23, where the peak azimuthal current density and the characteristic radius are represented for a 10 kA arc for various axial magnetic field strengths.
With increasing axial magnetic field the radius of the azimuthal current increases, but the peak value decreases significantly. Figure 4.24 depicts the time behaviour of the azimuthal current on several radial positions of the arc at 16 mT. These profiles are calculated with 10 Fourier coefficients giving a maximum frequency resolution of 500 Hz.

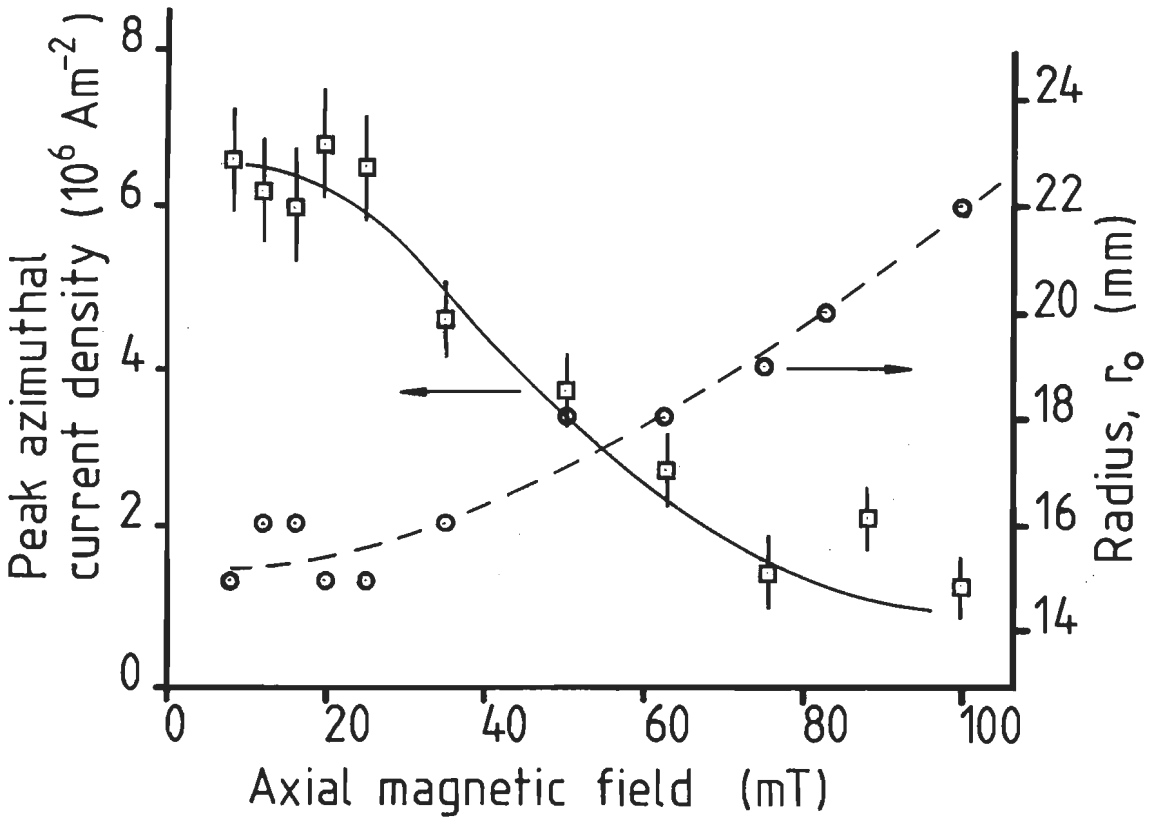

Figure 4.23 Azimuthal current density in a 10 kA arc as a function of the applied axial magnetic field.

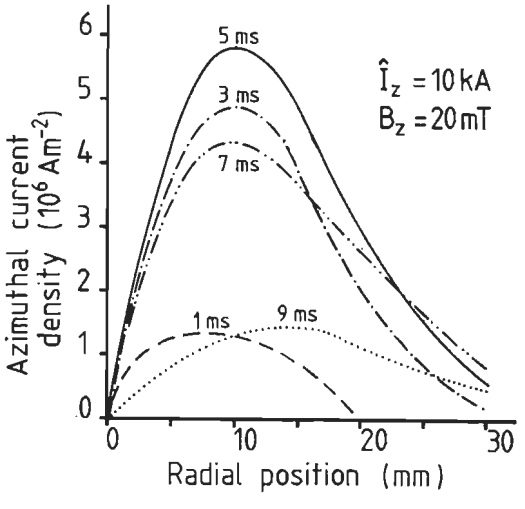

Figure 4.24 Time dependence of the azimuthal current density with a sinusoidal current of 10 kA peak at an axial magnetic field of 16 mT.

As a result of calibration inaccuracies especially in the determination of the phase shift, the calculated azimuthal current density attained non zero values at times of current zero. Except for large radii these errors are less than 10% of the azimuthal current density at current crest.

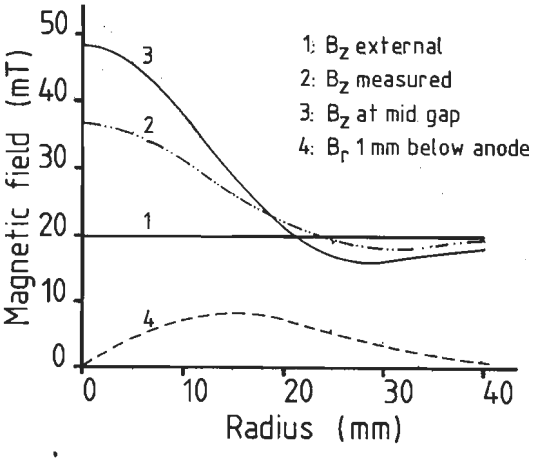

Figure 4.25 Magnetic field distribution in a 10 kA arc at an external magnetic field of 20 mT.
1.: Externally applied magnetic field
2.: Axial magnetic field on the position of the diamagnetic loops
With the assumption of an axially constant azimuthal current density:
3.: Axial magnetic field halfway between the electrodes
4.: Radial magnetic field 1 mm below the anode

With the here obtained azimuthal current density the magnetic field distribution in the arc can be calculated. In figure 4.25 the magnetic field at various positions is represented. Here the influence of the metallic parts is neglected. It is clear that the azimuthal current density generates a substantial additional axial magnetic field.

From the experimental data represented in figure 4.24 the radial current density will be derived in chapter 6 with the aid of the theoretical analysis of the momentum balance equations given in chapter 5. These experimental data this will also be used in the discussion on the origin of the arc voltage.

4.4 The Fabry Perot interferometer

4.4.1. Measurement principle

When a photon emitting particle moves with velocity towards an observer, the photon wavelength will be observed to be shifted by:

If the particles have a Maxwellian velocity distribution, the intensity of the line can be written as:

$$I(\lambda)\cdot d\lambda = \frac{2\sqrt{\ln 2}}{\Delta\lambda_d}\cdot \exp\{-4\ln 2\cdot((\lambda-\lambda_o)/\Delta\lambda_d)^2 \qquad (4.24)$$

where the full half width $\Delta\lambda_d$ of this Gauss profile depends on the particle temperature. In the case of copper

$$\Delta\lambda_d = 9\cdot 10^{-8}\cdot \lambda_o\cdot\sqrt{T(K)} \qquad 4.25$$

Although Doppler broadening will prove to be the main effect in the present study, other broadening mechanismes are considered as well (Loc 68).

Stark broadening: This effect occurs when the light emitting particle is under the influence of electric fields from other charged particles. It gives a Lorentz line profile. Parameters to calculate this effect are not available. The effect is smaller when the upper and lower level of the optical transition lie lower in the energy scheme.

Isotope shift: In natural occuring copper the isotope ratio between Cu^{63} and Cu^{65} is approximately 3 : 1. So all copper lines will have an isotope satelite. (Ney 66, Elb 61)

Zeeman effect: Magnetic fields cause a splitting up of the atomic energy levels when quantum number $J > 0$.
This result in a splitting up of the spectral lines. The spatial dependence of the magnetic field strength in the vacuum arc causes an additional broadening of the spectral line.

Selfabsorption: If the plasma is not optically thin the central wavelength of the spectral line will be more strongly absorbed than the line wings causing a distorted profile and appearant broadening.

The broadening of the spectral lines of 10 pm is too small to be measurable with either the monochromator or the spectrograph (both described above).
A Fabry-Pérot interferometer was used, of which the operating principle is shown in figure 4.26.

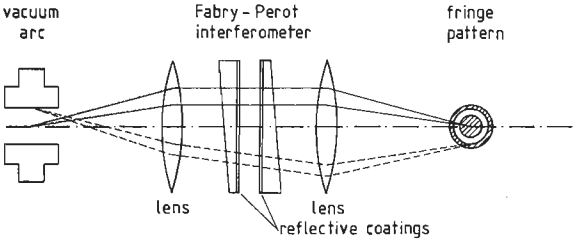

Figure 4.26 Principle of the Fabry-Perot interferometer.

The Fabry-Pérot consists of two parallel plates with highly reflective coatings, which produce an interference pattern like those presented in figure 4.27.
Preselection of the desired spectral range is achieved by the use of a monochromator. Figure 4.27a gives the interference pattern of a mercury line, 546 nm, emitted by a low pressure mercury discharge lamp. The photograph was taken with a Canon F1 camera and an image intensifier. In the photograph of figure 4.27b the interference pattern of the copper line 455.6 nm, emitted by the vacuum arc, is shown. The photographs display the following general features of Fabry-Pérot

patterns:

- further away from the centre of the interference rings, the rings lie closer together. Hence the best resolution is obtained in the centre.
- the broadening of the rings is a measure of the spectral line broadening, as is evident from the difference in width in the two photographs: the relatively cold mercury discharge shows smaller rings, than the relatively hot copper vacuum arc.

As the line width of the mercury lamp is small compared to the width of the apparatus profile, the width on the photograph is assumed to represent the apparatus profile.

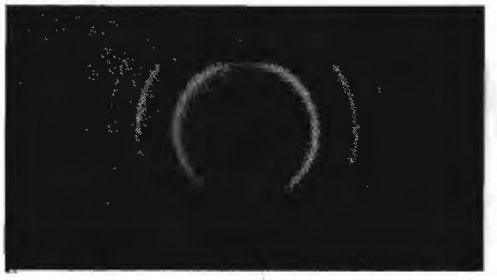

Figure 4.27a Interference pattern produced by the Fabry-Perot of a mercury line, 546 nm emitted by a low pressure discharge.

Figure 4.27b Interference pattern of a copper line 456 nm emitted by the vacuum arc at 10 kA.

By changing either the distance between the reflective glass plates (figure 4.26) or the dispersion of the refractive medium between the glass plates, a radial expansion of the interference rings is caused, and new interference ring are created in the centre of the pattern. Scanning of the line profile is achieved by changing the refractive index of the dispersive medium between the glass plates: pressure scanning.
A more extensive treatment is found in Lochte and Holtgreven (Loc 68).

4.4.2 Experimental equipment

A temperature stabilized Fabry-Pérot interferometer was used with a maximum reflectivity in the blue part of the spectrum (near 450 nm), where most of the visible copper ion lines are. In figure 4.28 the experimental arrangement is sketched.

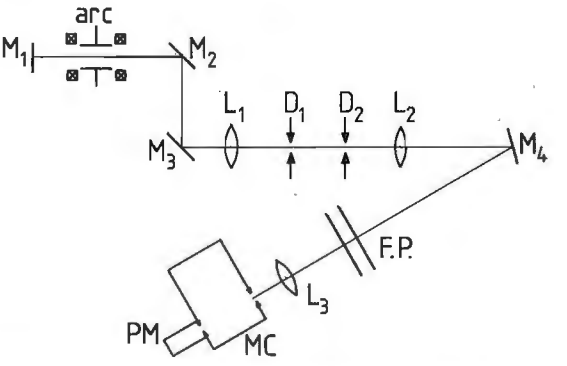

Figure 4.28 Experimental arrangement with the Fabry-Perot interferometer.

Selection of the spectral lines is carried out with a 0.25 m grating monochromater whose entrance slit is placed behind the Fabry-Pérot in the centre of the interference rings. The bandwidth of the monochromator is 0.9 nm.
At the wavelength of 455.6 nm the reflectivity of the mirrors was 97.2%. With a mirror spacing of 2 mm the free spectral range of the Fabry-Pérot is 52 pm, as the refractive index of the argon gas, which filled the Fabry-Pérot, is close to unity. At a wavelength of 455.6 nm the apparatus full width at half maximum is about 2.5 pm. As this apparatus profile is mainly caused by surface imperfections of the mirrors the apparatus profile has a Gaussian shape. The Lorentzian width is 1 pm which is small compared to the Gaussian width. The size of the pinhole (diameter .3 mm) placed in the entrance slit of the monochromator was too small to have a significant influence on the apparatus profile.
The light intensity was measured by a blue sensitive photomultiplier tube, RCA type IP 28. The output current of this photomultiplier was fed to a digitizing transient recorder, so that time resolution is possible. In order to obtain a sufficient accuracy in the light intensity, the signal is integrated during 1 msec by means of an RC-network.

As the arc duration is only 10 msec and the intensities of the spectral line reproduce within 10%, the spectral scanning of the line is obtained by changing the pressure of the argon gas inside the Fabry-Pérot interferometer between two successive discharges.
The optical system, allowed for selection of waist position and divergence by two diaphragms: one placed in the image plane and one in the focal plane of the first lens. With a spherical mirror it was possible to reflect the light emitted by the plasma back through the plasma.
This provides a means to measure the amount of selfabsorption of the spectral line (c.f. section 4.1).

4.4.3. Results

The measurements with the Fabry-Pérot interferometer were concentrated on the 455,6 nm CuII line
(upper level $4s^2{}^2D_2$ 10.99 eV : lower level $4p^3P_2$ 8.23 eV).
This line is chosen because

- it has a wavelength in the spectral range where the resolution of the Fabry-Pérot is maximum.
- it lies low in the CuII energy scheme, so that Stark broadening is expected to be small compared to the Doppler broadening.
- it has only two Zeeman-satellites. This resulted into a shift of the Zeeman satellites of ±15 pm per Tesla.

Figure 4.29 depicts the photomultiplier output voltage of the Fabry-Pérot versus wavelength. This figure thus represents the measured line profile at a current of 10 kA and an axial magnetic field of 100 mT. Each point gives the mean value of two measurements. The error bars indicate the shot to shot reproducibility. The drawn line is the best fit Gauss-profile obtained with a least square method. Also the apparatus profile of the Fabry-Pérot interferometer is shown. As the Doppler effect is not the only effect that influences the line profile, the various other broadening mechanisms, listed above, will be discussed quantitatively before deriving the ion temperature from the measured line profile.
The Stark contribution to the line profile is the largest in the line wings. In order to obtain the Stark contribution to the line profile, the broadening was measured at half the intensity of the line and at 10% intensity of the line. Using the tables of Lochte and Holtgreven an upper limit to the Lorentz half-width is found to be 20% of the Gauss half-width. As a result of the uncertainty in the determination of the actual intensity of the continuum radiation, the width of the spectral line at 10% of its peak intensity is rather inaccurate. Therefore the Lorentz half-width mentioned above has to be considered as a upper bound and not as an estimate. This upper limit of the Lorentz half-width leads to a 10% reduction in the actual Gauss half-width.

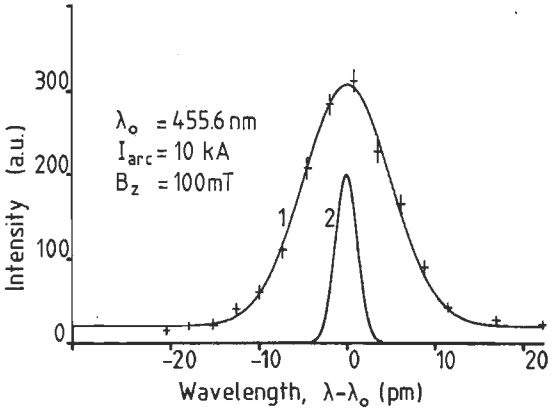

Figure 4.29 Intensity versus wavelength. Curve 1 represents the CuII line at 455.6 nm. The bars indicate the measurement accuracy and the drawn line is the best fit Gauss-curve. Curve 2 represents the apparatus profile.

In figure 4.29 also the apparatus profile is shown at the center wavelength. The half-width of the apparatus profile is to 2.5 pm. This results in a total finesse of the optical system of 21. So the width of the apparatus profile is very small compared to the width of the measured line profile. Deconvolution of the measured line profile with the apparatus profile yields thus a nearly identical real line profile.

Selfabsorption of the spectral line was measured by taking both the ratio between the intensity of the line center with and without the spherical mirror M1 (see figure 4.28) and the ratio between the

intensity of the continuum with and without the spherical mirror. From both ratios the selfabsorption is calculated to be negligible ($k_o l < 0,1$).

The Zeeman effect causes a line splitting. In cases where the magnetic field points in one direction this line splitting can be corrected for by polarization filters.
However, in the vacuum arc the axial magnetic field is comparable to the azimuthal magnetic field. The magnetic field vector in the middle of the arc points in the axial direction, but in the periphery of the arc the magnetic field vector has a strong azimuthal component.
So, when observing the arc side-on, the magnetic field vector rotates along the line of sight.
Therefore, in the present experiment it is impossible to separate the Zeeman satellites with polarization filters.
The Zeeman effect was corrected for by means of tables after the evaluation of the Gauss profile.

Isotope splitting of the spectral line at 455.6 mm studied here amounts to 2.5 pm, but as satellites do not have the same intensity, the influence of this splitting on the line profile is much less.
The effect of the splitting was also corrected for by means of tables.

The experimentally determined line profiles are corrected for the apparatus profile, the Zeeman effect and the isotope splitting. Because of the inaccuracy of the intensity measurements no determination of the Lorentz contribution to the line profile could be made.

With equation 4.25 the ion temperature is calculated from the line half-width under the additional assumption that the thermal velocity is sufficiently large compared to any systematic radial ion velocity.

In figure 4.30 the dependence of the ion temperature with respect to the axial magnetic field is represented. The measurements in absence of an axial magnetic field yield an ion temperature of 11eV independent of the current in the range of 2.8 kA to 8 kA.

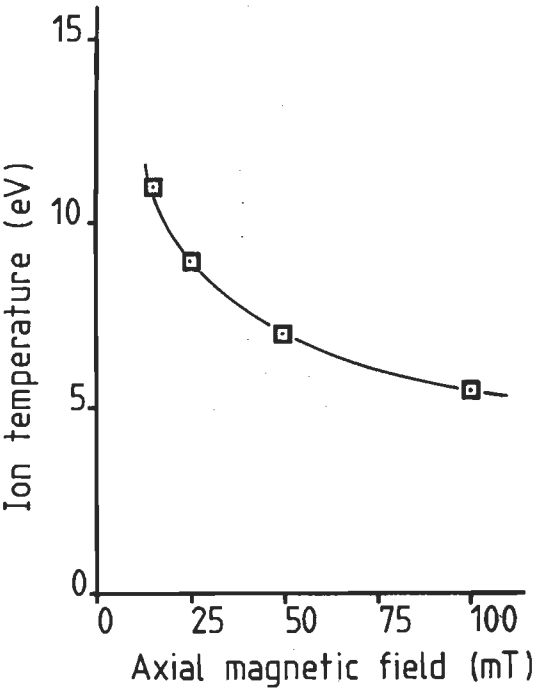

Figure 4.30 Ion temperature in a 10 kA arc for various axial magnetic field strengths.

In figure 4.31 the dependence of the ion temperature with respect to time for three arcing conditions is given; at 0 mT, 15 mT and 100 mT axial magnetic field strength. At low axial magnetic fields the ion temperature increases with current. In absence of this field this time dependent behaviour vanishes and the ion temperature becomes constant, 11eV within the time resolution of the experimental setup of 1 msec.

At an axial magnetic field of 25 mT the radial dependence of the ion temperature was determined. It was found that the ion temperature was independent of radius. The measurement revealed also that the center of the spectral line was shifted.
From a measurement of the position of the line center with positive and negative axial magnetic field the rotational velocity of the ions could be obtained. In figure 4.32 the observed rotational velocity of the ions is represented halfway between the electrodes. From this it is concluded that the interelectrode plasma rotates as a rigid body according to a left handed screw (anti clock wise) with regard to the axial

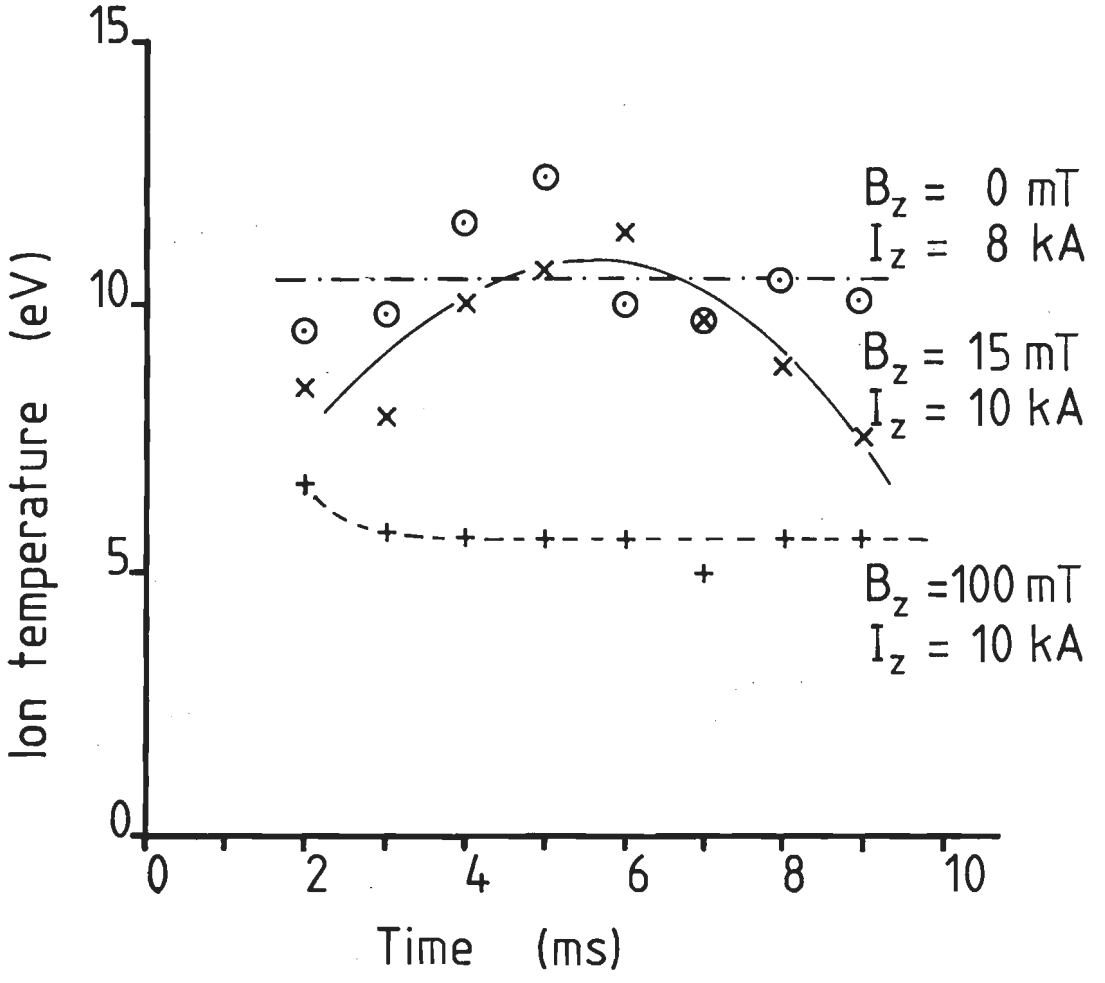

Figure 4.31 Ion temperature for various arc parameters as a function of time.

magnetic field. The rotational frequency amounts 3.3 kHz. This is nearly the same as the ion cyclotron frequency at 25 mT (3.7 kHz), taken only the externally applied axial magnetic field into account. The here observed rotation is the ion rotation in the plasma body as a whole. This confirms the validity of the diffuse plasma model used in this thesis.

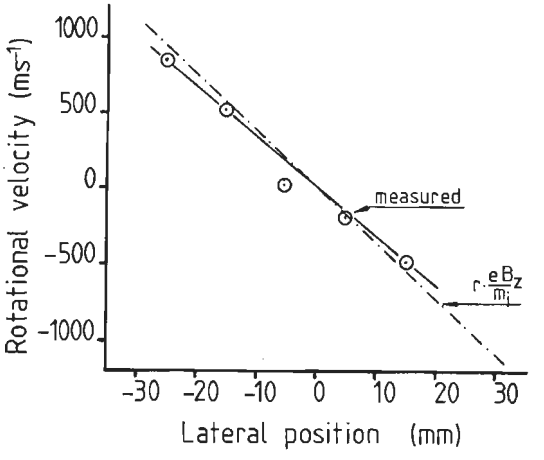

Figure 4.32 Ion rotational velocity at 10 kA, 25 mT as a function of radial position halfway between the electrodes.

5. THE PLASMA STATE IN THE VACUUM ARC

5.1 Introduction.

In kinetic theory the state of a plasma is specified for each particle component by a distribution function, which describes the density of these particles in phase-space at a certain time. The evolution of the distribution function with time is governed by the Boltzmann equation, which takes into account the forces exerted on the particles by external fields and collisions. As the mean free path of the particles in the vacuum arc is much shorter than the characteristic dimensions of the arc (cf. chapter 6), it is sufficient to describe the plasma in terms of average quantities, which can be obtained from the first three moments of the Boltzmann equation by integration over the velocity space. (Bra 67). One arrives after some substitutions at the following three balance equations, which hold for each particle component of the plasma: electrons, ions and neutrals.

Particle balance equation.

$$\frac{\partial n}{\partial t} + \nabla\cdot(n\underline{w}) = S \qquad 5.1$$

production rate
diffusion
particle sources

momentum balance equation

$$nm\{\frac{\partial}{\partial t}\underline{w} + (\underline{w}\cdot\nabla)\underline{w}\} = -\nabla p - \nabla\cdot\underline{\underline{\Pi}} + qn(\underline{E} + \underline{w}\times\underline{B}) - \underline{R} - \underline{M}^S \qquad 5.2$$

acceleration
inertia
pressure
viscosity
electric force
Lorentz force
friction
sources

energy balance equation

$$\frac{3}{2}\frac{\partial p}{\partial t} + \frac{3}{2}\underline{w}\cdot\nabla p + \frac{5}{2}p\nabla\cdot\underline{w} + \underline{\underline{\Pi}}:\nabla\underline{w} + \nabla\cdot\underline{q} = Q - L^S \qquad 5.3$$

heating rate
diffusion
convection
viscous heating
heat conduction
collisional heating
sources

In this thesis the energy balance equation is not dealt with in detail.

The symbols used in the above equations represent:

- n : particle density
- S : particle sources
- P : scalar pressure
- q : particle charge
- $\underline{B}$: magnetic field
- $\underline{w}$: average velocity
- m : particle mass
- : viscosity tensor
- $\underline{E}$: Electric field (macroscopic)
- $\underline{q}$: heat flow
- $\underline{R}$: momentum transfer by collisions between different particle species.
- Q : heat transfer by collisions between different particles species.
- $\underline{M}^S$: momentum loss associated with finite sources
- L^S: energy loss associated with finite sources

For the analysis of these equations it is necessary to model the vacuum arc, see figure 5.1.
The following regions are discerned in the high current vacuum arc:

- the cathode spot: which acts as the interface between the metal electrode and the arc.
- the luminous plasma ball in front of the cathode spot, which forms a transition region from the high pressure neutral vapour in the cathode spot to the relatively low density of ionized vapour in the cathode jet
- the cathode jet: expansion of the ionized gas from the plasma ball towards the interelectrode plasma.
- the interelectrode plasma: the interelectrode plasma is caused by intermixing of the individual cathode jets and ionization of the ambient plasma.
- the anode sheath: transition region between the plasma and the anode.

The characteristic dimensions of these

regions determine the accessibility of the regions for the diagnostic methods described in chapter 4. The measurements of the axial dependence of the relative fluctuation level outlined in chapter 2, see figure 2.16, show that in the first millimeter above the cathode the plasma ball with the cathode jet make up the image of the arc. (The very small cathode spot is not visible through the luminous plasma ball.)
The anode sheath will have typical dimension of some mean free paths, which in the high current vacuum arc will be of the order of 0.1 mm .
Approximately 90% of the space between the electrodes is filled with the interelectrode plasma.
The analysis of the balance equations is focussed on this region in particular.

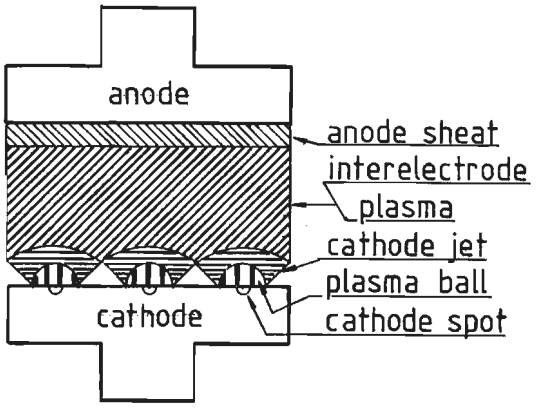

Figure 5.1 Schematic representation of vacuum arc showing the various regions

5.2 The particle balance.

The charged particle balance for a stationary plasma reads

$$\nabla \cdot n\underline{w} = \text{production} - \text{recombination} \quad (5.4)$$

For the diffuse vacuum arc the cathode is the ultimate source of material. In the cathode spot electrode material evaporates and is ionized in the plasma ball just above the cathode, but also in the interelectrode plasma is ionization and recombination.
The importance of the various terms in equation 5.4 will be estimated by a comparison of their characteristic time scales.

5.2.1 Diffusion

If in a plasma a density gradient arises a particle flux will tend to smooth out the non uniformity. In the first approximation the following relation exists:
between the cause, ∇n and the effect $n\underline{w}$

$$n\underline{w} = - D \nabla n \quad (5.5)$$

where D is the diffusion coëfficient (Miy 80).
If the diffusion is classical,

$$D = \frac{1}{\Omega_e \tau_e} \cdot \frac{kT}{eB} \quad (5.6)$$

for the charged particles. This estimate is appropriate only in a limited range for the electron Hall parameter:
$1 < \Omega_e \tau_e < 50$ (Pot 78). Below $\Omega_e \tau_e = 1$ the diffusion is also influenced by ion-neutral collisions. Above $\Omega_e \tau_e \sim 30$ anomalous diffusion sets in and Bohm's estimate would be more appropriate (Sch 83).
The characteristic time of diffusion can be defined as:

$$\tau_{diffusion} = \frac{\Lambda^2}{D} \quad (5.7)$$

where Λ is a characteristic scale for density gradients. With the experimental data of chapter 4 a characteristic time of diffusion is obtained of approximately 3.10^{-5} seconds. Davis observed in a 100A copper arc in vacuum ion velocities of around 14.000 m/s which results in very short electrode gap transit times (Dav 69). From this it may be concluded that in the low current vacuum arc diffusion is not a relevant phenomenon.
In the high current vacuum arc ion temperature measurements indicate a thermalization of this ion flow to a temperature of less than 11 eV. (cf. chapter 4.4). Kimblin measured that 8% of the current is carried by the ions (Kim 73). Then from the measured ion density an axial drift velocity of around 500 m/s towards the anode can be deduced. The electrode gap transit time is

thus of the same order as the diffusion time in the high current vacuum arc (2.10^{-5} seconds).

5.2.2 Production

In a singly ionized plasma the production is only by ionization. The rate coëfficient for ionization of copper is estimated to be between 10^{-14} and 10^{-13} m^3/s depending on the electron temperature (Miy 80, Zel 66). This results in ionization times of the order of 10^{-6}s at the neutral densities in the interelectrode plasma. This rapid ionization process causes a depletion of neutrals in the interelectrode plasma.

5.2.3 Recombination:

Recombination may be either radiative or collisional dielectronic recombination. At the electron densities and electron temperatures observed in a vacuum arc only the first is of importance. The rate coëfficient for radiative recombination to level n of a hydrogenic ion with charge Z-1 can be written as (Sea 59):

$$\alpha_n = 5.2\ 10^{-20}\ Z\, x_n^{3/2} \exp(x_n) E_1(x_n) \quad m^3/s \qquad (5.8)$$

Where $E_1(x) = \int_x^\infty \frac{e^{-t}}{t}\, dt$ is the first exponential integral and x the ratio between the ionization energy of level n and the electron thermal energy. This gives a rate coëfficient for recombination of the order of 10^{-18} $m^{+3}s^{-1}$ at the electron temperature prevailing in the arc. Thus the recombination time in the arc, ±0.2 msec, is so long that it does not influence the particle balance of the ionized particles.

In view of the strong dependence on the electron temperature, recombination can become important close to the anode.

In a 10 kA vacuum arc the influx of ions towards the anode amounts to 2.10^{24} $m^{-2}s^{-1}$. These ions recombine near or at the anode surface causing an increase of the neutral density there.

The above described ionization and recombination processes cause large neutral density gradients that result in a continous flow of neutrals towards the middle of the electrode gap securing a significant source of ionization in this region.

5.3 The momentum balance.

The current through a vacuum switch is determined by the characteristics of the electrical circuit.

The width of the current channel and the arcing voltage across the switch depend on the plasma properties at the actual current value. The heat dissipated during the arcing period, which is proportional to the electric field and the current, determines to a large extent the size of the interrupter. Therefore, the main interest lies in establishing the current flow lines and the electric field from the momentum balance.

Before the analysis of the momentum balance equations 5.2 some of the results obtained in chapter 4 with regard to the basic plasma quantities will be used to simplify these equations. On this basis it will be assumed that:

- the plasma is stationary. This is justified by the fact that the diffusion time is much shorter than the duration of the current pulse.
- the plasma is rotationally symmetric. This condition is fulfilled when the vacuum arc is in the diffuse arcing regime.
  As the cathode spots are distributed across the whole cathode and with these sources of metal vapour, the radial extention of the arc is related to the cathode size.
- the plasma is singly ionized (cf. chapter 6.4) and that only one type of ion is present; charge neutrality requires

  $$n = n_i = n_e$$

- an axial and an azimuthal magnetic field are present. The diamagnetic loop measurements have shown that the arc produces an axial magnetic field of appreciable strength in addition to the externally applied axial magnetic field. As a result of the finite length of the arc also a radial magnetic field is produced. This radial magnetic field is

strongly dependent on the radial and axial position.

When the axial magnetic field points towards the anode, this radial magnetic field points inward close to the cathode and points outward close to the anode. However, figure 4.23 shows that the strength of this radial magnetic field remains small compared to the strength of the axial magnetic field and therefore this radial field will be omitted in the calculations below.

- the electron Hall parameter, which is the ratio between the electron gyration frequency and the electron collision frequency is close to 1.

$$\Omega_e \tau_e \sim 1$$

If the ion temperature does not differ too much from the electron temperature, an automatic consequence is that the ion Hall parameter is much smaller than 1.

- the dimensions of the plasma are much larger than the mean free paths of the particles, as is confirmed by the measurements of chapter 4 and will be discussed in chapter 6.

$$\lambda_e \simeq \lambda_i \ll \Lambda$$

- the ion systematic velocities may approach, but are smaller than the ion thermal velocity.

In a stationary plasma the ion velocity perpendicular to the magnetic field, $\underline{w}_\perp^i$, is given by

$$\underline{w}_\perp^i = \left(\underline{E}\times\underline{B} - \frac{1}{n_e} \nabla p_i \times \underline{B} - n\underline{j}\times\underline{B} \right)/B^2 \qquad (5.9)$$

Magnetohydrodynamic ordening allows that only the $\underline{E}\times\underline{B}/B^2$ velocity approaches the ion thermal velocity.

Therefore large systematic ion velocities may not be excluded. However, measurements indicate that the axial and azimuthal ion velocity remain small compared to the thermal velocity in the inter electrode plasma of the diffuse vacuum arc.

$$w_z^i , w_\theta^i \ll v_{th}^i$$

Estimates of the current density yield values of the systematic electron velocity small compared to the electron thermal velocity. As a consequence electron inertia electron viscosity and electron-neutral friction may be neglected, while ion inertia, ion viscosity and ion-neutral friction may not be neglected at first hand (Sch 83). It is interesting to note, that this ordering differs from the usual one for elongated arcs in one important aspect. Here the radial ion velocity may approach the ion thermal velocity. In elongated arcs the azimuthal ion velocity w_θ^i approaches the ion thermal velocity (Tim 81).

- the momentum loss associated with finite sources is:

$$\underline{M}^{Si} = nm_i(\underline{w}^i - \underline{w}^o)\nu_{ion} \; ; \; \underline{M}^{Se} = nm_e(\underline{w}^e - \underline{w}^o)\nu_{ion} \qquad 5.10$$

where ion refers to the ionization frequency.

In the present study of the vacuum arc plasma the ionization time is much greater than electron-ion collision time

$$\tau_{ion} = 1/\nu_{ion} \gg \tau_{ei}$$

Hence the source contribution $\underline{M}^{se}$ can be neglected with respect to $\underline{R}^{ie}$

- also electron neutral friction is neglected as the cross section for electron neutral collisions is small compared to the cross section for electron ion collisions
- the resemblance of the ion-neutral friction force with the force exerted by finite sources makes it possible to simplify the equations.

$$\underline{R}^{io} + \underline{M}^{Si} = nm_i(\underline{w}^i - \underline{w}^o)\nu^{io} + nm_i(\underline{w}^i - \underline{w}^o)\nu^{ion} = nm_i(\underline{w}^i - \underline{w}^o)\nu^{io'} \qquad 5.11$$

where ν^{io} is the ion neutral collision frequency and $\nu^{io'}$ the effective collision frequency corrected for ionization.

- the experiments have shown that both ion and electron temperatures are constant in the interelectrode plasma (cf. chapter 4.1 and 4.4). Therefore the balance equation are simplified by use of

$$\frac{\delta T}{T} \ll \frac{\delta p}{p}$$

With the above assumptions the momentum balance equations read :

$$nm_i(\underline{w}^i \cdot \nabla)\underline{w}^i + \nabla p_i = en(\underline{E} + \underline{w}^i \times \underline{B}) - \underline{R}^{ie} - \underline{R}^{io} \qquad 5.12$$

$$\nabla p_e = -en(\underline{E} + \underline{w}^e \times \underline{B}) + \underline{R}^{ie} \qquad 5.13$$

In appendix A estimates of the various terms of the six components of the momentum balance equation are given in a dimensionless analysis.
It is also shown that viscosity may be neglected in the ion-momentum balance. Inertia is retained in the radial component of the ion momentum balance, as a priori not can be stated, that the radial ion velocity is small compared to the thermal velocity.
However, a numerical evaluation of the radial pressure balance at a current of 10 kA and a magnetic field of 25 mT shows, that due to the dominance of ion-neutral friction the radial ion velocity is also small compared to the ion thermal velocity. So, all systematic ion velocities turn out to be small compared to the ion thermal velocity and are small compared to the systematic electron velocities. The current is thus carried primarily by the electrons:

$$\underline{j} = -ne\ \underline{w}^{e} \qquad 5.14$$

With these considerations the above momentum equations can be modified to:

$$nm_i(\underline{w}^i\cdot\nabla)\underline{w}^i + \nabla(p^e+p^i) = \underline{j}\times\underline{B} - \underline{R}^{io} \qquad 5.15$$

(Navier-Stokes, i.e. the sum of the ion and electron momentum balance), and into:

$$\nabla p^e = -en\underline{E} + \underline{j}\times\underline{B} + enn\underline{j} \qquad 5.16$$

(the modified electron momentum balance).

The ion neutral friction couples Navier-Stokes equation to the neutral momentum balance. If neutral inertia and neutral viscosity are small compared to ion neutral friction, then ion neutral friction may be replaced by the neutral pressure gradient.

$$\nabla p^o = \underline{R}^{io} \qquad 5.17$$

As in this work the neutral pressure is not measured, hete the formulation with the friction term will be chosen.

The above introduced assumptions do not limit the applicability of the thus obtained momentum balance equations solely to the diffuse vacuum arc. In the plasma ball (see figure 4.1) the density of ions, neutrals and electrons is high enough to secure that the mean free paths of these particles is smaller than the characteristic dimensions of the plasma ball.
In this region the assumptions about a singly ionized plasma and about the electron Hall parameter do not necessarily hold. So with appropriate corrections the magnetohydrodynamic description can be extended towards the cathode spot.

5.3.1. The azimuthal balances

The azimuthal momentum balance of the electrons yields a relation between the radial current density and the azimuthal current density:

$$enn j_\theta = j_r B_\theta \qquad 5.18$$

or

$$j_\theta = \Omega_e \tau_e j_r \qquad 5.19$$

The equation 5.18 will be a keystone in the discussion of chapter 6, as it allows for the determination of the radial current density from the diamagnetic loop measurements. (cf chapter 4.3).
Knowledge about the radial current density enables the determination of the current flow lines with Kirchhoffs law: $\nabla\cdot\underline{j} = 0$
The azimuthal component of Navier-Stokes law yields

$$j_r B_z = nm_i(w_\theta^i - w_\theta^o)\nu^{io'} \qquad 5.20$$

Equation 5.20 can be used to obtain an estimate about the azimuthal ion velocity.

5.3.2. The axial pressure balance

Another expression for the radial current density can be found from the axial component of Navier-Stokes:

$$\frac{\partial}{\partial z}(p^e+p^i) = j_r B_\theta - nm_i(w_z^i - w_z^o)\nu^{io'} \qquad 5.21$$

Near the axis of the arc both the radial

current density and the azimuthal magnetic field vanish because of symmetry reasons. This means that near the axis the axial pressure drop is balanced by ion neutral friction, which limits the axial drift velocity of the ions. Thus an estimate for the axial ion drift velocity can be obtained:

$$w_z^i(r=0) = \frac{1}{nm_i \nu^{io'}} \frac{\partial}{\partial z}(p_e + p_i) \qquad 5.22$$

This balance is experimentally verified in hollow cathode arcs (Haa 82), which suggests, that it may be a more general characteristic of magnitized arcs with particle sources at the cathode side.
Off axis, the Lorentz contribution may be important in high current vacuum arcs and the axial velocity difference between neutrals and ions will accordingly be changed.
If $j_r B_\theta$ is positive the axial velocity difference will decrease with increasing radius.

5.3.3. The axial electric field

The axial momentum balance of the electrons yields an expression for the axial electric field.

$$enE_z = -\frac{\partial p^e}{\partial z} + j_r B_\theta + en\eta j_z \qquad 5.23$$

Part of the electric field is needed to support the current in the resistive plasma.

$$E_z^{Ohmic} = \eta j_z \qquad 5.24$$

The non Ohmic part of the electric field

$$E_z' = E_z - E_z^{Ohmic} \qquad 5.25$$

is then

$$E_z' = \frac{1}{ne}\left(-\frac{\partial p^e}{\partial z} + j_r B_\theta\right) \qquad 5.26$$

With the axial component of Navier Stokes equation 5.21 and equation 5.17 this can be written as

$$E_z' = \frac{1}{ne}\frac{\partial}{\partial z}(p^i + p^o) \qquad 5.27$$

Equations 5.26 and 5.27 are identical.
In chapter 6 the additional electric field E_z' will be calculated with equation 5.26.

5.3.4. The radial pressure balance

The radial component of Navier-Stokes equation is

$$\frac{\partial}{\partial r}(p^e + p^i) = j_\theta B_z - j_z B_\theta - nm_i(w_r^i - w_r^o)\nu^{io'} - nm_i w_r^i \frac{\partial}{\partial r} w_r^i \qquad 5.28$$

In the absence of an axial magnetic field the particles are kept together by the Pinch force $j_z B_o$ and by the ion neutral friction force and ion inertia.
A numerical evaluation of the above equation shows that the pinch force is not sufficient to explain the pressure build up. Mathematically, this means that the azimuthal beta, β_θ , defined as: the ratio of kinetic pressure and the pinch force, is larger than 1. For the high current vacuum arc typical values of 2 are obtained.
In an axial magnetic field positive azimuthal currents counteract the pinch force thereby decreasing the pressure gradient and thus the maximum attainable pressure.

In chapter 6 it will be shown that at 25mT the Lorentz forces exerted by the azimuthal current density and by the axial current density nearly cancel each other.
The current flows approximately "force free" (Lun 50) and hence the radial pressure drop must be balanced by inertia and ion neutral friction.
This yields thus an estimate of the radial ion velocity analogous to equation 5.22 and to equation 5.20.
Therefore one can state that as a consequence of the dominance of ion-neutral friction in Navier-Stokes law the differential ion neutral velocity, $\underline{w}^i - \underline{w}^o$,can be determined from the law of Navier-Stokes.

5.4 Some remarks

In the preceding chapter the diagnostic tools were described, that were used to measure some of the plasma quantities used in the above equations. In the general discussion of chapter 6 the implications of the above equations on the arcing behaviour will be investigated.

6 Discussion

In this chapter the results of the measurements described in chapter 4 with regard to the main plasma parameters, such as electron temperature, ion temperature, electron density, effective charge and neutral density are compared with findings reported in literature. Also their interplay on the equations derived from the momentum balance will be discussed. The discussion will be focussed on the pressure balance, the current density and the arc voltage. The pressure balance has a decisive influence on the current distribution and the potential distribution. Finally the formation of an anode spot is discussed on basis of the results reported here.

6.1 Electron temperature

The spectroscopic measurements yield a constant electron temperature of approximately 2.7eV. The electron temperature has been determined according to two methods, of which the applicability depends on the position in the arc. Near the cathode the electron density is so large that the upper excited state levels of neutral copper can be supposed to be in Saha-equilibrium with the continuum. Apparently near the cathode these levels are in PLTE. Then the Boltzmann-plot method is applicable and the distribution temperature equals the electron temperature.

Away from the cathode the distribution temperature is not equal to the electron temperature. Van der Mullen has shown that in absence of PLTE the excitation population for complicated atomic systems can be characterized by a simple power law, the CES phase (see figure 6.1). (Mul 81, Fuj 79)This has been confirmed in the present work for the copper neutral and copper ion system. The ion excited state density is then coupled to the ion ground state density by the Boltzmann factor, exp (-E/kT), multiplied by a collisional radiative (CR) constant, which is independent of electron temperature and density. When the CR constant and the elctron density are known, the electron temperature can be obtained from the excited state density.

In the literature various measurements of the electron temperature performed on a vacuum arc are reported. Most are based on the Boltzmann-plot method as described in section 4.1.

Morimiya e.a. report about the determination of the electron temperature in a high current arc with an axial magnetic field (typical valus 20 kA and 150 mT) from the ratio of two copper ion lines (the 254.4 nm and the 248.9 nm) under the assumption of partial local thermal equilibrium PLTE (Mor 73). They find electron temperatures of around 18000K or 1.6 eV. Kaneda determined the electron temperature from the ratio of two copper neutral lines (the 550.5 nm and the 555.5 nm) again under the assumption of PLTE at similar conditions and found an electron temperature of 7000 K or 0,6eV (Kan 81). As both the measurements reported above and

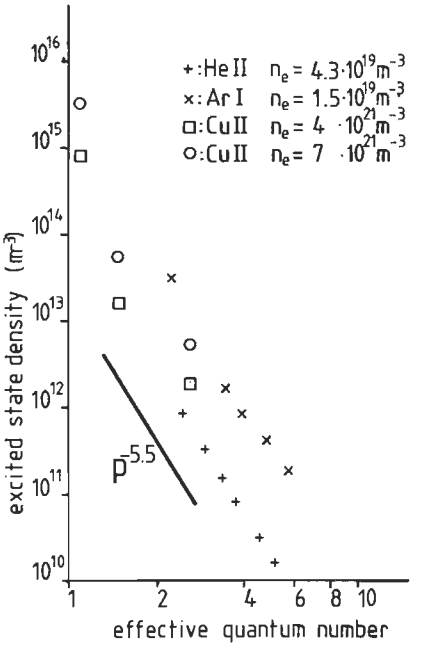

Figure 6.1 The excited state density for various atomic systems against the effective quantum number p.

the measurements described in chapter 4.1 are performed on a high current vacuum arc in an axial magnetic field, the results may be compared. The large differences between the electron temperature reported of in this thesis and obtained by Morimiya and Kaneda suggest, that the elctron temperature is not equal to the distribution temperatures.
The distribution temperature determined from the excited state densities in chapter 4 yield similar values as the temperatures given by Morimiya and Kaneda. Hence they erroneously identified this temperature as the electron temperature.

As the excited state densities in the CES-phase scale with $p^{-5.5}$, in which p is the principal quantum number (cf chapter 4.1), the closer two levels lie to the next ionisation stage, the steeper the line connecting the two levels in a Boltzmann plot and the lower the thus derived distribution temperature. Therefore the distribution temperature obtained from the copper neutral system is lower than the distribution temperature obtained from the copper ion system, and none of both distribution temperatures is equal to the electron temperature.

Boxman and Goldsmith performed extensive spectroscopic measurements on an aluminum arc burning on 25mm diameter electrodes spaced 4mm at a current of 2,8 kA peak without an axial magnetic field. (Box 80, Gol 80). From their findings distribution temperatures comparable to those in a copper vacuum arc can be derived. They used a time dependent collisional radiative model to explain the observed excited state densities with the electron temperature as a free parameter.
The principal assumption they made, is that the observed axial dependence of the excited state density in the laboratory frame is in fact the time dependent rate equation acting on the excited states in the frame of reference of the moving plasma.

So they state that:

$$\frac{\partial n}{\partial x} = \frac{1}{v}\frac{\partial n}{\partial t} \qquad (6.1)$$

The velocity of the moving plasma plays an essential role in their CR-model. They base the ion velocity on measurements of Davis and Miller, $1.5\ 10^4$ m/s (Dav 69). In section 6.2 the drift velocity of the ions will be discussed and it will be shown that the value found in low current vacuum arcs is improbable in the high current arc. Therefore the electron temperature deduced from the CR-model for aluminum (lying between 3 and 6 eV) cannot be compared with the value obtained in this study.

Webster e.a. performed measurements with an electrostatic probe in a vacuum arc between 75 mm diameter copper electrodes with 15 mm clearance (Web 76). They found for fixed current the electron temperature to depend on the effective electrode diameter. For instance an electron temperature of 3.5 eV at a current of 4.7 kA and an effective electrode diameter of 60 mm. This differs 30% from the result obtained in this study. In accordance though is the spatial dependence of the results. They also found the electron temperature to be constant within the arcing region between the electrodes. Outside this region the temperature falls off sharply.

The temperature drop could not be detected in the present spectroscopic study because in these outer arcing regions the emissivity is very low and therefore does not permit determination of the electron temperature.

In the above discussion it is shown that for a large range of arcing parameters the excited copper states are in the CES phase except for the arc region closest to the cathode where some upper levels are in PLTE, i.e. Saha equilibrium with the next ionization stage. The electron temperature is found to be independent of position and current, and is approximately 2.7 eV.

6.2 Ion temperature

In the presence of an axial magnetic field the ion temperature behaves in a similar fashion as the arcing voltage with respect to current. At a high magnetic field strength, and relatively low currents, when the arc is in the multiple arc regime during the whole sinusoidal current wave,

the ion temperature is independent of the actual current value. At low axial magnetic field strengths, where the arc is in the diffuse arc regime at current crest, the ion temperature increases with the current up to a value, which the ion temperature attains in absence of an axial magnetic field.

Then the ion temperature is found to be constant 11 eV in the current range from 3 to 8 kA unlike the arc voltage, which increases from 24 to around 60 volts. Therefore, it is concluded that the ion temperature depends on the arcing regime.
At the ion densities prevailing in the high current vacuum arc (4.10^{21} m^{-3}) the observed ion temperatures imply a mean free path of the ions of less than 1 mm. This result differs significantly from the expectations, based on an ion velocity of approximately 1.4 10^4 m/s found in the low current vacuum arc (Dav 69, Coc 76) and based on an ion velocity of 8000 m/s in the afterglow of a 5 kA arc (Bau 76), that the vacuum arc remains flow dominated up to the high current arcing region.

Until now it was assumed that the broadening of the spectral line is only caused by the thermal motion of the emitting ions. But the large systematic velocities associated with the expanding ion flow emanating from the cathode spot might also contribute significantly to the observed broadening. Therefore, several flow velocity profiles are checked on their influence on line broadening. The line profiles caused by ions with a Maxwellian velocity (thermal) distribution, by a homogeneous in all directions expanding ion cloud (spherical distribution), and by

a preferentially in axial direction expanding ion cloud (cosine distribution) are shown in figure 6.2. The cosine and the spherical distribution both have a constant velocity. In the first column of table 6.1 the velocity is represented, at which the line profile attains half the intensity of the top. In the second column the ratio between the constant velocity and the thermal velocity estimated from the halfwidth of the line profile is represented. It shows that the constant velocity is about the thermal velocity regardless the velocity profile. So if the ion velocity distribution is either a spherical or a cosine distribution the ion

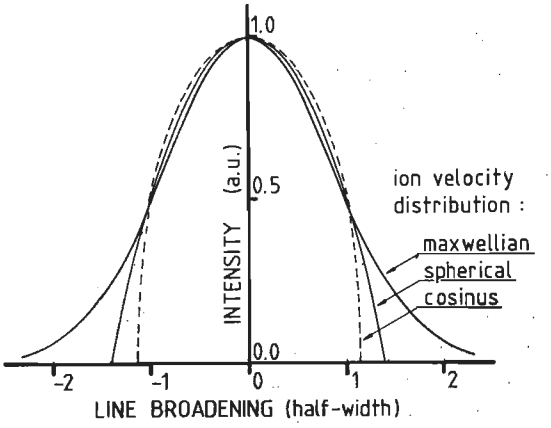

Figure 6.2 Line profiles corresponding to emitting particles with a Maxwellian, spherical and cosine velocity distribution.

TABLE 6.1 Influence of the ion velocity profile on the line broadening.

velocity profile	half width of line profile	ratio between maximum velocity and thermal velocity
Maxwellian	$v = o.84\ v_{th}$	-------
Homogeneous expanding flow	$v = 0.87\ v_{max}$	0.97
cosinus flow	$v = 0.71\ v_{max}$	1.19

velocity is between 5700 m/s at 0 mT and 3900 m/s at 100 mT. Thus, if the velocity distribution is determined by the properties of the cathode spot the velocity of the ions is much smaller in the high current vacuum arc than in the low current arc. As the cathode spots lie close together (the mean cathode spot separation in a 10 kA arc is about 3 mm), the expelled ion flows mix already close to the cathode and in view of the short mean free path for ion-ion collisions the ions will tend to thermalize rather quickly.

Of course a systematic drift velocity will be superimposed on the thermal motion. But it can be stated that the ions (and the electrons) and thus the plasma, behave like a drifting fluid in contrast with a bundle of particles.

A consequence of this conclusion is, that the systematic velocities will stay smaller than the thermal velocity. This is in fact also observed. For instance:

- the azimuthal ion velocity (cf. section 4.4) measured only at 25 mT increases proportionally with the radius and reaches a velocity of about 800 m/s at the periphery of the arc.
- the radial ion velocity when close to the thermal velocity would cause a distorsion of the Gaussian line profile, which is not observed. An estimation of the radial ion velocity yields a value comparable to the azimuthal ion velocity (cf. chapter 6.6).
- the axial ion velocity can be estimated from the ion current. Kimblin has shown that the ions carry about 10% of the arc current (Kim 73), which implies a mean axial ion velocity of 500 m/s.

The magnitude of the ion temperature depends on external parameters. Thus the temperature is not only determined by the proporties of the cathode spot. So, it is not excluded that ion heating takes place in the interelectrode plasma. On the other hand the high ion temperature can also be due to the thermalization of the very fast ion and neutral jets in the vacuum arc

plasma, or the ions can cool through collisions with the cold neutrals entering the arc from the cold recombination zones. Also electrons can cool the ions.

Only more refined line broadening measurements focussed on the interface between plasma ball and interelectrode plasma will bring some insight into the ion heating mechanism.

6.3 Electron Density

A comparison of the interferometric measurements with the continuum measurements puts an upper bound to

$$\xi_{fb}(1-\exp(-hc/\lambda kT_e)) + \xi_{ff}\exp(-hc/\lambda kT_e) \simeq 1 \quad (6.2)$$

with an uncertainty of around 20% (Loc 68). This means that the measured continuum intensity is indeed due to the free-bound (recombination) and free-free radiation. This is also to be expected at the electron density prevailing in the arc. The electron density may thus be determined from the continuum measurements (Mae 54, Gra 68, Ven 73), which contrary to the interferometric measurements did not suffer from mechanical noise. As the continuum intensity scales with the electron density squared, the uncertainty introduced by Abel inversion is reduced and detailed

information is thus gained about the spatial dependence of the electron density. In contrast to the temperature the density is strongly dependent on the current.

Many reports exist about electron density measurements in high current vacuum arcs including a report of an arc in an axial magnetic field.
Boxman (Box 74) and Harris (Har 78) both published electron density measurements made with a CO_2-laser interferometer at a wavelength of 10.6 $/^{um}$. The measurements were performed in a vacuum arc burning on copper electrodes of 25 mm diameter at the transition to anode spot formation. Webster and Sherman measured the electron density with an electrostatic probe in a 4.7 kA arc on 75 mm diameter electrodes (Web 76). The electron density they find, is substantially lower than the interferometric results. This may be due to emission of the probe. Kaneda e.a.

measured the broadening of a line and derived from the observed Stark broadening, the electron density. These measurements were performed on a vacuum arc in an axial magnetic field (Kan 81). Their results give significantly higher densities. There are indications that there are more than one spectral line within the apparatus profile, which would lead to an overestimated line broadening and hence of the electron density.

The peak electron densities observed by the various authors and determined in this study are represented in figure 6.3. It shows that a good agreement is found with the results of Boxman, who measured the electron density in the same way as is done in this study.

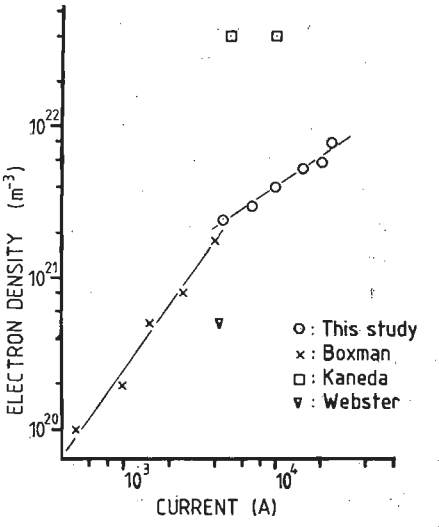

Figure 6.3 Peak electron density versus current as reported by various authors.

6.4 Effective charge

The ion density can be derived from the electron density if one type of ion is present.
If more types of ions are present the density of the ion with charge number Z, n_z, can be obtained from the density of an excited state of the atomic system Z-1, of which the particular ion with charge number Z forms the continuum (cf. the Saha equation chapter 4.1)

This method is only applicable if the used level in the Z-1 system is in (partial) local thermal equilibrium with the continuum state. Z.
This situation prevails in a part of the atomic systems of Cu I and Cu II near the cathode and thus the densities of singly and doubly ionized copper can be found. The effective charge, defined as

$$Z = \frac{n^{+} + 2n^{++}}{n^{+} + n^{++}} \qquad (6.3)$$

in absence of triply and higher ionized particles, is found to be about 1.17 near the cathode.

Further away from the cathode PLTE does not prevail, so only an upper estimate of the doubly charged ion density can be made. In table 6.2 the upper estimates of the ratio between doubly ionized copper density and the electron density are listed for various axial positions in the arc.
The density of triply ionized copper is obtained in a similar way from the spectral

TABLE 6.2 Ratio between ion and electron density for doubly and triply charged ions, and also the effective charge in a 10 kA arc.

distance from the cathode (mm)	n^{++}/n_e	n^{+++}/n_e	Z_{eff}
1	0.15	0.00007	1.17
3	0.06	0.00010	1.06
5	0.01	0.00011	1.01
7	0.008	0.00010	1.01
9	0.005	0.00005	1.00

line intensity of doubly ionized copper under the assumption of PLTE, which is very likely to be inappropriate.
Thus only an uppervalue for the triply charged ion density is obtained being approximately 10^{-4} times the electron density. This triply ionized ion density can be neglected in the calculation of the effective charge. Except for the region closest to the cathode the effective charge listed in table 6.2 is an upper estimate. Therefore is can be stated that for most of the arc the plasma is singly ionized. This result is in contrast to the findings of Davis and Miller. They found from measurements with a mass spectrometer in a 100 A copper arc the effective charge to be 1.85 with even a large proportion of the ions triply ionized (Dav 69).
Goldsmith and Boxman (Gol 81) however did not find any doubly charged ions in a high current cadmium arc using a spectroscopic measurement technique. The results listed in table 6.2 do not exclude a higher effective charge closer towards the cathode.

6.5 Pressure

Now that the charged particle densities and temperatures are known the total pressure inside the arc can be calculated with Dalton's law: the sum of the partial pressures of each of the constituents give the total charged particle pressure:

$$p = n_e kT_e + n^+ kT^+ + n^{++} kT^{++} \quad (6.4)$$

(The neutral particle influence will be discussed below in section 6.6). The temperature of the doubly charged ions is unknown, but it is very unlikely, that it deviates strongly from the observed temperature of the singly charged ions, because the energy relaxation time between the doubly and singly charged ions is even shorter (by a factor 4) than the thermalization time for the singly charged ions (the ion-ion collision time). Thus both ion temperatures are expected to be the same. The density of triply and higher charged ions is so low, that its influence on the arc pressure can be neglected, as may be done also for the doubly charged ions outside the region just in front of the cathode.

The pressure of charge particles has been calculated as function of the radial position at three axial positions, where the electron density was known: 2 mm above the cathode, halfway the electrodes and 2 mm. before the anode. Through these three axial points a least square approximation did give the pressure as a function of the distance to the cathode:

$$P = P_{cath} + \frac{\partial P}{\partial z} (z - z_{cath}) \quad (6.5)$$

With this linear analytic expression the pressure on any axial position has been calculated. As this was done for each radial position, the pressure is known everywhere in the arc. Connecting the places with equal pressure gives contours and by filling the region between the contours with black and white colouring results in a representation of the pressure in the vacuum arc as is shown in figure 6.4. This figure shows the pressure in a 10 kA arc at various axial magnetic field strengths, from 100 mT down to 8 mT which is just below the threshold for anode spot formation. One notices directly that with decreasing magnetic field strenght the axial pressure drop increases and reaches values comparable to the radial pressure drop.

As the variation of the temperature with position is neglectable, the observed variation of the pressure is mostly due to a variation of the particle density with position.

6.6 Neutral copper density

The laser interferometric measurement of the refractive index yielded beside the electron density also the neutral copper density. The accuracy is limited due to the uncertainty in the polarizability of neutral copper. The neutral density integrated along the line of sight appears to be five times higher than the integrated electron density. This is comparable with the findings of Boxman (Box 74). The spectroscopic measurements gave some additional information about the neutral particle density.
As both the copper neutral and the copper ion system are for a large part in the

complete excitation saturation phase, the ratio between the neutral and ion copper density can be found (c.f. chapter 4.1, Pot 79). Combining the laser and spectroscopic measurements a crude estimate of the radial dependence of the neutral copper density is obtained (see figure 4.18). From this figure one can conclude that in the middle of the arc the neutral density amounts to 20% of the electron density increasing a twentyfold towards the chamber walls.

The ionization degree is thus 80% in the arc centre decreasing towards the arc boundaries. Remarkable is also the time lag between the increase of the neutral density and the increase of the electron density. This time lag is about 1 ms in a 100 Hz arc and 2 ms in a 50 Hz arc.

The absolute value of the neutral density remains very uncertain. A miscalculation of a factor 3 is not improbable, by both the certainty of the polarizability and the certainty in the spatial dependence of the neutral density outside the electrode region.

Now several sources of neutral particles will be investigated on their relative importance, after which the cause of the observed time lag will be discussed. The neutral particles may originate from:

- the cathode spots. These hot emission sites wander across the cathode and leave small craters behind with typical dimensions of several micrometers (Daa 74, Daa 78).
  These just abandoned craters have temperatures near the boiling point of the electrode material and they lose their thermal energy by evaporation and heat conduction.

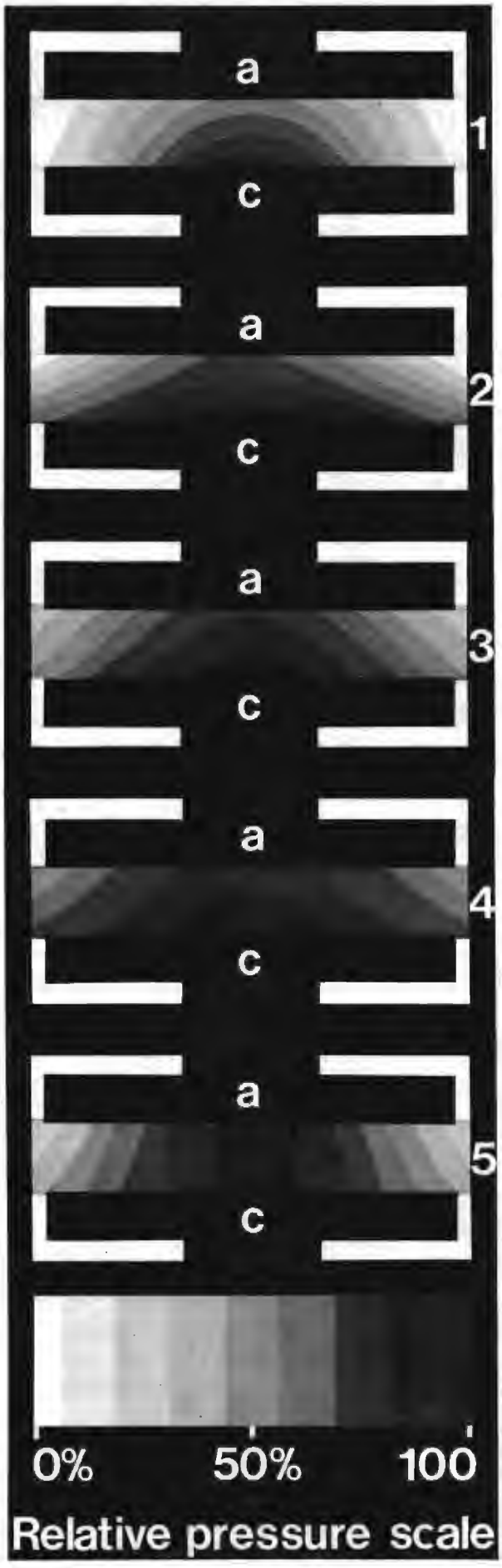

Figure 6.4 Pressure distribution in the high current vacuum arc, 10 kA, for various axial magnetic field strengths. a = anode; c = cathode
1. at 8 mT peak pressure 9000 Pa
2. at 15 mT peak pressure 7900 Pa
3. at 25 mT peak pressure 7100 Pa
4. at 50 mT peak pressure 6100 Pa
5. at 100 mT peak pressure 4800 Pa

So these craters may supply the arc with neutrals from the cathode side.

- the anode spot: In the current range investigated no luminous anode spot was present. This does not exclude molten areas on the anode, but near the melting point evaporation of electrode material is neglectable.
- the microdroplets: These droplets find their origin in places with high temperature and are flying into the arc with velocities of about 20 - 200 m/s. The droplets cool by evaporation and radiation.
  Boxman (Box 80a) shows that the contribution of microdroplet evaporation to the neutral density can be neglected.
- the sputtering of neutrals. When particles hit a wall with high energy, they can liberate atoms from the metal bulk (Mil 79).
  The high energy particles hitting the walls of the vacuum chamber will also liberate iron, but, as this element is not found in the emission spectrum of the vacuum arc, this process is not likely to be a dominant one in the present study.
- recombination of ions. As already discussed in chapter 5, volume recombination in the arc is neglectable and can thus not explain the high neutral density.
  Near cold surfaces as there are the electrodes and the walls of the vacuum chamber three particle recombination might become important. This would explain the observed build up of neutrals near the walls. The neutral density in the middle of the arc may be an equilibrium between a flow of neutrals from the recombination zones, caused by the large neutral density gradient, and by the ionization of the neutrals which is most frequent near the arc axis.

From the above mentioned sources only recombination would explain the observed spatial variation. The high neutral density may then be a consequence of a long neutral lifetime, longer than the ion lifetime. This is supported by the neutral density measurements of Jenkins after current interruption (Jen 75). The relatively long neutral lifetime hypothesis, which would explain the observed time lag, is supported by erosion measurements. The erosion rate in the high current vacuum arc in the present study amounts to 46.10^{-9} kg/C which is comparable to the ion mass erosion rate as reported by Daalder (Daa 75).

The total mass associated with the observed neutral density ($5.10^{21} m^{-3}$) in a discharge volume of approximately 300 cc is about 0.16 mg. This amount of mass is liberated by a 10 kA arc in 0.4 ms. If the fraction of droplet is taken into account, which is about 50% (Daa 76), the neutral lifetime is of the order of 1 ms, which corresponds to the observed timelag.

The consequence of the high neutral density will now be discussed. The collission cross section for neutral-ion collisions is 8.10^{-19} m^2 for velocities corresponding to a temperature of 1 eV. (Abd 80). Thus the collision frequency of this induced dipole collision at a neutral density of 10^{21} is about $1,6.10^6$ Hz, compared to 7.10^6 Hz of the ion-ion collision frequency. By this high ion-neutral collision frequency ion-neutral friction dominates in the law of Navier-Stokes. As a consequence of this the ion velocity is limited to values not exceding 1000 m/s, which is confirmed by indirect experimental evidence for the axial ion velocity (cf. section 6.2) and by experimental results for the azimuthal ion velocity (cf. chapter 4.4).

Thus in the high current vacuum arc the ion velocity is much smaller than in the low current vacuum arc, and in correspondence with the demands imposed by the magnetohydrodynamic theory.

The influence of the large neutral density on the radial pressure balance will be discussed in the next section.

6.7 Current density

The main interest regarding the current density lies in the axial current density, as this determines the current flow in the plasma. Knowledge about the current flow pattern before anode spot formation might reveal the causal relation between the anode spot and the current constriction,

which is evident after the formation of the anode spot. In a previous publication of the author (Sch 81) measurements of the axial current density near the anode are presented, made with a so called multiprobe anode. As a consequence of its construction the electrode could not withstand the heat flow which is attended with currents in excess of those reported in that paper.
Measurements with an electrode consisting of rings connected to each other with shunts having resistances as low as 200 $\mu\Omega$ influenced the current distribution in the anode in such a way that each ring carried the same amount of current (see figure 6.5).

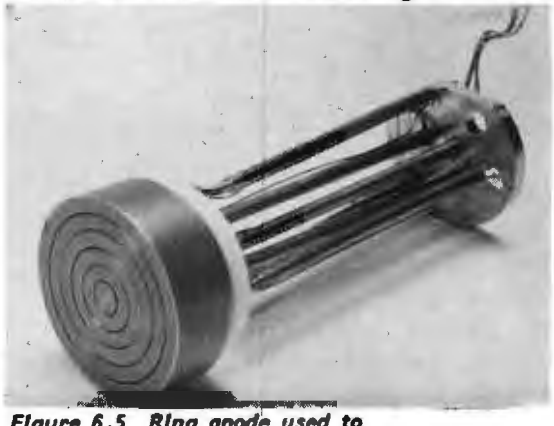

Figure 6.5 Ring anode used to measure the axial current density

A reduction of the resistance of the shunts increased the relative influence of the inductive noise on the measurements signals which hindered the interpretation of the signals completely. Therefore in evaluating the current density only the diamagnetic loop measurements are left.

The azimuthal current density is found from the diamagnetic loop measurements (cf chapter 4.3).
With relation 5.18 derived from the momentum balance of the electrons one obtains the radial current density from the azimuthal current density (see figure 6.6). This figure shows that at 100 mT the radial current density is two orders of magnitude smaller than at 8 mT. The axial magnetic field thus tremendously reduces the radial current density.
At low applied axial magnetic fields the determination of the radial current density is inaccurate, due to the axial magnetic field generated by the azimuthal plasma current.

With this radial current density the axial

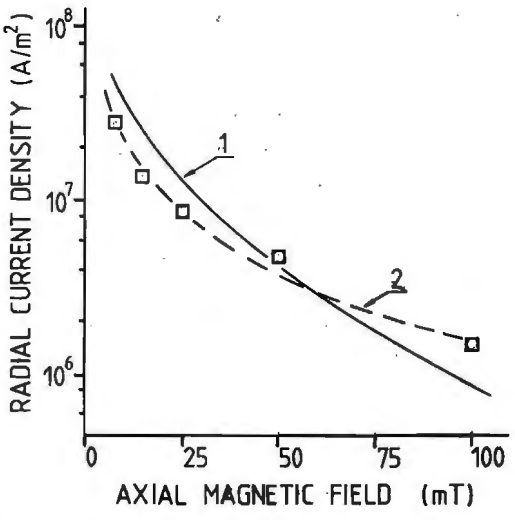

Figure 6.6 Radial current density versus axial magnetic field strength.
1. derived from azimuthal current density (peak value)
2. derived from the axial pressure drop

current density can be calculated using Kirchoff's law.
From the axial current density the current flow lines in the vacuum arc can be obtained. The variation of the radial current density profile with axial position is not known, and depends on the assumed axial profile of the azimuthal current density. Since this profile is assumed to be independant on axial position, the calculation of the current flow lines should be considered as a first order approximation.
In figure 6.7 the current flow lines are represented for a 10 kA arc at various axial magnetic fields.

At low axial magnetic fields the current flow concentrates towards the middle of the arc. At high axial magnetic fields the current flow lines connect the anode with the cathode along the shortest path causing a more homogeneously distributed current density at the anode.
Agarwal and Holmes (Aga 78) obtained similar results from magnetic probe measurements in a 8.7 kA vacuum arc between 75 mm diameter contacts with a 15 mm clearance. They also found the current to constrict at 0 mT axial magnetic fieldstrength and to remain homogeneous at 200 mT. Thus the high radial current density causes a current constriction in front of the anode before anode spot formation.

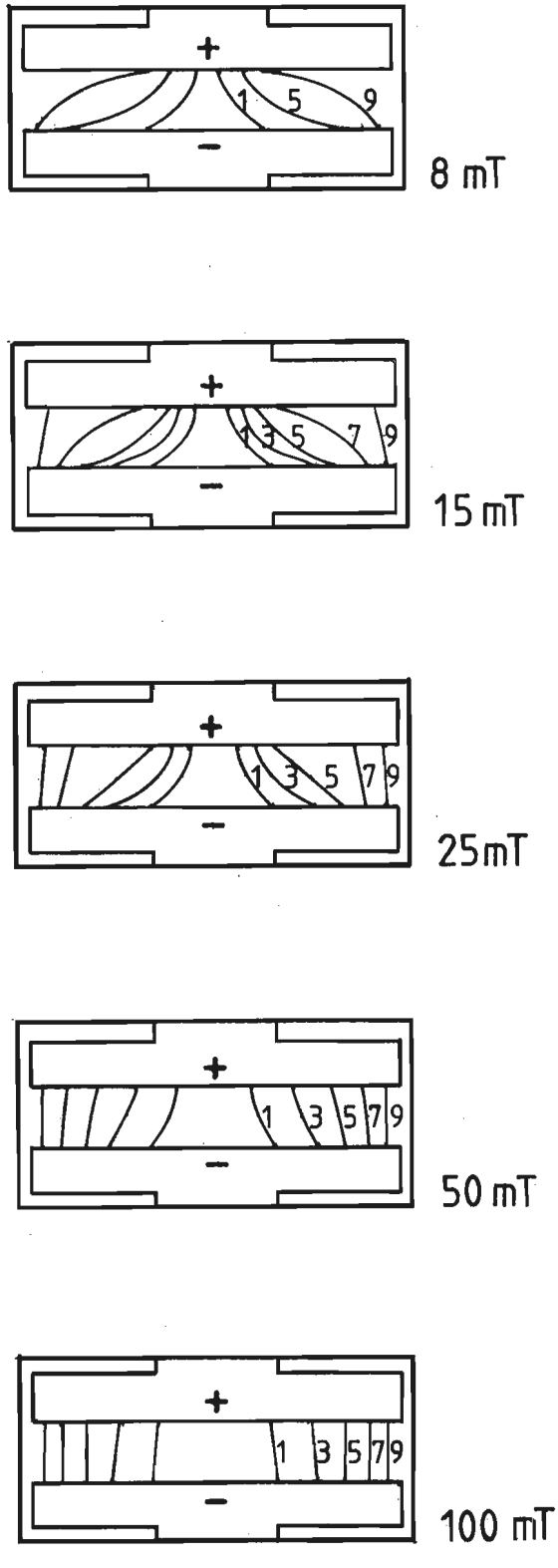

Figure 6.7 Current flow lines in the high current vacuum arc, 10 kA for various axial magnetic field strengths. The numbers indicate the amount of current (kA) flowing inside the surface represented by the curve.

Now the current densities in the arc are determined, a closer look to the pressure balances can be made for a specific set of parameters.

As shown in chapter 5 the radial pressure balance can be written as

$$\frac{\partial(p^e+p^i)}{\partial r} = j_\theta B_z - j_z B_\theta - nm_i w_r^i \frac{\partial}{r\partial r} w_r^i - nm_i (w_r^i - w_r^o)\nu^{io'} \qquad (6.6)$$

In tabel 6.3. the estimated magnitude of the terms of equation 5.28 are given for a 10 kA arc at 25 mT for various radial positions.

In the pinch force $j_z B_\theta$ is estimated on basis of a mean axial current density and of an azimuthal magnetic field produced by an infinitely long cylindrically symmetric arc.
The other component, $j_\theta B_z$, is estimated on basis of the mean azimuthal current density obtained from the diamagnetic loop measurements. In the calculation of the axial magnetic field it is not taken into account that the azimuthal current density reinforces the externally applied axial magnetic field.
From the table it can be seen that the forces exerted by the axial and azimuthal currents are of the same magnitude.
The plasma currents thus exert in first order no force in radial direction. The magnetic fields associated with this current density distribution are close to what is called "forcefree fields" (Lun 50). These forcefree fields are present also in other types of discharges, particularly in the cold gas surrounding the hot cores of tokamaks. (Bob 68, Laa 76). Looking again

Table 6.3 : The radial force density at various radial positions for a 10 kA arc at 25 mT.

radius	radial force density in 10^5 N/m^3			
r	$\frac{\partial(p^e+p^i)}{\partial r} = j_\theta B_z - j_z B_\theta - (nm_i w_r^i \frac{\partial}{r\partial r} w_r^i + nm_i (w_r^i - w_r^o)\nu^{io'}$			
0	0	0	0	0
5	-0.8	1.1	-1.0	-0.9
10	-1.6	1.6	-1.2	-2.0
15	-2.1	1.4	-1.0	-2.5
20	-2.2	0.9	-1.1	-2.0
25	-2.1	0.5	-1.5	-1.1
30	-1.8	0.2	-2.0	0

to the vacuum arc the radial charged particle pressure gradient has to be mainly balanced by ion neutral friction in the presence of force free fields. Based on this a maximum radial ion velocity can be estimated for a 10 kA arc at 25 mT of around 500 m/s.

This confirms the supposition that all systematic ion velocities are of the same order of magnitude and smaller than the ion thermal velocity.

The axial pressure balance is

$$\frac{\partial(p^e+p^i)}{\partial z} = j_r B_\theta - nm_i(w_z^i - w_z^o)\nu^{io} \quad (6.7)$$

No knowledge is available about the ion-neutral friction because experimental knowledge about the difference between the axial and neutral velocity is lacking. Figure 6.8 shows the difference between the axial pressure gradient and the

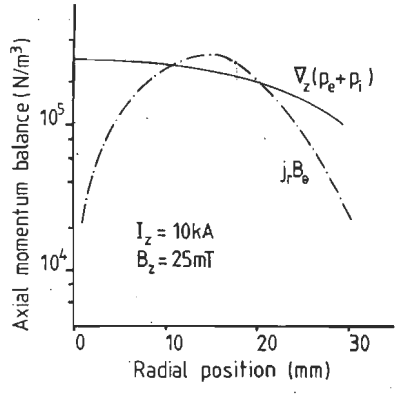

Figure 6.8 The force density in axial direction exerted by the pressure drop and the radial current density for a 10 kA arc at 25 mT at various radial positions.

Lorentz force exerted by the radial current density for a 10 kA arc at 25 mT. At intermediate radii the pressure gradient appears to be approximately balanced by the radial current density. In figure 6.6 the calculated radial current density is compared with the pressure term:

$$j_r = \frac{1}{B_\theta}\frac{\partial(p^e+p^i)}{\partial z} \quad (6.8)$$

of equation 6.7. This comparison is performed at the radial position where the radial current density obtained from the azimuthal current density is at its maximum. From the close correspondence between both current densities it can be concluded that at that position a significant fraction of the axial pressure drop is balanced by the Lorentz force exerted by a radial current density.

The part of the axial pressure drop not balanced by the Lorentz force accelerates the ions until ion-neutral friction is sufficient.

6.8 Arc voltage

In chapter 2 it was stated that the positive current voltage relationship is one of the features of the diffuse high vacuum arc (see figure 2.1). Measurements have shown that at low axial magnetic fields the arc voltage of a high current vacuum arc deviates from the arc voltage of a single 100 A arc, whereas at high axial magnetic fields, both are equal (see figure 2.15). Below the cause of the difference between arc voltage of a high current arc and of a 100 A arc at low axial magnetic fields will be discussed on the basis of the theory developed in chapter 5, the measurements of chapter 4 and the preceding discussions.

In chapter 5 it was derived on basis of the momentum balance equation, that the axial electric field in the interelectrode plasma could be splitted in at least an Ohmic electric field, and a "additional" electric field.

By integrating the Ohmic electric field and the pressure drop electric field over the axial extension of the interlectrode region from the plasma ball in front of the cathode up to the sheath edge in front of the anode the voltage drop across the interelectrode plasma is obtained. Adding to this voltage the cathode voltage drop and the voltage drop across the anode sheath the total arc voltage is obtained.

$$V_{arc} = V_{cath} - \int E_z^{Ohms} dz - \int E_z' \, dz + V_{an} \quad (6.9)$$

The voltage drop at the cathode is known by the work of Reece (Ree 63) and is independent of the radial position on the contact. The anode voltage drop on the other hand is not known, but is supposed to be small compared to the cathode voltage drop and will therefore be omitted.
In evaluating the additional electric field from the experimental data

equation 5.27 although illustrative is less useful by the lack of information about the neutral pressure distribution. Therefore, this electric field has been calculated using the identical equation 5.26. The Ohmic electric field can be calculated with equation 5.24 from the axial current density derived in the preceding paragraph. By integrating the two electric fields from cathode to anode the corresponding voltages are obtained. In figure 6.9 the contribution of the cathode voltage drop, of the additional voltage and of the Ohmic voltage to the total arc voltage are shown for the arcing region close to the arc axis for a 10 kA arc at 15 mT. Due to the current constriction the Ohmic voltage is greatest at the arc axis. Away from the arc axis the additional voltage increases and is the most important. The remaining differences between measured and calculated arc voltages may be due to an underestimation of the plasma resistivity and to a deviation from the assumed current distribution.

It can be concluded that the observed agreement between the measured and calculated arc voltages is satisfactory.

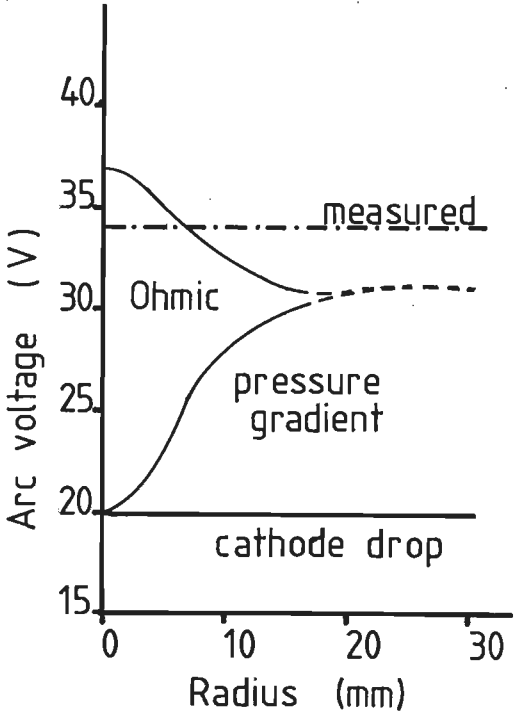

Figure 6.9 The arc voltage versus radial position for a 10 kA arc at 15 mT. The various sources that attribute to the arc voltage are shown.

This can be seen as a support of the here developed model of the diffuse arc.

6.9 Anode spot formation

In the present investigation no measurements were performed at the transition from the diffuse vacuum arc to the vacuum arc with a luminous vigorously evaporating spot on the anode, the anode spot. In fact this transition was always avoided during the experiments as the occurence of this spot limits the useful lifetime of the electrodes drastically. However, still some additional information regarding the formation of the anode spot has become available through this study. In section 6.7 the axial current density in the diffuse vacuum arc was discussed.

At low axial magnetic fields the current density near the center increases sharply towards the anode.
Figure 6.10 shows the peak axial current density as function of the axial magnetic field strength. Also the magnetic field, at which an anode spot occurs, is given. Remarkable is the correspondence between the here found current density near to anode spot formation ($9.10^7 A/m^2$) and the critical current density for the anode constriction instability ($6.10^7 A/m^2$) calculated by Ecker for a homogeneous short gap model (Eck 74).
This result is remarkable as some of the model assumptions in Ecker's model are in contradiction with the experimental findings presented above.

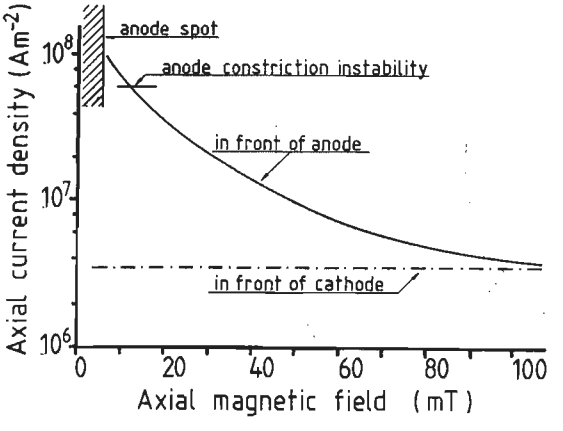

Figure 6.10 Peak axial current density in front of the anode versus axial magnetic field strength.

In the homogeneous short gap model it is assumed that in the interelectrode plasma the interaction between the particles is negligible (collisionless) and that the voltage drop is only across the cathode, the cathode spot voltage, and across the anode sheath edge. However, from the measurements is concluded that the interaction between the particles is collision dominated and that due to radial currents a voltage drop in the interelectrode plasma exists. So the agreement between the here obtained result and the prediction of the homogeneous short gap model is accidental, because Ecker's model cannot be applied to the interelectrode region.

Close to the anode not only the axial current density increases, but also the total voltage drop across the arc with decreasing axial magnetic field. The energy loss in the arc increases thus even faster.

Ultimately the total amount of energy dissipated by the vacuum arc is converted into heat, which accumulates in the electrodes and the shield surrounding the arcing volume. Measurements by Gundersen and Foosnaes (Gun 71, Foo 79) show, that approximately 60% of the energy is delivered to the anode.

Cobine and Burger (Cob 54) calculated the energy loss rate of a metallic surface due to the radiation and evaporation as a function of the temperature of the metal. (see figure 6.11).

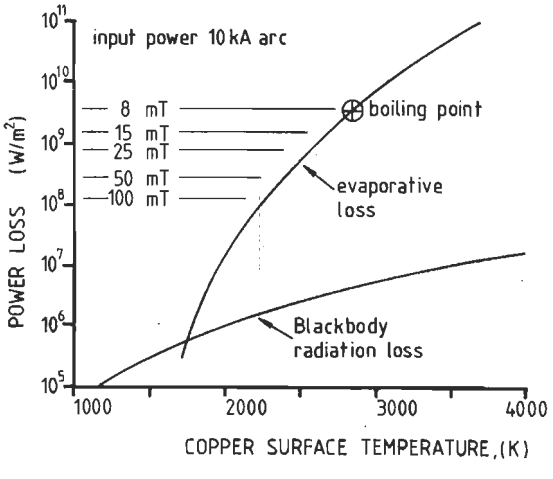

Figure 6.11 Energy loss rate of a copper surface versus the copper temperature. The peak heat input into the cathode is also represented for various axial magnetic fields.

With a constant heat input into the anode the steady state temperature of the anode can be derived from this figure. For the 10 kA arc studied here, the maximum heat input into the anode at various axial magnetic fields is also represented in this figure. It is clear from figure 6.11 that already at moderate magnetic field strengths melting occurs. At 8 mT the atmospheric boiling point of the copper anode is almost reached. In reality at 6 mT an anode spot is present.

From this it is concluded that the transition to the anode spot regime is due to a preceding current constriction.

7 Conclusions

a. At a fixed axial magnetic field the vacuum arc passes with increasing current through three different arcing regimes:
- the multiple arc regime; here the arc is split up in separate arc channels. Each arc channel is fed from a single cathode spot. Here is no measurable interaction of the arc channel with the background plasma.
- the diffuse arc regime; the arc is fed from a multitude of cathode spots covering the whole electrode. No distinction can be made between the arc channels and the background plasma and the arc behaves like a diffuse plasma.
- the anode spot regime; the arc is fed from a multitude of cathode spots and a large molten spot on the anode.

b. In the diffuse arc the mean free paths of ions and electrons are smaller than the characteristic dimensions of the arc. So, the arc is collision dominated and the behaviour of the particles can be described by magnetohydrodynamic theory. As the electron Hall parameter is close to 1, only the electrons are influenced by the azimuthal magnetic field as well as the axial magnetic field.

c. The analysis of the magnetohydrodynamic equations shows a direct relationship between the azimuthal current density and the radial current density. The existence of a positive azimuthal current density leads hence to a positive radial current density. The latter causes a current constriction at the anode. The positive azimuthal current density implies an almost force-free flow of the current through the arc.

d. The positive current voltage relationship of the diffuse vacuum arc is not due to an increased resistivity of the plasma, because the electron temperature is not found to depend on the arcing parameters. The large radial currents generate in the outer parts of the arc an additional axial electric field, which forces the current towards the arc centre. In order for the arc to be able to carry the current imposed by the external electrical circuit, the Ohmic voltage drop has to increase in the middle of the arc. Therefore, it is concluded that a significant voltage drop is across the interelectrode plasma. The close correspondence between the measured and the calculated arc voltage is a support for the here presented model of the diffuse arc.

e. The current constriction causes an enhanced energy dissipation in the plasma. This leads to evaporation of anode material. Calculations show that at low applied axial magnetic fields the anode heats up to its atmospheric boiling temperature For these conditions experimentally an anode spot is indeed observed. Therefore, it is concluded that the transition from the diffuse arc regime to the anode spot regime is related to the energy dissipation in the diffuse arc.

f. Measurements show that the Lorentz force exerted by the radial current density balances a significant fraction of the axial charged particle pressure gradient. The remaining fraction is balanced by ion neutral friction. In the radial component of Navier Stokes measurements indicate that ion neutral friction is comparable to the radial charged particle pressure gradient. At present these qualitative statements about ion neutral friction can not be verified quantitatively. Thus a detailed study of the behaviour of the neutrals is justified.

g. The axial magnetic field affects the arc in at least two ways.
   - With increasing axial magnetic field the radius of a single arc channel decreases and the particle density inside increases. This leads to an increase of the value of the main current at which the interaction between the arc channel and the background plasma occurs. Thus the concentration of the current flow in the diffuse arc appears at larger currents.
   - With increasing axial magnetic field the radial current density decreases. This results in a reduced current constriction. Also because of this effect the anode spot formation occurs for larger currents.

   The latter affects the arc already at moderate axial magnetic field strengths, whereas the former influences the arc at high magnetic fields.

h. The main cause of the anode spot is identified as the enhanced energy dissipation due to a current constriction in the diffuse vacuum arc. The electron momentum balance is found to determine the current flow lines. With this knowledge it will be possible to design the arcing region: i.e. electrode geometry and magnetic field configuration, in order to distribute the current more homogeneously at the anode surface. In this way anode spot formation may be prevented more effectively.

APPENDIX A

Estimation of the various terms in the momentum balances.

The momentum balance can be written as:

$$nm\left(\frac{\partial}{\partial t} + \underline{w}\cdot\nabla\right)\underline{w} = nq\left(\underline{E} + \underline{w}\times\underline{B}\right) - \nabla p - \nabla\cdot\underline{\underline{\Pi}} - \underline{R}$$

The various contributions to the momentum balances of electrons and ions will now be estimated.

The following simplifications are made:

- cylindrical coordinate system
- rotational symmetry $\frac{\partial}{\partial\theta} = 0$
- stationary state $\frac{\partial}{\partial t} = 0$
- velocity profile:

  $w_r = \xi_r(z)\ v_{th}\frac{r}{\Lambda}\exp\{-(r/\Lambda)^2\}$

  $w_\theta = \xi_\theta(z)\ v_{th}\frac{r}{\Lambda}\exp\{-(r/\Lambda)^2\}$

  $w_z = \xi_z(z)\ v_{th}\exp\{-(r/\Lambda)^2\}$

  and $\xi_j(z) = \xi_j\exp(-z/L)$
- pressure profile:

  $p = nkT\ f(z)\exp\{-(r/\Lambda)^2\}$

  $f(z) = \exp-(z/L)$
- temperature profile

  $T = Tg(z)\exp\{-(r/\Lambda_T)^2\}$

  $g(z) = \exp-(z/L_T)$

(these profiles are ad hoc assumptions, but enable an estimation of the importance of viscosity and inertia, which play a role in the ion momentum balance)

- electron viscosity and inertia are neglected
- all components of the systematic electron velocities are large compared to the corresponding systematic ion velocities
- in the estimates the neutral velocities will be ignored
- λ_i is the mean free path for ion-ion collisions
- λ_e is the mean free path for electron-electron collisions
- λ'_{io} is the mean free path for ion-neutral collisions taking ionization into account

  $\lambda'_{io} = v^i_{th}/\nu^{io'}$
- the temperature gradients are small compared to the pressure gradients: $\Lambda_T >> \Lambda$ and $L_T >> L$

The ion viscosity coefficients and the electron-ion collision time are taken from Braginskii

The various terms in the momentum balances are compared with the pressure gradient. First the viscosity will be estimated. Thereafter the momentum balances of ions and electrons will follow.

Estimation of the ion viscosity

Table A1 Ion viscosity in radial direction

$(\nabla\cdot\underline{\underline{\Pi}})^i_r$	$\lvert(\nabla\cdot\underline{\underline{\Pi}})^i_r/\frac{\partial p^i}{\partial r}\rvert$
$-2\eta_1\frac{\partial}{\partial r}\frac{w^i_r}{r}$	$\xi^i_r\cdot\lambda_i/\Lambda$
$-2\eta_3\frac{\partial}{\partial r}\frac{w^i_\theta}{r}$	$\xi^i_\theta\cdot\Omega_i\tau_i\lambda_i/\Lambda$
$-\frac{1}{3}\frac{\partial}{\partial r}\eta_0\frac{\partial w^i_r}{\partial r}$	$\xi^i_r\cdot\lambda_i/\Lambda$
$-\frac{1}{3}\frac{\partial}{\partial r}\eta_0\frac{w^i_r}{r}$	$\xi^i_r\cdot\lambda_i/\Lambda$
$\frac{2}{3}\frac{\partial}{\partial r}\eta_0\frac{\partial w^i_z}{\partial z}$	$\xi^i_z\cdot\lambda_i/L$
$-\frac{\partial}{\partial r}\eta_1 r\frac{\partial}{\partial r}\frac{w^i_r}{r}$	$\xi^i_r\cdot\lambda_i/\Lambda$
$-\frac{\partial}{\partial r}\eta_3 r\frac{\partial}{\partial r}\frac{w^i_\theta}{r}$	$\xi^i_\theta\cdot\Omega_i\tau_i\lambda_i/\Lambda$
$-\frac{\partial}{\partial z}\eta_2\frac{\partial}{\partial r}w^i_z$	$\xi^i_z\cdot\lambda_i/L$
$-\frac{\partial}{\partial z}\eta_2\frac{\partial}{\partial z}w^i_r$	$\xi^i_r\cdot\lambda_i\Lambda/L^2$
$-\frac{\partial}{\partial z}\eta_4\frac{\partial}{\partial z}w^i_\theta$	$\xi^i_\theta\cdot\Omega_i\tau_i\lambda_i\Lambda/L^2$

The viscosity coefficients of the ions are :

(for $\Omega_i\tau_i << 1$)

$\eta_0 = 0.96\ n_i kT_i\tau_i$ $\qquad$ $\eta_3 = 2\Omega_i\tau_i\cdot n_i kT_i\tau_i$

$\eta_1 = \eta_2 = \eta_0$ $\qquad$ $\eta_4 = 0.5\eta_3$

Table A2 Ion viscosity in azimuthal direction

$(\nabla\cdot\underline{\underline{\Pi}})_\theta$	$\lvert(\nabla\cdot\underline{\underline{\Pi}})_\theta/\frac{\partial p^i}{\partial r}\rvert$
$-\frac{\partial}{\partial r}\eta_1 r\frac{\partial}{\partial r}\frac{w^i_\theta}{r}$	$\xi^i_\theta\lambda_i/\Lambda$
$\frac{\partial}{\partial r}\eta_3 r\frac{\partial}{\partial r}\frac{w^i_r}{r}$	$\xi^i_r\Omega_i\tau_i\lambda_i/\Lambda$
$-2\eta_1\frac{\partial}{\partial r}\frac{w^i_\theta}{r}$	$\xi^i_\theta\lambda_i/\Lambda$
$2\eta_3\frac{\partial}{\partial r}\frac{w^i_r}{r}$	$\xi^i_r\Omega_i\tau_i\lambda_i/\Lambda$
$-\frac{\partial}{\partial z}\eta_2\frac{\partial w^i_\theta}{\partial z}$	$\xi^i_\theta\lambda_i\Lambda/L^2$
$\frac{\partial}{\partial z}\eta_4\frac{\partial w^i_z}{\partial r}$	$\xi^i_z\Omega_i\tau_i\lambda_i/L$
$\frac{\partial}{\partial z}\eta_4\frac{\partial w^i_r}{\partial z}$	$\xi^i_r\Omega_i\tau_i\lambda_i\Lambda/L^2$

Table A3 Ion viscosity in axial direction

$(\nabla\cdot\underline{\underline{\Pi}})_z$	$\left\|(\nabla\cdot\underline{\underline{\Pi}})_z / \frac{\partial p^i}{\partial z}\right\|$
$-\frac{\partial}{r\partial r} r \eta_2 \frac{\partial w_z^i}{\partial r}$	$\xi_z^i \lambda_i L/\Lambda^2$
$-\frac{\partial}{r\partial r} r \eta_2 \frac{\partial w_r^i}{\partial z}$	$\xi_r^i \lambda_i/\Lambda$
$-\frac{\partial}{r\partial r} r \eta_4 \frac{\partial w_\theta^i}{\partial z}$	$\xi_\theta^i \Omega_i \tau_i \lambda_i/\Lambda$
$\frac{2}{3}\frac{\partial}{\partial z} \eta_0 \frac{\partial w_r^i}{\partial r}$	$\xi_r^i \lambda/\Lambda$
$\frac{2}{3}\frac{\partial}{\partial z} \eta_0 \frac{w_r^i}{r}$	$\xi_r^i \lambda_i/\Lambda$
$-\frac{4}{3}\frac{\partial}{\partial z} \eta_0 \frac{\partial w_z^i}{\partial z}$	$\xi_z^i \lambda_i/L$

So even for systematic ion velocities approaching the ion thermal velocity the ion viscosity devided by the pressure gradient is smaller than:

λ_i/L or λ_i/Λ

Estimation of the momentum balance

Measurements show that:

- λ_i/L , λ_i/Λ are between 0.1 and 0.02
- all ξ for ions and electrons are smaller than 0.1 except $\xi_r^i < 1$
- $\Omega_i \tau_i \simeq 0.01$

These data will be used to derive the final results of this appendix.

Table A4 Radial component of the ion momentum balance

terms	$\left\|\text{terms} / \frac{\partial p^i}{\partial r}\right\|$
$nm_i w_r^i \frac{\partial}{\partial r} w_r^i$	$\xi_r^{i\,2}$
$-nm_i w_\theta^{i2}/r$	$\xi_\theta^{i\,2}$
$nm_i w_z^i \frac{\partial}{\partial z} w_r^i$	$\xi_z^i \xi_r^i \Lambda/L$
=	
$-\frac{\partial}{\partial r} p^i$	1
$-(\nabla\cdot\underline{\underline{\Pi}})_r$	λ_i/Λ
enE_r	$E_r \Lambda/\hat{T}_i$ (*)
$enw_\theta^i B_z$	$\Omega_i \tau_i \xi_\theta^i \Lambda/\lambda_i$
$-enw_z^i B_\theta$	$\Omega_i \tau_i \xi_z^i \Lambda/\lambda_i$
$-en\eta j_r$	$\xi_r^e \frac{\Lambda}{\lambda}\frac{T_e}{T_i}$
$\frac{3}{2}\frac{n}{\Omega_e \tau_e}\frac{B_\theta}{B_z}\frac{\partial}{\partial z} kT_e$	$\frac{1}{\Omega_e \tau_e}\frac{B_\theta}{B_z}\frac{T_e}{T_i}\frac{\Lambda}{L_T}$
$-nm_i(w_r^i - w_r^o)\nu^{io'}$	$\xi_r^i \Lambda/\lambda_{io}'$

The most important terms are:

$$nm_i w_r^i \frac{\partial}{\partial r} w_r^i = enE_r - \frac{\partial}{\partial r} p^i - en\eta j_r - nm_i (w_r^i - w_r^o)\nu^{io'}$$

(*) $\hat{T}$ represents the temperature in eV.

Table A5 Azimuthal component of the ion momentum balance.

terms	$\left\vert \text{terms}/\frac{\partial p^i}{\partial r} \right\vert$
$nm_i w_r^i \frac{\partial}{\partial r} w_\theta^i$	$\xi_r^i \xi_\theta^i$
$nm_i w_r^i w_\theta^i / r$	$\xi_r^i \xi_\theta^i$
$nm_i w_z^i \frac{\partial}{\partial z} w_\theta^i$	$\xi_z^i \xi_\theta^i \Lambda / L$
$=$	
$-enw_r^i B_z$	$\Omega_i \tau_i \xi_r^i \Lambda / \lambda_i$
$-(\nabla \cdot \underline{\underline{\Pi}})_\theta$	λ_i / Λ
$-en\eta j_\theta$	$\xi_\theta^e \frac{\Lambda}{\lambda_e} \frac{T_e}{T_i}$
$\frac{3}{2} \frac{n}{\Omega_e \tau_e} \frac{\partial}{\partial r} kT_e$	$\frac{B_\theta}{\Omega_e \tau_e B_z} \frac{\Lambda}{\Lambda_T}$
$-nm_i (w_\theta^i - w_\theta^o) \nu^{io'}$	$\xi_\theta^i \Lambda / \lambda_{io}'$

The most important terms are:

$$0 = -en\eta j_\theta - nm_i (w_\theta^i - w_\theta^o) \nu^{io'}$$

Table A6 Axial component of the ion momentum balance.

terms	$\left\vert \text{terms}/\frac{\partial p^i}{\partial z} \right\vert$
$nm_i w_r^i \frac{\partial}{\partial r} w_z^i$	$\xi_r^i \xi_z^i r^2 L / \Lambda^3$
$nm_i w_z^i \frac{\partial}{\partial z} w_z^i$	$\xi_z^{i\,2}$
$=$	
neE_z	$E_z L / \bar{T}_i$
$enw_r^i B_\theta$	$\Omega_i \tau_i \xi_r^i L / \lambda_i$
$-\frac{\partial}{\partial z} p^i$	1
$-(\nabla \cdot \underline{\underline{\Pi}})_z$	λ_i / L
$-en\eta j_z$	$\xi_z^e \frac{\Lambda}{\lambda_e} \frac{T_e}{T_i}$
$.71\, n \frac{\partial}{\partial z} kT_e$	$\frac{L}{L_T} \frac{T_e}{T_i}$
$-\frac{3}{2} \frac{1}{\Omega_e \tau_e} \frac{B_\theta}{B_z} \frac{\partial}{\partial r} kT_e$	$\frac{1}{\Omega_i \tau_i} \frac{B_\theta}{B_z} \frac{T_e}{T_i} \frac{L}{\Lambda_T}$
$-nm_i (w_z^i - w_z) \nu^{io'}$	$\xi_z^i \Lambda / \lambda_{io}'$

The most important terms are:

$$0' = enE_z - \frac{\partial}{\partial z} p^i - en\eta j_z - nm_i (w_z^i - w_z^o) \nu^{io'}$$

Table A7 Radial component of the electron momentum balance.

terms	terms / $\frac{\partial p^e}{\partial r}$
0	
=	
$-enE_r$	$E_r \Lambda/\hat{T}_e$
$-enw^e_\theta B_z$	$\Omega_e \tau_e \xi^e_\theta \Lambda/\lambda_e$
$enw^e_z B_\theta$	$\Omega_e \tau_e \xi^e_z \Lambda/\lambda_e$
$-\frac{\partial}{\partial r} p^e$	1
$enn j_r$	$\xi^e_r \Lambda/\lambda_e$
$-\frac{3}{2}\frac{n}{\Omega_e \tau_e}\frac{B_\theta}{B_z}\frac{\partial}{\partial z} kT_e$	$\frac{1}{\Omega_e \tau_e}\frac{B_\theta}{B_z}\frac{\Lambda}{L_T}$

The most important terms are:

$$0 = -enE_r - enw^e_\theta B_z + enw^e_z B_\theta - \frac{\partial}{\partial r} p^e + enn j_r$$

Table A8 Azimuthal component of the electron momentum balance.

terms	terms / $\frac{\partial p^e}{\partial r}$
0	
=	
$enw^e_r B_z$	$\Omega_e \tau_e \xi^e_r \Lambda/\lambda_e$
$enn j_\theta$	$\xi^e_\theta \Lambda/\lambda_e$
$-\frac{3}{2}\frac{n}{\Omega_e \tau_e}\frac{\partial}{\partial r} kT_e$	$\frac{1}{\Omega_e \tau_e}\frac{\Lambda}{\Lambda_T}$

The most important terms are:

$$0 = enw^e_r B_z + enn j_\theta$$

Table A9 Axial component of the electron momentum balance

terms	terms / $\frac{\partial p^e}{\partial z}$
0	
=	
$-enE_z$	$E_z L/\hat{T}_e$
$-enw^e_r B_\theta$	$\Omega_e \tau_e \xi^e_r L/\lambda_e$
$-\frac{\partial}{\partial z} p^e$	1
$enn j_z$	$\xi^e_z \Lambda/\lambda_e$
$-.71\, n\frac{\partial}{\partial z} kT_e$	L/L_T
$\frac{3}{2}\frac{n}{\Omega_e \tau_e}\frac{B_\theta}{B_z}\frac{\partial}{\partial r} kT_e$	$\frac{1}{\Omega_e \tau_e}\frac{B_\theta}{B_z}\frac{L}{\Lambda_T}$

The most important terms are:

$$0 = -enE_z - enw^e_r B_\theta - \frac{\partial p^e}{\partial z} + enn j_z$$

REFERENCES

Abd 80 H. Abdelhakim, J.P. Dingwirard and S. Vacquie, J. Phys. D, Appl. Phys. 13 (1980) 1427

Aga 78 M.S. Agarwal and R. Holmes, 5th Int. Conf. Gas Disc. London (1978) 277

Alc 66 H. Alcock and S Ramsden, Appl. Phys. Lett. 8 (1966) 137

Alp 59 R. Alpher and D. White, Phys. Fluids 2 (1959) 162

Ash 63 D.E.T.F. Ashby and D.F. Jephcott, Appl. Phys. Lett. 3 (1963) 13

Bat 49 D.R. Bates and A. Damgaard, Philos. Trans. Roy. Soc. London A, Mathm. and Phys. Scien. 242 (1949) 101

Bau 76 G.J. Bauer and R. Holmes, 4th Int. Conf. Gas Disc. London (1976) 303

Bie 75 A. Bielski, J. Quant. Spectrosc. Radiat. Transfer 15 (1975) 463

Bob 68 C. Bobeldijk, Plasma Phys. 10 (1968) 567

Box 74 R.L. Boxman, J. Appl. Phys. 45 (1974) 4835

Box 78 R.L. Boxman, J.H. Harris and A. Bless, IEEE Trans. Plasma Scienc. Ps-6 (1978) 233

Box 80 R.L. Boxman and S. Goldsmith, J. Appl. Phys. 51 (1980) 3644

Box 80a R.L. Boxman and S. Goldsmith, J. Appl. Phys. 52 (1980) 151

Bra 67 S. Braginskii, Revieuw of plasma physics, by M. Leontovich, Vol.1, Consultants bureau, New York, 1967

Cob 55 J.D. Cobine and E.E. Burger, J. Appl. Phys. 26 (1955) 895

Coc 76 W.M. Cock and J.E. Daalder 7th Int. Symp. Disc. Elec. Insul. Vac., Novosibirsk, USSR (1976) 288

Daa 74 J.E. Daalder, IEEE Trans. Power Appar. Syst. Pas-93 (1974) 1747

Daa 75 J.E. Daalder, J. Phys. D, Appl. Phys. 8 (1975) 1647

Daa 76 J.E. Daalder, J. Phys. D, Appl. Phys. 9 (1976) 2379

Daa 78 J.E. Daalder, Thesis, Cathode erosion of metal vapour arcs in vacuum, Eindhoven University of Technology. Eindhoven (1978)

Dav 69 W.D. Davis and H.C. Miller, J. Appl. Phys. 40 (1969) 2212

Del 74 J.L. Delcroix and A.R. Tindale, J. de Phys. 29 (1968) 605

Dja 71 B.E.D. Djakov and R. Holmes J. Phys. D, Appl. Phys. 4 (1971) 504

Dra 73 H.W. Drawin, Phys. Lett. 42a (1973) 423

Dro 81 M.G. Drouet, 15th Int. Conf. Phen. Ion. Gas., Minsk, USSR, (1981) 481

Eas 34 E.C. Easton, F.B. Lucas and F. Creedy Elec. Eng 53 (1934) 1454

Eck 74 G. Ecker, IEEE Trans. Plasma Scienc. PS-2 (1974) 130

Eck 80 G. Ecker, Theoretical aspects of the vacuum arc in "Vacuum arcs" editor J.M. Lafferty, John Wiley, New York (1980)

Elb 61 M. Elbel and W. Fischer, Z. Physik 165 (1961) 151

Far 80b G.A. Farrall, Arc ignition processes in "Vacuum arcs" editor J.M. Lafferty, John Wiley, New York (1980)

Far 80a G.A. Farral, Electrical breakdown in vacuum in "Vacuum arcs" editor J.M. Lafferty, John Wiley, New York (1980)

Foo 79 J.A. Foosnaes and W.G. Rondeel, J. Phys.D, Appl.Phys. 12 (1979) 1867

Fow 28 R.H. Fowler and L. Nordheim, Proc Roy. Soc. (London) A119 (1928) 173

Fra 71 S. Fragan, K. Saxena and B.Lo, Atomic Data 3 (1971) 323

Fuj 72 T. Fujimoto, Y. Ogata, I. Sugiyama, K. Tachibana and K. Fukuda, Jap. J. Appl. Phys. 11 (1972) 718

Fuj 79 T. Fujimoto, Jap. Phys. Soc. Japan 47 (1979) 265

Gib 64 A. Gibson and G.W. Reid, Appl. Phys. Lett. 5 (1964) 195

Gol 80 S. Goldsmith and R.L. Boxman, J. Appl. Phys. 51 (1980) 3649

Gol 81 S. Goldsmith, S. Shalev and R.L. Boxman, Physica 104C (1981) 107

Gra 68 P.H. Grassmann, Z. Naturforsch. 23a (1968) 251

Gri 74 J.T. Grissom and C.J. Newton J. Appl. Phys. 45 (1974) 2885

Gun 71 G. Gundersen, Thesis, Anode spot formation in vacuum arcs, Norweg. Inst. Techn., Trondheim (1971)

Gun 72 H.C.W. Gundlach, 1972 5th. Int. Symp. Disc. Elec. Insul. Vac., Poland (1972) 249

Gun 78 H.C.W. Gundlach, 1978 8th Int. Symp. Disc. Elec. Insul. Vac., Albuquerque, New Mexico (1978) 1

Haa 82 J.C.M. de Haas, Int. Report VDF/NT 82-06, Eindhoven University of Technology, Eindhoven (1982)

Har 79 J.H. Harris, J. Appl. Phys. 50 (1979) 753

Heb 80 J.V.R. Heberlein and J.G.Gorman IEEE Trans. Plasma Scienc. Ps-8 (1980) 283

Hol 67 R. Holm, Electrical contacts, Springer, Berlijn 1967

Jen 75 J.E. Jenkins, J.C. Sherman, R. Webster and R. Holmes J. Phys. D, Appl. Phys. 8 (1975) 139

Jol 72 D.C. Jolly, data obtained from Box 74

Jol 75 J. Jolly and M. Touzeau, J. Quant. Spectrosc. Radiat. Transfer 15 (1975) 863

Kan 81 T. Kaneda, E. Kaneko, S. Yanabu and H. Ikeda, Physica 104C (1981) 124

Kas 78 A. Kasperczuk, M. Paduch, L. Pokora and Z. Wereszczynski, J. Techn. Phys. 19 (1978) 137

Kim 69 C.W. Kimblin, J. Appl. Phys. 40 (1969) 1744

Kim 73 C.W. Kimblin, 11th. Int. Conf. Phen. Ion. Gas, Praque (1973) C72

Kim 74 C.W. Kimblin, IEEE Trans. Plasma Scienc. Ps-2 (1974) 310

Klu 67 O. Klueber, Z. Naturforsch. 22a (1967) 1473

Koc 68 M. Kock and J. Richter, Z. Astrophysik 69 (1968) 180

Laa 76 P.C.T. van der Laan, J.P. Friedberg and K.S. Thomas Report scientific Laboratory, Los Alamos, LA-6413-P (1976)

Lid 62 L.M. Lidsky, S.D. Rothleder, D.J. Rose, S. Yoshikawa, C. Michelson and R.J. Mackin, J. Appl. Phys. 33 (1962) 2490

Loc 68 W. Lochte-Holtgreven in Plasma diagnostics, North Holland Publ. Comp., Amsterdan 1968

Lun 50 S. Lundquist, Arkiv Foer Fysik 35 (1950) 361

Mae 54 H.Maecker and T. Peters, Z. Physik 139 (1954) 448

Mil 77 H.C. Miller, IEEE Trans. Plasma Scienc. Ps-5 (1977) 181

Mil 79 H.C. Miller, J. Phys. D, Appl. Phys. 12 (1979) 1293

Mil 81 H.C. Miller, J. Appl. Phys. 52 (1981) 4523

Mit 70 G.R. Mitchell, Proc. IEE 117 (1970) 2315

Miy 80 K. Miyamoto, Plasma physics for nuclear fusion, MIT press, New York (1980) ISBN 0-262-13145-5

Mor 73 O. Morimiya, S. Sohma, T. Sugawara and H. Mizutani Trans. IEEE Power App. Syst. Pas-92 (1973) 1723

Mul 80 J.J.A.M. van der Mullen, B. van der Sijde and D.C. Schram, Phys. Lett. 79a (1980) 51

Mul 81 J.J.A.M. van der Mullen, B. van der Sijde and D.C. Schram, ICPIG-Minsk, USSR (1981) 441

Ney 66 J. Ney, Z. Physik 196 (1966) 53

Pat 79 M.D. Pattengill and D.E. Sands, J. Chem. Educ. 56 (1979) 245

Ply 65 A.A. Plyutto, V.N. Ryzhkov and A.T. Kapin Sov. Phys.-J. Exp. Theor. Phys. 20 (1965) 328

Pot 79 B.F.M. Pots, Turbulence and Transport in a magnetized argon plasma Thesis, Eindhoven University of technology, Eindhoven 1979

Ree 63 M.P. Reece, Proc. IEE 110 (1963) 793

Ric 71 J.H. Rich, L.E. Prescott and J.D. Cobine J. Appl. Phys. 42 (1971) 587

Ron 75 W.G.J. Rondeel, J. Phys., D. Appl. Phys. 8 (1975)

Ros 81 R.J. Rosado, An investigation of non-equilibrium effects in thermal argon plasmas., Thesis, Eindhoven University of technology Eindhoven, 1981

Sch 23 W. Schottky, Z. Physik 14 (1923) 63

Sch 74 F.C. Schueller, Arc discharges in a curved magnetic field, Thesis, University of Utrecht 1974

Sch 81 H. Schellekens, Physica 104C (1981) 130

Sch 83 D.C. Schram, J.J.M. van der Mullen, B.F.M. Pots and C.J. Timmermans, to be published in Z. fuer Naturforsch. (1983)

Sea 59 M.J. Seaton, Phys. Rev. 113 (1959) 814

She 73 J.C. Sherman, R. Webster, J.E. Jenkins and R. Holmes Report ULAP-T17, University of Liverpool, 1973

She 77 J.C. Sherman, R. Webster, J.E. Jenkins and R. Holmes, J. Phys. D, Appl. Phys. 11 (1978) 379

Sij 82 B. van der Sijde, J.J.A.M. van der Mullen and D.C. Schram Invited talk Leipzig, DDR, 1982, to be published Beitr. Plasma Physik.

Sta 03 J. Stark, Z. Physik 4 (1903) 440

Ste 77 K. Stefaniak, 3rd Int. Symp. Switch. Arc Phen., Lodz, Poland (1977) 217

Tan 30 R. Tanberg, Phys. Rev. 35 (1930) 1080

The 77 P.G.A. Theuws, H.C.W. Beyerink, D.C. Schram and N.F. Verster J. Appl. Phys. 48 (1977) 226

Tim 81 C.J. Timmermans, D.C. Schram and A. Lunk, Beitr. Plasma Physik 21 (1981) 117

Uo 64 K. Uo, Report Plasma Physics Laboratory, Princeton, New York, Matt-255 (1964)

Ven 73 G. Venus, Z. Physik 259 (1973) 437

Web 76 R. Webster, J.E. Jenkins, J.C. Sherman and R. Holmes, Report University of Liverpool, Liverpool ULap T-43, Liverpool 1976

Zel 66 Y.B. Zeldovich, Physics of Shock Waves, Vol. 1 Ac.Press., New York, 1966

Summary

This thesis concerns a study of the diffuse vacuum arc which can occur in vacuum circuitbreakers. This study focusses on two points:

- the determination of the characteristic quantities of the plasma of the diffuse vacuum arc.
- the description of the arcing behaviour by means of magnetohydrodynamic equations.

The aim of this study is to gain insight into the cause of anode spot formation by a study of the diffuse vacuum arc.

First an identification of the range of parameters, in which the diffuse vacuum arc occurs, is given. Then four diagnostic methods are described, which are used to determine the plasma quantities. The electron temperature has been determined by means of spectroscopy. Although the atomic systems in the vacuum arc are not in local thermal equilibrium, it is possible to determine the electron temperature from spectral line emission by making use of recent knowledge about the existence of a complete excitation saturation state in the atomic systems. The spatial dependence of the electron density has been determined from the intensity distribution of the continuum radiation. From line emission the spatial dependence of the neutral density is also determined in the electrode region. The absolute value of both the electron density and the neutral density has been obtained with laser interferometry. The ion temperature has been measured with a Fabry-Pérot interferometer. The ion temperature appears to be higher than the electron temperature. On this moment there is no satisfactory explanation for this observation. With diamagnetic loops the radial dependence of the generated axial magnetic field has been determined. It appears that at low externally applied axial magnetic field strengths the azimuthal currents in the arc generate an additional axial magnetic field of comparable strength as the applied axial magnetic field.

An important conclusion, which follows from the measurements, is that the mean free path's of ions and electrons are small compared to the geometrical dimensions of the arc. This allows a description of the arcing behaviour by means of magnetohydrodynamic equations, what leads to a model of the diffuse vacuum arc. This model gives a relationship

between the pressure in the arc and the radial current density as well as a relationship between the azimzuthal current density and the radial current density. With the arcing model the radial current density can be calculated from the azimuthal current density. The measurements of the particle temperatures and densities yield knowledge about the pressure in the arc, which yields an estimate of the radial current density. The in these two ways obtained radial current densities are of the same magnitude. The model gives also a relationship between the radial current density and the electrical field strength in the arc. The from this field calculated voltage drop matches the measured voltage drop. Hence it is concluded that the radial current density governs the processes in the diffuse vacuum arc. At low axial magnetic field strength the large radial current density causes a very strong increase of the axial current density in front of the anode. Together with the associated higher arcing voltage the axial current density causes a significant energy flux toward the anode so high that this electrode starts to melt locally, and the anode spot is formed. Therefore, the transition from the diffuse arc to the anode spot is determined by the processes in the diffuse vacuum arc.
An externally applied axial magnetic field leads to a reduction of the radial current density and to an even larger reduction of the energy flux towards the anode. As a consequence anode spot formation occurs at much higher current levels.

It is concluded, that the model of the diffuse vacuum arc gives a reasonably well description of the arcing processes. Hence with this model it will be possible to construct the arcing region so that anode spot formation occurs at higher current levels than hitherto.

Samenvatting

Dit proefschrift betreft een studie van de diffuse vacuumboog, welke optreedt in vacuumvermogensschakelaars. Deze studie richt zich op twee punten:
- de bepaling van de karakteristieke grootheden van het plasma van de diffuse vacuumboog.
- de beschrijving van het gedrag van de boog met behulp van magnetohydrodynamische vergelijkingen.

Het doel is inzicht te krijgen in de oorzaak van de vorming van een anode spot door een studie van de diffuse vacuumboog.

Na een afbakening van het parameter gebied waarin de diffuse boog voorkomt worden vier diagnostieken beschreven die aangewend zijn ter bepaling van de plasma grootheden. De elektronentemperatuur is bepaald met behulp van spectroscopie. Ofschoon de atomaire systemen in de vacuumboog niet in locaal thermisch evenwicht zijn, blijkt het mogelijk uit de lijnemissie de electronentemperatuur te bepalen. Hierbij is gebruik gemaakt van recente kennis over het bestaan van een volledige excitatie verzadiging in de atomaire systemen. Het electronendichtheidsverloop is bepaald uit de intensiteitsverdeling van de continuümstraling. Met behulp van spectroscopie is ook het verloop van de neutrale dichtheid in de door de electroden begrensde ruimte bepaald. De absolute waarde van zowel de electronen als de neutrale dichtheid is verkregen met behulp van laserinterferometrie. De ionentemperatuur is bepaald met gebruikmaking van een Fabry-Pérot interferometer. De ionentemperatuur blijkt voor alle onderzochte boogparameters hoger te zijn dan de electronentemperatuur. Op dit moment is er geen verklaring voor deze waarneming. Met diamagnetische lussen is de radiale verdeling van het gegenereerde axiale magneetveld bepaald. Hieruit blijkt dat bij lage extern aangelegde magneetvelden de azimuthale stromen in de boog een axiaal magneetveld genereren van vergelijkbare sterkte als het aangelegde magneetveld.

Een belangrijke conclusie, die getrokken kan worden uit de metingen, is dat de vrije weglengten van ionen en electronen kleiner zijn dan de afmetingen van de boog. Daarom kan het gedrag van de boog beschreven worden met magnetohydrodynamische vergelijkingen. Dit resulteert in een model van de diffuse vacuumboog. Het model geeft zowel een verband tussen de drukopbouw in de boog en de radiale stroom dichtheid als een verband tussen de azimuthale en de radiale stroomdichtheid.

Met het model kan uit de gemeten azimuthale stroomdichtheid de radiale stroomdichtheid berekend worden. De metingen van de deeltjes temperaturen en dichtheden leiden tot kennis van de drukopbouw in de boog. Hieruit volgt een schatting van de radiale stroomdichtheid. De op beide manieren verkregen radiale stroomdichtheden zijn van gelijke grootte orde. Bovendien legt het model een verband tussen de electrische veldsterkte in de boog en de radiale stroomdichtheid. De hiermee berekende spanningsval over de boog komt overeen met de gevonden spanningsval. Derhalve wordt geconcludeerd dat de radiale stroomdichtheid de processen in de diffuse vacuumboog beheerst. De bij lage axiale magneetvelden grote radiale stroomdichtheid leidt tot een zeer sterke toename van de axiale stroomdichtheid direct voor de anode. Samen met de daarmee samenhangende hogere boogspanning veroorzaakt dit een dermate hoge energiestroom naar de anode dat deze lokaal begint te smelten, de anode smeltvlek. De overgang van de diffuse boog naar de anode smeltvlek blijkt derhalve voornamelijk bepaalde door processen, die optreden in de diffuse boog. Door het aanleggen van een axiaal magneetveld wordt de radiale stroomdichtheid verminderd. Dit leidt tot een verlaging van de thermische belasting van de anode. Het gevolg is dat bij veel hogere stromen een anode smeltvlek optreedt.

Geconcludeerd kan worden dat het model van de diffuse vacuumboog de boogprocessen redelijk beschrijft. Derhalve zal het mogelijk zijn met dit model de boogruimte zo te construeren, dat anode smeltvlek vorming optreedt bij hogere stromen dan tot nu toe.

Dankwoord

Dank is verschuldigd aan alle werknemers van Holec Hazemeyer en van de Technische Hogeschool Eindhoven, die geholpen hebben bij het tot stand komen van dit proefschrift. Speciaal wil ik mijn promotor professor Daan Schram en mijn directe chef drs. Harry Gundlach bedanken voor de discussies die ik met hen mocht voeren. Gaarne wil ik de medewerkers van de Researchgroep danken voor hun steun bij de experimenten. Hierbij denk ik vooral aan Jan Kwint die de opstelling draaiende hield, aan Gerard van den Bosch die een snelle oplossing had voor ieder electrisch probleem, en aan John Bleize van de groep atoom en plasma fysica van de THE, die de nauwkeurigheid van de ionentemperatuurmeting opvoerde. Ook de afdeling productie vacuumschakelaar verdient een woord van dank, in het bijzonder ir. Sjer Lipperts voor de ondersteuning van dit onderzoek en Harry Fluttert voor de tot stand koming van de experimenteer schakelaar. Binnen de computerafdeling wil ik Wolter Gierveld danken voor de speciale software. Meer in het algemeen ben ik dank verschuldigd aan groepen van de T.H. Twente, van de Universiteit Utrecht en van de T.H. Eindhoven voor het beschikbaar stellen van meetapparatuur, zonder welke de meeste experimenten niet mogelijk waren geweest. De typekamer wil ik danken voor het geduld in het aanbrengen van alle correcties en de reproductie afdeling voor de fraaie vormgeving van dit proefschrift. Ook wil ik alle stagiaires en afstudeerder, nu ir. Frank Niessen danken voor hun inbreng bij de experimenten. Tot slot dank ik Nelly, Jeroen, Linda en Martijn voor hun steun.

LEVENSLOOP

5 december 1953	geboren te Alkmaar
juni 1972	eindexamen Gymnasium-B, Bisschoppelijk College te Roermond
maart 1978	Doctoraal examen Technische Natuurkunde aan de Technische Hogeschool Eindhoven
april 1978 - december 1982	Researchmedewerker bij Holec-Hazemeyer te Hengelo
januari 1983 -	Wetenschappelijk medewerker in de groep DZO bij de N.V. KEMA te Arnhem

List of symbols

A	:transition probability
A_{dl}	:area of diamagnetic loop
a	:ratio of Lorentz to Doppler line broadening
B_r, B_θ, B_z	:cylindrical components of the magnetic field vector $\underline{B}$
c	:light velocity in vacuum
D	:diffusion coefficient
E	:excitation energy
$\underline{E}$	:electric field (chapter 5 and 6)
$\underline{E}^c$	:complex Fourier coefficients of the integrated diamagnetic loop voltages
e	:unit charge
e,i,o	:subscript denoting particle kind electron , ion and neutral
e_d	:integrated diamagnetic loop voltage
g	:statistical weight of excited state
H	:magnetic transfer function of metallic parts
h	:Planck constant
I	:intensity
I	:current
J	:quantum number
j_r, j_θ, j_z	:cylindrical components of the current density $\underline{j}$
k	:Boltzmann constant
k_0	:absorption parameter
L^S	:energy associated with particle sources
l	:length of plasma
$\underline{\underline{M}}$	:coupling matrix between plasma currents and integrated diamagnetic loop voltages
$\underline{M}^S$	:momentum associated with particle sources
m	:particle mass
n_k	:particle density
n	:refractive index
p	:pressure
p	:effective quantum number (chapter 4.1 and 6.1)

Q :energy transfer by friction between various kinds of particles

q :particle charge

$\underline{q}$:heat flow vector

$\underline{R}$:momentum transfer by friction between various kinds of particles

R_m :collisional radiative constant

R_∞ :Rydberg constant

r,θ,z :cylindrical coordinates

S :particle sources

T :particle temperature

t :time coordinate

w_r,w_θ,w_z :cylindrical components of the velocity $\underline{w}$

Z :ion charge number

α :polarizability

ε :voltage induced in diamagnetic loop (chapter 4.3)

ε :emission coefficient

ε_0 :dielectric constant

η :resistivity

η_n :viscosity coefficients; n=0,1,2,3,4

λ :wavelength of spectral line

$\Delta\lambda_d$:Doppler broadening of spectral line

ν :frequency

$\underline{\underline{\Pi}}$:viscosity tensor

τ :collision time

τ :time parameter(chapter 4.3)

Φ :magnetic flux

χ :ionization energy

ξ_{fb} :free-bound quantum mechanical correction factor

ξ_{ff} :free-free quantum mechanical correction factor

Ω :cyclotron frequency

Stellingen behorende bij het proefschrift van

HANS SCHELLEKENS

1. *In de diffuse vacuumboog speelt de drukopbouw een zeer belangrijke rol. (Dit proefschrift)*

2. *De vorming van een anode-smeltvlek wordt veroorzaakt door een toenemende warmtestroom naar de anode tengevolge van een lokale verhoging van de stroomdichtheid. (Dit proefschrift)*

3. *In een rotatie-symmetrisch en stroomvoerend plasma wordt een axiaal magneetveld gegenereerd. Derhalve dient in de analyse rekening te worden gehouden met dit magneetveld, ook al wordt dit veld niet extern aangelegd.*

4. *Door een betere beheersing van de diffuse vacuumboog kan de spanningsvastheid van vacuumvermogenschakelaars een niveau bereiken gelijkwaardig aan dat van SF_6-hoogspanningsschakelaars.*
(EPRI rapport EL-1895 (1981))

5. *De geringe contacterosie in vacuumvermogenschakelaars maakt deze bij uitstek geschikt voor toepassing in geautomatiseerde netten met hoge schakelfrequenties.*

6. *In de numerieke simulatie van Sohet et.al. is ten onrechte de invloed van de neutralen niet meegenomen.*
(J.L.Sohet, P.D.Pedrow en L.M.Burrage
IEEE Trans. Plasma Scienc. Ps-9 (1981) 254)

7. *De positie van de inlaatopening van de derde waterkolom in de door water bewogen Stirling motor is bepalend voor het al of niet werken van deze machine.*
(S.C.Bhargava, R.Rup, R.P.Saxena en P.K.Srivastava J.Appl.Phys. 49 (1978) 3521)

8. *Snelfilmfotografie leidt dikwijls tot foutieve interpretaties.*

9. *Voor het opwekken van infra-rode straling in het millimeter golflengtegebied kan met voordeel gebruik gemaakt worden van een holle kathode-ontlading.*

10. *Bij de analyse van de balansvergelijkingen van neutraal koper, geioniseerd koper en geioniseerd neon in het negatieve glimlicht van een neon-ontlading met koperen holle kathode gaan Warner et.al. uit van onjuiste veronderstellingen over het dichtheidsverloop van neutraal koper aan de kathode wand.*
(B.E.Warner, K.B.Persson en G.J.Collins J.Appl.Phys. 50 (1979) 5694)

11. *Chinese referenties zullen een belangrijke plaats gaan innemen in de literatuurlijsten van toekomstige proefschriften.*
